High-Resolution 3D Diffuse Optical Tomography for Non-invasive Functional Brain Imaging in the Sub-Centimeter Range

Christina Habermehl, MSc.

Berlin 2014

High-Resolution 3D Diffuse Optical Tomography for Non-invasive Functional Brain Imaging in the Sub-Centimeter Range

Von der Fakultät IV - Elektrotechnik und Informatik
der Technischen Universität Berlin
zur Erlangung des akademischen Grades
Doktorin der Naturwissenschaften (Dr. rer. nat.)
genehmigte Dissertation

vorgelegt von
Christina Habermehl geb. Siegel
geb. in Berlin

Erstgutachter: Prof. Dr. Klaus-Robert Müller
Zweitgutachter: Prof. Dr. Hamid Dehghani
Drittgutachter: Dr. Jens Steinbrink
Tag der wissenschaftlichen Aussprache: 8. September 2014

Berlin 2014

Acknowledgement

I would like to give sincere thanks to Dr. Jens Steinbrink whose enormous support and persistent help was invaluable during the course of my thesis. His comments and suggestions were of inestimable value for all the studies.

I have also greatly benefited from the expertise and friendship with Dr. Christoph Schmitz who believed in me from the beginning. Christoph and Jens formed a warm and familiar atmosphere, which I believe is unique in the scientific world.

Special thanks goes to Prof. Klaus-Robert Müller whose ideas and comments gave new insights and perspectives. His cooperation with our group was beneficial and allowed us to broaden our horizon. Initiated by Klaus, I received generous support concerning time and expert knowledge from Dr. Stefan Haufe. Together we completed a work in the field of reconstruction algorithms.

I want to thank Prof. Hellmuth Obrig for giving insightful comments and suggestions about our projects. They definitely helped to see things clearer and improved the results. Without his and Jens' willingness to serve as subjects in sometimes painful experiments, some studies would not have been possible.

Furthermore, I thank Prof. Hamid Dehghani, who kindly agreed to serve as external referee for this work.

During my work at the Charité, I met some very friendly and generous people. I especially thank Dr. Jan Mehnert, Dr. Sophie Piper, Dr. Susanne Holtze and Dr. Franziska Preusse for their friendship and support during sometimes daunting stages of my work.

I would also like to express my gratitude to my best friend Ulrike and my family for their moral support and warm encouragements: my parents Raymonde und Horst, my brother John, my children Paul and Matti and last but not least my husband Christian. His support gave me the freedom to work within this exciting field.

Finally, I gratefully appreciate the financial support of the German Ministry of Science and Education that made it possible to complete my thesis.

Zusammenfassung

Aktivierungen von Gehirnarealen verursachen lokale Änderungen des Blutvolumens sowie der Sauerstoffversorgung. Diese wiederum verursachen Absorptionsänderungen von Licht im nahinfraroten Bereich. Nahinfrarotspektroskopie (NIRS) ist in der Lage, diese Absorptionsänderungen erfassen, indem Licht punktuell in den Kopf gegeben und wenige Zentimeter entfernt von Detektoren erfasst wird. In den letzten zwei Jahrzehnten entwickelte sich die NIRS zu einem viel genutzten funktionellen Bildgebungsverfahren.

Zur Erhöhung der räumlichen Auflösung, kann Anzahl der optischen Fasern erhöht und zusätzlich können sie in engerem Abstand zueinander auf der Kopfhaut angebracht werden. Dieser Ansatz wird *Diffuse Optische Tomographie* (DOT) genannt. Eine hohe Anzahl von Messkanälen in Kombination mit einem Verfahren zur Bildrekonstruktion führen im Ergebnis zu dreidimensionale Karten von Absorptionsänderungen (und damit lokaler Aktivierungen) im Gehirn.

Obwohl die optische Tomographie der klassischen NIRS in vielen Punkten überlegen ist, wird sie bisher nur von wenigen Gruppen angewandt. Offene Fragen dieser Methode umfassen unter anderem i) optimale Rekonstruktionsalgorithmen, ii) fehlende Evaluation in Simulationsstudien sowie daraus resultierend iii) fehlende *in vivo* Daten. Im Rahmen dieser Dissertation werden diese drei Themenkomplexe ausführlich behandelt.

In der Simulationsstudie generiere ich realistische Daten indem ein Rauschmodell verwendet wird, dass auf *in vivo* Messungen basiert. Es werden verschiedene Methoden implementiert und bewertet, darunter häufig verwendete lineare Verfahren sowie deren tiefen- und rauschgewichtete Varianten aber auch kürzlich eingeführte 'sparse' Methoden. Zwei dieser sparsen Methoden werden von aus dem Bereich der EEG- Quellenlokalisation adaptiert und im Rahmen dieser Arbeit erstmals auf das DOT-Rekonstruktionsproblem angewandt.

Im Rahmen dieser Evaluation schlage ich auch ein objektiviertes Verfahren zur Regularisierung des unterbestimmten inversen Problems vor. Dies ermöglicht die unvoreingenommene und datenbasierte Bildrekonstruktion für den Fall, dass lineare Methoden verwendet werden. Ich kann zeigen, dass diese häufig angewandten

Methoden schnell und ausreichend genaue Ergebnisse liefern. Die Präzision kann jedoch mit sparsen Methoden erhöht werden. Unabhängig vom Signal-zu-Rausch-Verhältnis, kann der LCMV Beamformer einzelne Aktivierungen mit der größten Genauigkeit rekonstruieren. Bei mehreren korrelierten Aktivierungen führt die minimum ℓ_1-norm Abschätzung zum besten Resultat.

Der zweite Teil widmet sich intensiv den Möglichkeiten von DOT als *in vivo* Bildgebungsverfahren. Zuerst präsentiere ich eine Studie zum somatosensorischen System, in der ich zeige, dass eine räumliche laterale Auflösung von unter einem Zentimeter erreicht werden kann. Weiterhin zeige ich, dass DOT und funktionelle Magnetresonanztomographie (fMRT) zu einem großen Teil vergleichbare Ergebnisse liefern. Die sich anschließende Studie zu kontrastmittelverstärkter Bildgebung zeigt, dass extra- und intra-zerebrale Schichten räumlich gut von einander getrennt werden können. Ich zeige das frühe Ansteigen der Absorption in kortikalen Schichten sowie das späte Auswaschen in den oberen Hautschichten. Die dritte Studie befasst sich mit der DOT im Ruhezustand (resting state). Ich zeige ein mit DOT erstelltes Tiefenprofil sogenannter spontaner hämodynamischer Schwingungen. Wir finden niederfrequenten Schwingungen in Bereich von 0,1Hz sowohl im Gehirn als auch in der Haut, Pulssignale jedoch werden überwiegend in den Hautschichten lokalisiert.

Abstract

Focal brain activity is accompanied by a metabolic demand and local changes in blood volume and oxygenation, which in turn results in changes of the absorption properties of the brain tissue. These changes can be determined by near infrared spectroscopy (NIRS).

During the last two decades, NIRS has emerged as a tool for functional brain imaging that can detect these absorption changes. Light is applied to the head from discrete locations and detected a few centimeters away. However, the topographic spatial resolution is in the order of a few centimeters. This is rather poor compared to other brain imaging methods such as functional magnetic resonance imaging (fMRI).

To enhance the spatial resolution of the method, an increased number of optical point sources and detectors can be applied in a dense grid with overlapping probing volumes (high-density measurement). This approach is termed *Diffuse Optical Tomography* (DOT). In DOT, measured light intensity changes from hundreds of optical data channels need to be reconstructed in order to achieve a 3D representation of changes of absorption properties.

Although DOT is advantageous over classical NIRS-topography, it has only been reported by few specialized laboratories. This is mainly due to the many open questions such as i) optimal reconstruction algorithms, ii) missing evaluations in simulations and iii) missing *in vivo* data.

With this thesis I aim to address all three issue by evaluations in computer simulations of functional brain activation, *in vivo* measurements during a somatosensory stimulation, contrast enhanced brain imaging and resting-state measurements.

For the simulation study, I mimic a highly realistic DOT measurement by adding noise that originated from an *in vivo* measurement. In contrast to the usually added white noise, this model preserves all specific features such as hemodynamic fluctuations and fiber distance-dependent noise levels, which often affect the reconstruction quality. To test the theoretical boundaries of the method and to find the optimal reconstruction method, I implement and evaluate frequently used linear methods, depth and noise-weighted variations of these methods, and

recently proposed sparse methods. Two of these sparse methods are adapted from the EEG source localization problem and I introduce them to cerebral DOT for the first time.

In the course of this evaluation, I propose an objective process for regularization to solve the under-determined inverse problem of DOT. This allows the un-biased and data driven image reconstruction when linear methods are used. I show that linear reconstruction methods provide fast and adequate results. However, their accuracy can be increased by implementing sparse algorithms, albeit at the expense of computational time and effort. Independent of the applied noise level, I find that the linearly constrained minimum variance (LCMV) beamformer is best for single spot activations with perfect location and focality of the result, whereas the minimum ℓ_1-norm estimate succeeds with multiple targets.

The central contribution of this thesis is a broad evaluation of how far the limits of DOT as a functional and physiological brain imaging tool can be pushed. Therefore, a large part of this work is dedicated to the *in vivo* ability of high-density DOT. For the study on somatosensory stimulation I show that a spatial resolution of under one centimeter can be obtained. Additionally, DOT and fMRI find comparable lateral positions in seven out of ten finger representations. The study on contrast enhanced imaging succeeds in the attempt of showing the separation of intra- and extra cerebral tissue by tracking the bolus of safe dye. I show the early arrival of the contrast agent in deeper (cortical) layers and the late wash out from superficial (skin) layers. The last study utilizes resting state measurements and demonstrates that DOT allows a depth profiling of spontaneous hemodynamic rhythms in the adult head. Low frequency oscillations (0.1Hz) are found in cortical but also superficial voxels, whereas heart beat signals are localized within superficial layers.

Contents

1 Introduction

1.1 Diffuse Optical Tomography in Functional Brain Imaging in Humans

Functional near infrared spectroscopy (fNIRS) is an optical tool to monitor changes in cerebral blood oxygenation. FNIRS measures changes in the absorption of near infrared light in the cortex and allows estimating the functionally evoked changes in cerebral oxygenated (HbO_2) and deoxygenated hemoglobin (HbR) concentration due to local brain activation. For fNIRS, light in the near infrared-range (650-850nm) is brought to the head by a light source (e.g. LED or laser) and the back reflected light is detected some centimeters away.

NIRS is non-invasive, low cost and easy to apply. To some extent, it can serve as a substitute for functional magnetic resonance imaging (fMRI), especially for studies where the task is not suitable for an MRI scanner, e.g. when auditory stimuli are involved or more importantly when children or even newborns are investigated. Research with fNIRS in children include developmental and psychiatric studies (Aslin, 2012; Franceschini et al., 2007; Hyde et al., 2010; Wilcox et al., 2012) and monitoring of brain-injured children (Murkin and Arango, 2009; Goff et al., 2010; Kwak et al., 2007; Mittnacht, 2010). Application in adults includes physiological and psychological (Gagnon et al., 2012; Hyodo et al., 2012; Jackson et al., 2012; Suhr and Chelberg, 2013; Tsujii et al., 2013) as well as an increasing number of psychiatric or pathophysiological studies such as monitoring stroke patients (Budohoski et al., 2012; Oldag et al., 2012; Pizza et al., 2012) and epilepsy (Buchheim et al., 2004; Nguyen et al., 2013; Slone et al., 2012). Within the last decade, fNIRS technology has been advanced to be applicable also for modern research questions such as the use in brain-computer-interfaces (BCI) to enhance classification accuracy

(Birbaumer, 2006; Birbaumer et al., 2006; Fazli et al., 2012b,a; Pfurtscheller et al., 2010; Power et al., 2012; Sitaram et al., 2009) and new types of monitoring at the bed-side. For instance, resting state analysis using NIRS has been shown to be appropriate to identify functional connectivity networks yielding comparable results as fMRI (Franceschini et al., 2006; Medvedev, 2013; Mesquita et al., 2010; Sasai et al., 2012, 2011; Tong et al., 2013).

Besides these promising applications and a wide approval of the method within the scientific community, fNIRS has some serious drawbacks. First of all, the photon propagation is governed by diffusion and most set-ups apply a few channels only (8-100) to gather information on functional brain regions. This results in a poor spatial resolution on the order of centimeters. Furthermore, since the photons are back reflected from the brain, they need to pass the scalp and skull. Therefore, NIRS data are highly sensitive to hemodynamic fluctuations in the skin. Systemic or task-induced increases in blood pressure or spontaneous hemodynamic fluctuations often contaminate the comparatively small cortical signals (Kirilina et al., 2012). This contamination is enhanced by the fact that the highest sensitivities are located close to the head surface.

One way to alleviate these drawbacks is the so-called multi-distance or *diffuse optical tomography* (DOT) approach (Barbour et al., 2001; Bluestone et al., 2001). DOT aims at transforming light intensity changes measured on the head surface with different source-detector separations ('multi-distance') into three-dimensional images instead of planar back-projection maps that are obtained with fNIRS.

In the field of neuroscience, DOT studies have focused on motor (Boas et al., 2004; Gibson et al., 2006; Joseph et al., 2006) and visual stimulation (White and Culver, 2010a; Zeff et al., 2007). Boas et. al ((Boas et al., 2004)) inspired the field by showing planar representations of three-dimensional reconstructions of motor activation in the human cortex and compared these to topographic back projection maps. The group demonstrated an increasing lateral resolution, when overlapping multi-distance measurements were used. Moreover, White and Culver (2010b) demonstrated an improved lateral resolution when a denser imaging grid is used.

Beside this ground research, DOT has not found its way to a wide scientific community yet. One reasons for this retention is that the image generation ('reconstruction') is not as straight forward as in fNIRS, where after raw data processing, the measured intensity changes are converted into concentration changes of the chromophores.

As a first step in DOT image reconstruction, the fluence of light within the head has to be simulated and a sensitivity pattern of all volume elements for a specific source and detector arrangement has to be determined. This is the so-called forward problem and until a few years ago, user-friendly, realistic and fast implementations of this forward modeling were not available. Furthermore, the problem of merging the forward space and the real world measurement space was open. Another challenge is solving the underdetermined and ill-posed inverse problem of reconstructing inner changes in optical properties from measured light intensity changes. This inversion relies on stabilization due to the nature of the sensitivity matrix. Reliable methods to determine this stabilization parameter have been missing and a systematic benchmarking of different reconstruction methods for cerebral DOT has not been performed.

1.2 Scientific Proposal

This work aims at promoting DOT as a functional brain imaging tool. I hypothesize that DOT vastly improves fNIRS, bringing it closer to the capabilities of fMRI. Due to its multi-distance approach and its increased spatial resolution, DOT is able to detect very small activations and can separate cortical from non-cortical signals in a 3D manner. To test and to corroborate this hypothesis, I will perform extensive simulation studies as well as *in vivo* measurements using HR-DOT in humans. The simulation studies aim at evaluating standard and newly introduced image reconstruction procedures as well as promoting a method to minimize user-guided influence on the reconstruction process. I perform various *in vivo* studies to evaluate and improve the applicability of DOT and to test its limitations and potentials concerning spatial resolution and depth separation.

1.3 Outline of the Thesis

In the first part of this thesis (chapters 2 and 3) I will discuss principles that are involved in DOT. This includes the physiological processes facilitating the detection of cortical activation and the physical premises including light propagation in tissue and detection of back reflected light. In the methodological section I will especially address approaches for image reconstruction

and quality assessment.

In chapter 4, I will demonstrate results from a simulation study. By simulating realistic DOT measurements, I assess drawbacks and advantages of a high number of reconstruction methods. These include algorithms that I adopt from the EEG-source localization problem and which I apply to the inverse problem of DOT for the first time. I can show, that a beamforming algorithm yields excellent results independently from the noise level of the data when one activation site is assumed. However, this method fails when more spots in the volume are activated. Other source localization methods such as SFLEX or minimum ℓ_1-norm approaches outperform standard methods such as tSVD or minimum ℓ_2-norm, which tend to blur images.

For these frequently used linear methods, which allow for a fast reconstruction, I demonstrate how much the reconstruction quality depends from the chosen regularization. To minimize the subjective influence on the choice of regularization, I promote a cross-validation procedure to determine the specific values automatically and only depending on the data.

The simulation study is followed by chapter 5, in which I depict results from *in vivo* DOT measurements for functional brain imaging. In order to investigate the limits of spatial resolution I apply a somatosensory finger stimulation. I find that DOT is capable to resolve brain activation in the sub-centimeter range.

Two other *in vivo* studies (see chapters 6 and 7) focus on the separation of cortical and non-cortical compartments. In the first study, I utilize an optical contrast agent whereas in the second I utilize intrinsic spontaneous hemodynamic oscillations. This is the first time, that the differentiation between different layers of the head is shown with DOT in a three-dimensional manner.

1.4 List of Publications

Some of the work reported in this dissertation has already been reported elsewhere.

1.4.1 Publications in peer reviewed journals

- **C. Habermehl**, J. Steinbrink, K.R. Müller, S. Haufe. *Optimizing the Regularization for Image Reconstruction of Cerebral Diffuse Optical*

Tomography, Journal of Biomedical Optics, accepted (2014).

- **C. Habermehl**, S. Holtze, J. Steinbrink, S.P. Koch, H. Obrig, J. Mehnert, and C. H. Schmitz, *Somatosensory activation of two fingers can be discriminated with ultrahigh-density diffuse optical tomography*, NeuroImage 5915 3201-3211 (2012).

- **C. Habermehl**, C.H. Schmitz, and J. Steinbrink, *Contrast enhanced high-resolution diffuse optical tomography of the human brain using ICG*, Optics express 19, 18636-18644 (2011).

- S.K. Piper, A. Krueger, S.P. Koch, J. Mehnert, **C. Habermehl**, J. Steinbrink, H. Obrig, C.H. Schmitz, *A wearable multi-channel fNIRS system for brain imaging in freely moving subjects.* Neuroimage 85 Pt 1, 64-71 (2014)

- S.K.Piper, **C. Habermehl**, C.H. Schmitz, W.M. Kuebler, H. Obrig, J. Steinbrink, J. Mehnert, *Towards whole-body fluorescence imaging in humans.* PLoS One 8, e83749 (2013).

- S.P. Koch, **C. Habermehl**, J. Mehnert, C.H. Schmitz, S. Holtze, A. Villringer, J. Steinbrink, and H. Obrig, *High-resolution optical functional mapping of the human somatosensory cortex*, Frontiers in neuroenergetics 2, 12 (2010).

1.4.2 Conference proceedings

- **C. Habermehl**, C.H. Schmitz,S.P. Koch, J. Mehnert, J. Steinbrink, *Investigating hemodynamics in scalp and brain using high-resolution diffuse optical tomography in humans* (paper BSu2A.2). Biomedical Optics and 3-D Imaging OSA Technical Digest (Optical Society of America).(2012)

- **C. Habermehl**, C.H. Schmitz, and J. Steinbrink, *Contrast-enhanced diffuse optical tomography of brain perfusion in humans using ICG*, in Progress in Biomedical Optics and Imaging (Proceedings of SPIE, San Francisco), (2012).

- **C. Habermehl**, C. Schmitz, J. Mehnert, S. Holtze, and J. Steinbrink, *Three-dimensional superposition of diffuse optical tomography results*

and subjacent anatomic structures, in Diffuse Optical Imaging III, P. T. Andreas H. Hielscher, ed. Proceedings of SPIE Munich, Germany, (2011).

1.4.3 Talks

- *Investigating the origin of hemodynamic fluctuations using high-resolution diffuse optical tomography in humans.* Functional Near Infrared Spectroscopy, University College London (2012)
- *Three-dimensional Superposition of Optical Tomography Results on Subjacent Anatomic Structures.* Optical Society of America & SPIE: European Conference of Biomedical Optics (ECBO), München, (2011).
- *Contrast-enhanced diffuse optical tomography of brain perfusion in humans using ICG.* SPIE: Photonics West, San Francisco, (2012).
- *Investigating hemodynamics in scalp and brain using high-resolution diffuse optical tomography in humans.* Optical Society of America: BIOMED, Miami, (2012).

1.4.4 Posters

- *Three-dimensional Superimposition of Optical Tomography Results on Subjacent Anatomic Structures.* Organisation for Human Brain Mapping: OHBM, Barcelona, (2010)
- *Depth sensitivity in multi-distance NIRS measurements in humans.* Optical Society of America: BIOMED, Miami, (2012)

2 NIRS - detecting brain activity with light

2.1 Physiological Background

Within the last 20 years, there has been an almost exponential increase of publications investigating human brain function with near infrared spectroscopy.When searching Pubmed (http://www.ncbi.nlm.nih.gov/pubmed) for 'near infrared spectroscopy' and 'human brain' for publications in the year 1990, six results are obtained. For 2000, we get 78 results and for 2012 we find 304 publications (see, Figure 2.1). Although still in a niche within neuro-scientific methods (the same search for EEG showed more than 4000 results for 2012), this development shows the increased impact of this optical method for human brain imaging.

The basic principles of NIRS are widely discussed in the literature and a good introduction can be obtained from Taber et al. (2010). In the following, we will shortly explain fundamentals that allow assessing human brain function via an optical method. The link between cortical activity and its noninvasive detection with light is the principle of *neurovascular coupling*. Neuronal activity that may be caused by a specific task or stimulus initiates the release of neurotransmitters. The restoration of ionic gradients and recycling of neurotransmitters increases the demand of ATP and therefore the need of oxygen and glucose. This causes an increase in local cerebral blood flow. Since there is less demand of oxygen than of glucose, there is an oversupply of hemoglobin and the concentrations of both states within the tissue drift apart; with a time delay of $\sim$5s, the concentration of HbO_2 increases whereas the fraction of HbR within the tissue decreases (for a sketch of the temporal response see Figure 2.2).

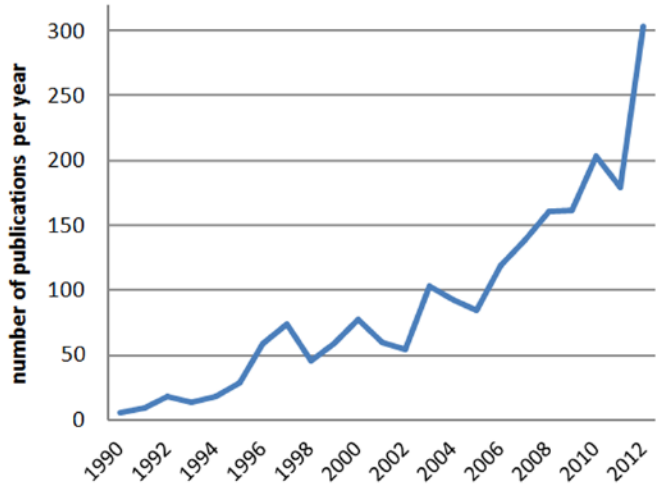

Figure 2.1: Number of publications for 'near infrared spectroscopy' and 'human brain' in Pubmed (August 2013).

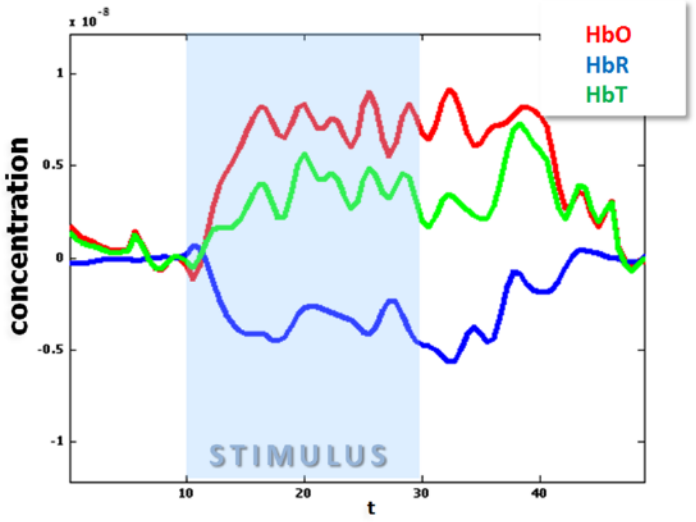

Figure 2.2: Schematic of the hemodynamic response following a stimulation at t=10s. The concentration of deoxygenated hemoglobin decreases, whereas the concentration of oxygenated hemoglobin increases.

2.2 Physical Background-Light Propagation, Absorption and Detection

The connection between concentration changes of HbO_2 and HbR and their determination with near infrared (NIR) light is the so-called 'optical window' (see, Figure 2.3). Light propagation in biological tissue is highly diffusive, which means that the reduced scattering (μ_s') of applied photons dominates over absorption (μ_a). For example, the values for 760nm and scalp tissue can be assumed as 7.3 cm^{-1} for μ_s' and 0.177cm^{-1} for μ_a (skull: 9.3/0.125, cerebrospinal fluid: 0.1/0.021, brain: 11.8/0.192)(Strangman et al., 2003).

However, absorption of NIR light is mainly affected by the two chromophores HbO_2 and HbR. For NIRS, light of two different wavelengths is applied to the subject's head via an optical fiber (optode). The lower wavelength in the range of 690-750nm is more sensitive to changes in HbR whereas the higher (830-850nm) is mainly absorbed by HbO_2). A few centimeters away, the leaving light is detected by a photodiode. One source-detector combination is defined as an 'optical data channel'.

Changes in light attenuation between source and detector can be transformed into changes in the concentration of HbO_2 and HbR by applying the modified Beer-Lambert law (Delpy et al., 1988; Sassaroli and Fantini, 2004). The average of the trajectories of the detected photons passing the tissue between source and detector has a typical ellipsoid ('banana') shape (see, Figure 2.4).

Usually, fNIRS studies use a topographic approach with inter-fiber-distances of 2 to 4cm, covering particular regions of interest (Franceschini et al., 2003; Holper et al., 2010) or the whole head (Franceschini et al., 2006; Takeuchi et al., 2009) depending on the imaging machine, the number of available optical fibers and the focus of the research.

This topographic fNIRS has been widely used within the last decade, and has become an accepted tool in brain research as a stand-alone method for physiological (Holper et al., 2009; Miyai et al., 2001), psychological (Hyde et al., 2010; Nakahachi et al., 2010; Wartenburger et al., 2007) or psychiatric studies (Kameyama et al., 2006; Zhu et al., 2010) and has been also frequently used in combined NIRS-EEG studies (Fazli et al., 2012a; Telkemeyer et al., 2011). Previously, resting state analysis using NIRS with a high coverage of the head identified the same functional connectivity networks as fMRI experiments (Franceschini et al., 2006; Mesquita et al., 2010)

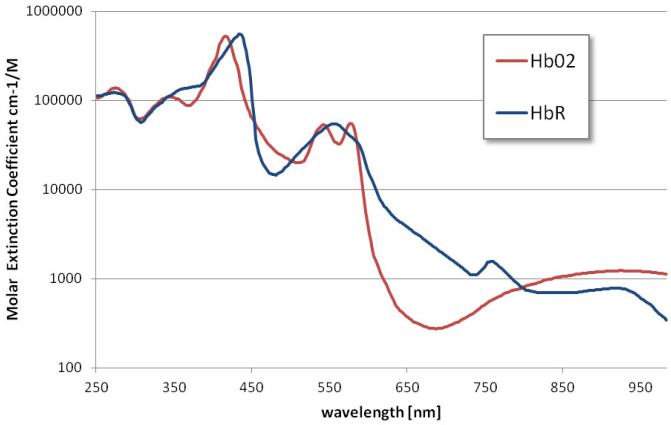

Figure 2.3: Molar extinction coefficient for oxygenated (HbO_2) and deoxygenated (HbR) hemoglobin.

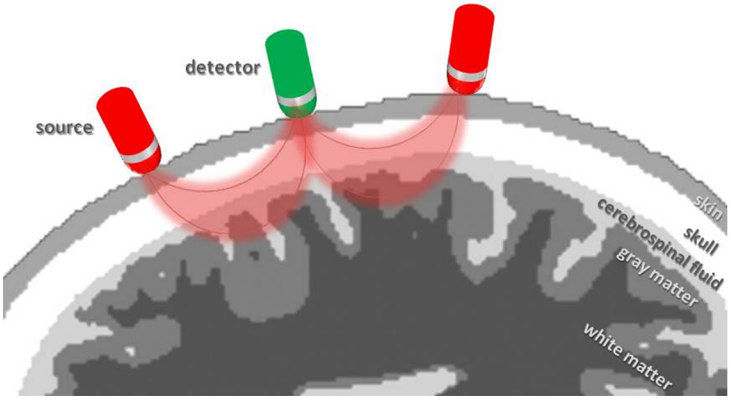

Figure 2.4: Schematic of the topographical NIRS approach. Light source and detector are placed on the head with a distance of 2-4 cm. The photons passing the head between one source-detector-combination (optical channel) form an ellipsoid ('banana') shape and some reach the cortex.

3 DOT: Multi Distance Approach for NIRS

Beside its sensitivity to superficial signals, the spatial resolution of topographic fNIRS is limited to several centimeters. However, for many applications a higher spatial resolution and depth discrimination are mandatory.

For example, investigation of rehabilitation induced changes of cortical function and neuroplasticity need a higher spatial resolution than conventional topographic NIRS can provide. By applying a multi-distance approach (Barbour et al., 2001; Bluestone et al., 2001), the spatial resolution can be increased. Dense arrays of optical fibers allow for recording many optical data channels from different source-detector (SD) distances and therefore also from different tissue depths (Figure 3.1).

The approach of diffuse optical tomography (DOT) transforms the signal content from different measuring distances into depth information, thus forming three-dimensional image maps instead of the planar back-projection, which is obtained with topographic fNIRS.

In DOT, the inter-fiber distance can vary according to the task and the imaging machine. Most groups, (Boas et al., 2004; Joseph et al., 2006; White et al., 2009; Zeff et al., 2007) use fiber grids with a minimum SD separation of about 13-25mm. In the following, we refer to this approach as 'high-density' DOT.

The sampling distance can be exceeded by applying a tighter set-up, using co-located optical fibers. Those can serve as source and detector at the same time and a lean design of the optodes allows a minimum distance of 7.5mm (see, Figure 3.2). With this 'ultra-density' set-up, a much higher amount of data channels can be obtained.

In contrast to fNIRS, DOT has not found its way to a wider scientific community, yet. Most publications examine certain aspects of the meth-

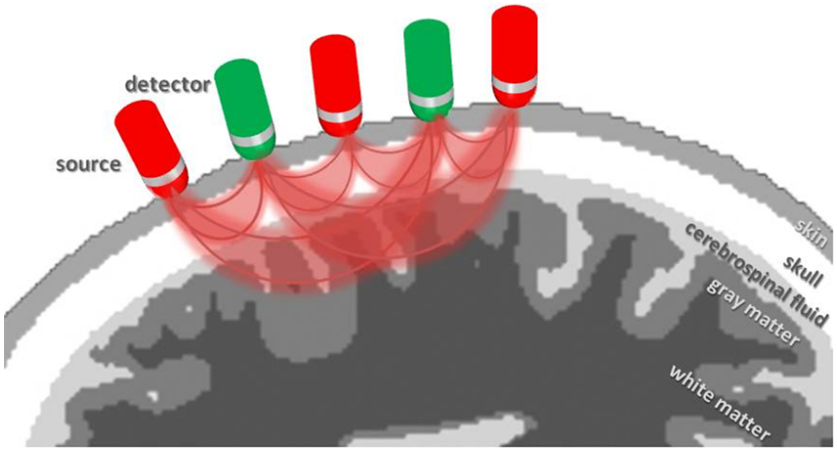

Figure 3.1: Diffuse optical tomography applies a multi-distance approach. Optical fibers are placed in a dense grid, allowing for a recording of many overlapping optical data channels and imaging of different tissue depths.

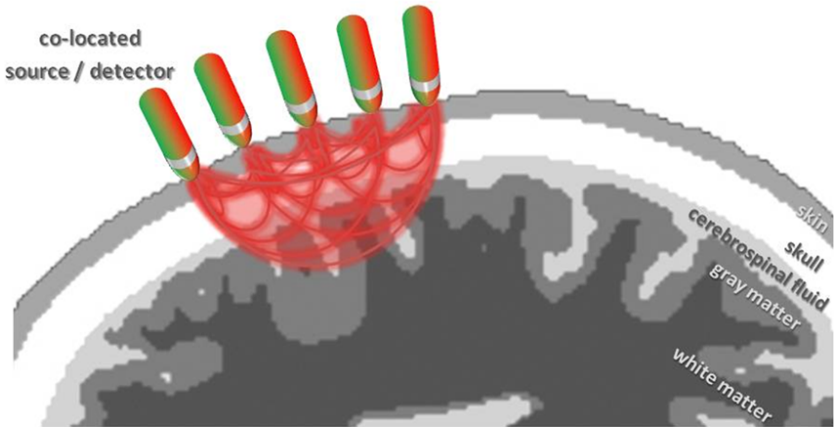

Figure 3.2: Ultra-high density approach for DOT. Optical fibers are placed on the head surface with an inter-optode distance of under 10mm. Fibers serve as source and detector, allowing for recording of multiple optical data channels.

ods like forward modeling or reconstruction methods, but applied studies are rare. 3D DOT image recovery is not as straightforward as the planar back-projection of fNIRS, where changes in light attenuation can be directly transformed into changes of HbO_2 or HbR concentration by a single 2x2 matrix inversion. On the contrary, DOT with its hyper-dense approach acquires a multiple of data of different source-detector distances and aims at recovering three-dimensional images out of this vast amount of data.

For brain imaging, it is widely accepted, that the main coefficient of interest is absorption, since scattering can be assumed stable over the time of the measurement (Arridge and Hebden, 1997). Therefore it is justified to neglect changes in μ_s' and reconstruct for changes in μ_a, only. It is also accepted to calculate relative changes between two sampling points (difference imaging or pertubation approach) since functional brain imaging aims at retrieving cortical activation instead of absolute values of chromophore concentration. Since the changes in μ_a are small, the reconstruction can be approximated by a linear representation.

The reconstruction problem in DOT aims at recovering $\Delta\mu_a$ in N volume elements given M measurements (optical data channels). Therefore, the light propagation within the tissue must be modeled in order to create a sensitivity function, which contains information about the influence of absorption changes in each element to the measured intensity changes on the surface.

In this chapter, the main challenges that are associated with DOT and its forward and inverse problem are discussed. Furthermore, we propose solutions to obstacles which may occur when cerbral DOT experiments are conducted.

3.1 Forward Modeling

First of all, a discretized representation of the scanned volume has to be created, which is typically implemented with a finite element mesh (Arridge et al., 1993). Depending on the requirements on the accuracy of reconstruction and the prerequisites of the experiment, this model can be a simple shell, a homogeneous head model or a realistic head model (atlas or individual) with inhomogeneous distribution of optical properties and arbitrary geometry of different layers.

Given the surface of the volume of interest, the location of sources and detectors on the tissue surface and inner optical properties μ_a, we define the

forward problem as finding the measurement data y on the boundary.

The result of the simulated light propagation is a sensitivity/Jacobian matrix J, with the dimension $M \times N$, where M is the number of measurements (optical data channels) and N the number of volume elements (e.g. mesh nodes) in the reconstruction volume. J describes the logarithmic relationship between changes in measured boundary data (Δy) that are caused by small changes of μ_a within the tissue, for each channel-node combination with

$$\Delta y = J \Delta \mu_a \tag{3.1}$$

Since the investigated medium can be seen as isotropic after a few scattering lengths (few mm from the light source), this forward problem is usually solved by applying the diffusion equation

$$S(r,t) = -\nabla(D\nabla\phi(r,t)) + \mu_a\phi(r,t) + \frac{1}{v}\frac{\delta\phi(r,t))}{\delta t} \tag{3.2}$$

where v is the speed of light within the medium, $\mu_a(r)$ is the absorption and $D(r)$ the diffusion coefficient at position r with

$$D = \frac{1}{3[\mu_a(r) + \mu_s'(r)]} \tag{3.3}$$

$\mu_s'(r)$ is the reduced scattering coefficient which is defined as $\mu_s' = (1 - g)\mu_s$, g is the anisotropy factor and μ_s is the scattering coefficient. The photon fluence $\phi(r,t)$, which is measured in response to the light source $S(r,t)$ can be used to recover the distribution of $\mu_a(r)$ and $D(r)$ in the 3D volume.

Such a model naturally simplifies the processes of light transport and requires assumptions about the underlying optical properties of each tissue type (skull, scalp, gray matter, white matter, cerebrospinal fluid). In the past, these properties have been determined *post mortem* or *in vitro*, and sometimes not for the specific wavelength which is used in the experiment. Researchers should be aware of this source of inaccuracy. However, it is considered as tolerable when the perturbation approach is followed.

3.2 Matching Measurement Space and Reconstruction Space

DOT measures changes in cortical concentration of relevant chromophores but it reveals no information about the measurement's underlying anatomical structures. Therefore, one challenge in optical imaging is the transfer of the measurement space in the real world to the forward model (and reconstruction) space.

There are three possible constellations for the integration of spatial priors. Figure 3.3 lists the options depending on whether an anatomic scan of the subject is available and whether a subject-specific model is desired.

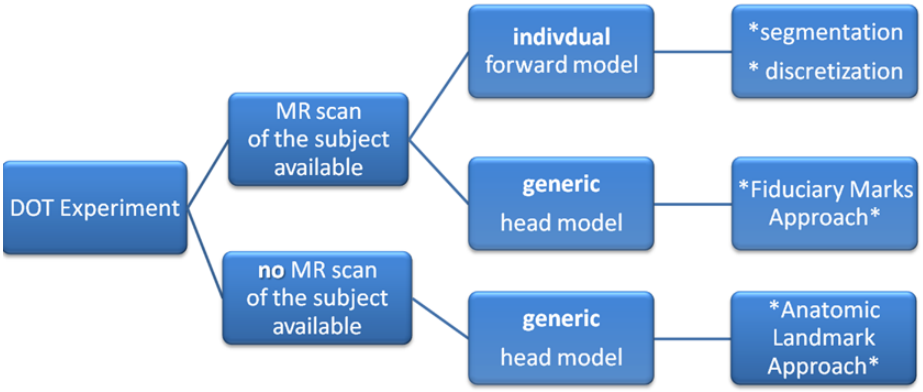

Figure 3.3: Schematic for different possibilities of matching the DOT measurement space with the forward model and reconstruction space.

3.2.1 Individual Models for Forward Modeling and Reconstruction

For some studies it might be desirable to create a forward model for each individual subject. This requires an anatomic scan (e.g. MR scan), segmentation of the different head and brain tissues, discretization of the volumes, and knowledge about optical properties of the tissue types. Various groups have developed tools that help solving these challenges.

Segmentation of different brain tissue has been widely discussed and tools are available such as SPM (Statistical Parametric Mapping; Wellcome De-

partment for Cognitive Neurology, University College London, United Kingdom; (Ashburner, 2012; Friston et al., 1995)) or the commercial BrainVoyager (Goebel, 2012). These programs focus on brain segmentation and were developed mainly for fMRI data processing. However, for DOT additional compartments such as scalp and bone play an important role in light propagation. Segmenting the soft brain tissue types from anatomic MRI scans is feasible but these scans are inappropriate to present detailed bone structures, since the magnetic resonance signals produced in bones are weak. Dogdas et al. Dogdas et al. (2005) offer mathematical morphological operations to distinguish between scalp and skull based on anatomic MRI scans and this tools helps to close the gap in producing a detailed layered head model.

Based on the segmented head, a masking and meshing software (Nirview) (Jermyn et al., 2012) can be used to create a 3D tetrahedral mesh. This mesh forms the basis to calculate the photon transport and thus provide the framework to simulate cortical activation. The free available NIRFAST software (Dehghani et al., 2008) provides a toolbox to calculate forward models based on the FE method with the possibility to incorporate individually generated meshes of different tissue types like head models. Other free tools that are available include fast, voxel based Monte Carlo (MC) simulations for photon transport using graphics processing units based parallel computing techniques (Fang and Boas, 2009) and another one to solve MC simulations based on FE meshes (Fang, 2010).

3.2.2 Fiduciary Mark Approach

There may be cases, where individual MR scans of each subject are available but a generic head model is used for forward simulation and reconstruction due to the complexity of generating individual models or the possibility to calculate group analysis. It has been shown that using a head model leads to sufficient good reconstruction quality and only slight localization error (Cooper et al., 2012; Custo et al., 2010). In this case, the positions of optical fibers have to be translocated from the measurement space to the model space.

The fiduciary marks approach requires the acquisition of an anatomical MR scan. Before or after the optical data acquisition, the corner positions of the imaging grid or other appropriate reference points of the fiber set-up have to be marked with markers that generate a high magnetic resonance (e.g. oil-filled capsules), serving as high-contrast fiduciary marks in T1 weighted MR

images. Subsequently, an anatomical MRI scan is acquired.

Then, the subject's anatomic scan is nonlinearly co-registered with the MR scan of the generic head model on which the FE-model is based. As a spatial processing tool for 3D MR scans, SPM (Ashburner, 2012; Friston et al., 1995) can be used for a spatial normalization of the subject's MR scan and the model scan. The subject's scan serves as the *source* image, wheras the model's scan is the *template*. The SPM spatial normalization tool computes an affine and subsequently a nonlinear transformation between the two volumes. The source image is warped to fit into the boundaries of the template image without losing structural information (Ashburner et al., 2011). This results in a translocation of the subject's coordinates to the forward model space. Figure 3.4 (a) shows one example of one subject that was 'warped' into the model space. Finally, the positions of the optical fibers are interpolated between the coordinates of the fiduciary marks and assigned to the finite element model boundary.

3.2.3 Anatomic Landmark Approach

Due to limited availability and high costs of MR scans, individual anatomic scans are not accessible for the subjects in all cases. Therefore, we describe a method that does not require any structural scan but uses the generic head model for anatomical mapping.

Coordinates of reference points on the subjects head surface (e.g. from the International 10-20 system (Klem et al., 1999)) and of the reference points within the fiber pad have to be recorded using a 3D digitizer (e.g. Polhemus) or a photogrammetric software (PhotoModeler, Eos Systems Inc., Vancouver, Canada)(Figure 3.5).

Then, the fiber pad coordinates are translocated to the FEM model space by solving the least square problem of the subject's reference points and the same model's reference points. This can be achieved for instance by using Horn's quaternion-based method (Horn, 1987). This approach contains translation, rotation and scaling. Finally, the fiber positions are translocated onto the FEM mesh, thereby ensuring the correct position of the reconstructed volumetric images.

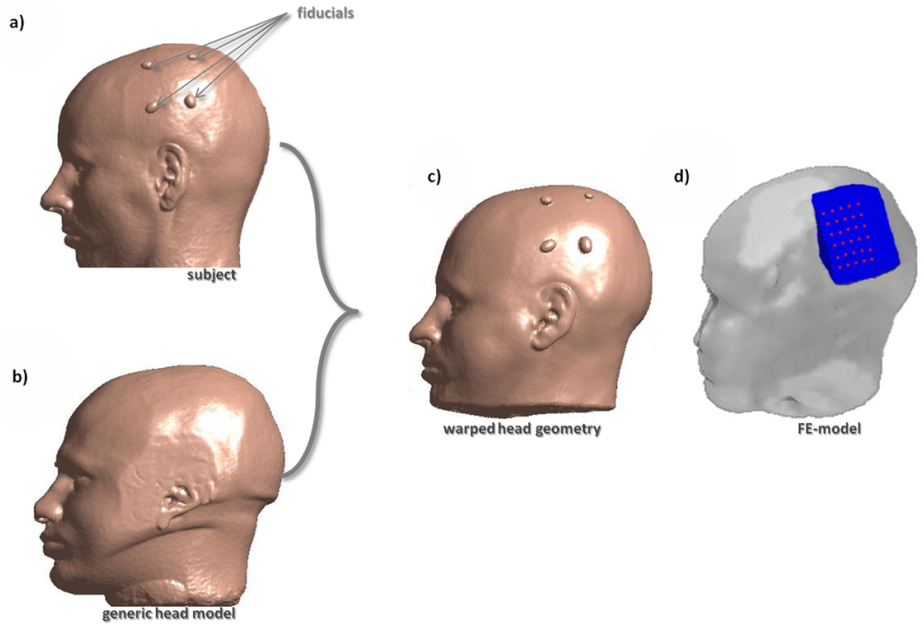

Figure 3.4: Fiduciary mark approach; transformation of the imaging grid corner positions obtained from individual MR scan to the FEM model space. (a) T1 weighted MR-scan of one subject. Corner positions of the probe pad are indicated by four spheres. (b) MR-scan of the generic brain model. (c) Subject's MR image after a spatial normalization (warping) to the generic brain model geometry. (d) The positions of 30 optical fibers are interpolated between the fiduciary marks and assigned to the finite element model boundary.

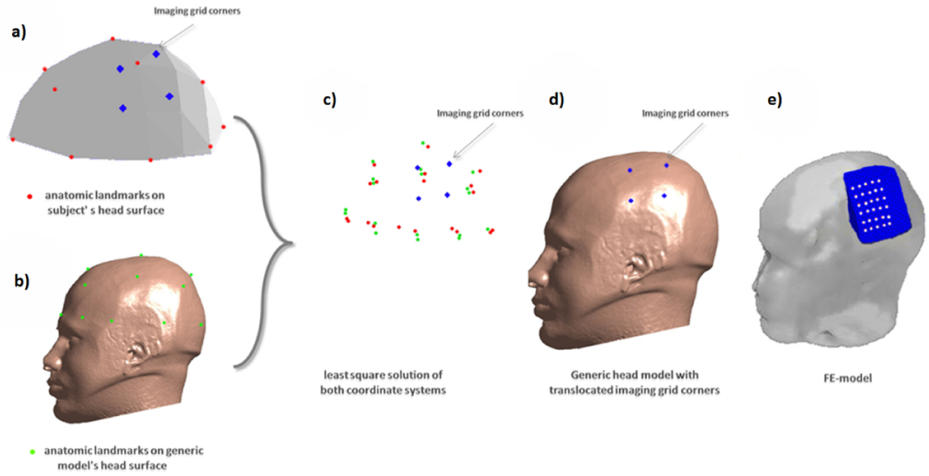

Figure 3.5: Anatomic landmark approach; transformation of the optical fiber pad corner positions to the FEM model space without individual MR scan. (*a*) 19 reference points (red dots) and coordinates of the fiber pad corners (blue dots) were acquired from the subject's head surface. (*b*) MR scan of the generic model with 19 marked reference points (green dots) derived by (Jurcak et al., 2005). (*c*) Solving the least square problem of the two coordinate systems. (*d*) The coordinates of the grid corners are now in the generic model space, the positions (blue dots) are mapped onto the model's head surface. (*e*) The positions of the optical probes are interpolated and determined on the FEM model.

3.3 The Inverse Problem

Given the measured boundary data Δy (readouts of combinations of different sources and detectors) and the sources and detectors at the tissue boundary the inverse problem of DOT is defined as finding the optical properties μ_a in every volume element.

For a reconstruction of DOT images, J needs to be inverted, which is an under-determined and ill-posed problem. First, countless distributions of μ_a within the volume can explain the same surface measurement and secondly, near infrared light can pass skin and bone but is highly attenuated with increasing depth. With a penetration depth of three to four centimeters, light reaches the cortex, but there is a vast sensitivity loss in the depth. This leads to a sparse matrix and the largest fraction of the volume contains very small sensitivity values. Furthermore, small changes in optical properties in the depth have to be recovered from boundary measurements with underlying nodes that have a high sensitivity to superficial signals and therefore make them sensitive to noise.

To reduce the problem of ill-posedness, the dimensions of J can be modulated; limiting the reconstruction volume to the field of view of the optical fibers is the most natural first step for reduction. Nodes with the lowest sensitivities in the depth can be excluded from the reconstruction, since they are unlikely to have contributed to the measurement. By choosing a higher inter-node-distance the number of nodes in the forward model is reduced, however, spatial resolution decreases. Additionally, the result space can be limited to cortical nodes but this requires exact knowledge of the underlying anatomy and therefore is appropriate for simulation studies but can only be an approximation in real-world experiments. In the following, we refer to this reduced Jacobian as $\tilde{J}$ with the dimension of $\tilde{M}$ measuring channels and $\tilde{N}$ reconstruction nodes. Naturally, in cases with no applied spatial constraints $J = \tilde{J}$ with $N = \tilde{N}$ and $M = \tilde{M}$.

3.4 Image Reconstruction Methods

To solve the inverse problem a variety of image reconstruction methods is available.

As mentioned before, image reconstruction in DOT estimates changes of the interior absorption of the brain ($\Delta\mu_a$) based on changes, which are

measured on the head surface (Δy). The reconstruction problem can be seen as linear since the aim is to recover relative changes instead of absolute concentration values. However, since the number of measurements is much smaller than the number of reconstruction nodes, the linear system Eq. 3.1 is heavily under-determined, and a unique solution for $\Delta\mu_a$ can only be obtained under additional constraints.

Alternative approaches to reconstruct brain activation are provided by developments in electrophysiological dipole mapping. Based on a volume-conducting model, the inverse problem of electroencephalography (EEG) aims at localizing the position of the active cerebral current source from measured surface fields and therefore is comparable to the inverse problem of image reconstruction in DOT.

In the following paragraphs, we review seven image reconstruction methods, which are a set of

1. widely applied linear reconstruction methods such as truncated singular value decomposition, minimum ℓ_2-norm estimates, and a depth and noise weighted variation,

2. recently proposed sparse methods (minimum ℓ_1 and a smooth minimum ℓ_0-norm estimate) (Kavuri et al., 2012; Prakash et al., 2013; Shaw and Yalavarthy, 2012b,a; Suzen et al., 2010)

3. and finally we adapt two EEG source localization algorithms and introduce them to the DOT inverse problem. More precisely, we apply the linearly constrained minimum variance (LCMV) (Van Veen et al., 1997), a scanning/beamformer method and a method for source localization using spatial flexibility (S-FLEX), which has been shown to be a good compromise between focality and smoothness and allows recovering multiple activation foci (Haufe et al., 2011).

These methods form the basis of a study which is described in chapter 4. This study simulates a cerebral DOT experiment in order to benchmark the quality of different approaches and to investigate the influence of the selected parameter for regularization.

3.4.1 Minimum ℓ_2-norm estimate (ℓ_2MNE)

Since it is computational fast and effortless, one common way of constraining the brain source activity $\Delta\mu_a$ is to penalize its norm, thereby encoding a

preference for the 'least-active' (or, least-complex) brain state that gives rise to the measurement. In the simplest case, the complexity is measured using the ℓ_2 norm. The minimum ℓ_2 norm estimate (ℓ_2MNE) of the DOT inverse problem can be written as

$$\tilde{\Delta\mu_a} = \arg\min_{\Delta\mu_a} \|\tilde{J}\Delta\mu_a - \Delta y_{\aleph}\|_2^2 + \lambda\|\Delta\mu_a\|_2^2 \tag{3.4}$$

(Hamalainen and Ilmoniemi, 1994). The solution is obtained as

$$\tilde{\Delta\mu_a} = H_\lambda \Delta y_{\aleph} \tag{3.5}$$

where $\Delta y_{\aleph}$ are the noisy measurements, λ adjusts the degree of regularization, $H_\lambda = \tilde{J}^T(\tilde{J}\tilde{J}^T + \lambda I)^{-1}$ is a pre-computable pseudo-inverse matrix, and I is the $\tilde{M} \times \tilde{M}$ identity matrix.

3.4.2 Minimum ℓ_1 -norm estimate (ℓ_1MNE)

In the EEG/MEG literature, it is often noted that linear inverses (i.e., those employing ℓ_2-norm penalties) lead to blurred images of source activity, and are furthermore unable to spatially separate multiple simultaneously active brain sites (Haufe et al., 2008, 2011). As a remedy, it is often suggested to estimate brain activation maps using ℓ_1-norm penalties. Using ℓ_1-norm penalties leads to sparse solutions, i.e., activity maps, which are zero almost everywhere. Here we consider a depth-weighted variant of the method proposed by (Matsuura and Okabe, 1995). The minimum ℓ_1-norm solution is given by

$$\tilde{\Delta\mu_a} = \arg\min_{\Delta\mu_a} \|\tilde{J}\Delta\mu_a - \Delta y_{\aleph}\|_2^2 + \lambda\|W\Delta\mu_a\|_1 \tag{3.6}$$

The weight matrix W is chosen to be the same as in Eq.3.12. The minimum of Eq.3.6 is obtained using an iterative optimization algorithm.

3.4.3 Smoothed minimum ℓ_0-norm estimate (ℓ_0MNE)

The method described in (Mohimani et al., 2009) has been applied for a cylindrical geometry for DOT in (Prakash et al., 2013). It aims at a direct minimization of the ℓ_0-norm

$$\tilde{\Delta\mu_a} = \arg\min_{\Delta\mu_a} \|\tilde{J}\Delta\mu_a - \Delta y_{\aleph}\|_2^2 + \lambda\|\Delta\mu_a\|_0 \tag{3.7}$$

Thus, it searches for the solution with the smallest number of active voxels. Since this leads to a combinatorial optimization problem, a smooth approximation of the (discontinuous) ℓ_0-norm of a vector is considered, which leads to optimizing a sequence of certain continuous cost functions. The function, which approximates ℓ_0-norm, includes an additional parameter σ, which determines the quality of the approximation in terms of balancing smoothness and sparsity of the result.

3.4.4 Truncated Singular Value Decomposition (tSVD)

The MNE solution Eq. 3.4 is defined for any positive regularization constant λ. The limit

$$\tilde{J}^{+} = \lim_{\lambda \to 0} \tilde{J}^{T}(\tilde{J}\tilde{J}^{T} + \lambda I)^{-1} \tag{3.8}$$

is called the Moore-Penrose (MP) pseudo inverse of $\tilde{J}$ The MP solution $\tilde{J}^{+}\Delta y_{\aleph}$ is the source activity with smallest ℓ_2-norm fulfilling Eq.3.1 exactly, while solutions $H_{\lambda}\Delta y_{\aleph}$ for $\lambda > 0$ generally do not explain the data perfectly anymore. The computation of $\tilde{J}^{+}$ can be performed using the singular value decomposition (SVD)

$$\tilde{J} = U\Sigma V^{T} \tag{3.9}$$

of $\tilde{J}$ where $\Sigma = diag(\sigma_1, \ldots, \sigma_{\tilde{M}})$ is a $\tilde{M} \times \tilde{M}$ diagonal matrix, $\sigma_1 \geq \ldots \geq \sigma_{\tilde{M}}$ are the singular values, U is an orthogonal $\tilde{M} \times \tilde{M}$ matrix with $U^{T}U = UU^{T} = I$ and V is an $\tilde{N} \times \tilde{M}$ matrix with $V^{T}V = I$.

The Moore-Penrose pseudoinverse of $\tilde{J}$is given by

$$\tilde{J}^{+} = V\Sigma^{-1}U^{T} \tag{3.10}$$

Similarly, for $\lambda > 0$, the SVD can be used to compute $H_{\lambda} = V(\Sigma + \lambda I^{-1})U^{T}$, and thus to solve Eq. 3.5. The formulation of $\tilde{J}^{+}$ in terms of U, Σ and V offers an alternative to regularizing the source activity using an ℓ_2 - norm penalty. Given that $\Sigma^{-1} = diag(\sigma_1^{-1}, \ldots, \sigma_{\tilde{M}}^{-1})$ it is possible to compute a reduced-rank pseudoinverse

$$\tilde{J}_{m}^{+} = V_m \Sigma_m^{-1} U_m^{T} \tag{3.11}$$

using truncated matrices V_m, Σ_m^{-1} and U_m, where the $\tilde{N} \times m$ matrix V_m and the $\tilde{M} \times m$ matrix U_m are obtained by selecting the first m rows of V

and U, respectively, and where $\Sigma_m^{-1} = diag(\sigma_1^{-1}, \ldots, \sigma_m^{-1})$ is $m \times m$.

Performing image reconstruction using $\tilde{J}_m^+$ corresponds to constraining the source estimate $\tilde{J}_m^+ \Delta y_\aleph$ to lie within the m-dimensional subspace of the brain in which brain activity contributes most strongly to the sensors.

These two methods have widely been used for image reconstruction since they are computational fast and easy to implement. One big advantage is the possibility to create a pseudo inverse of the Jacobian prior to the experiment, when fiber positions and head geometry (e.g. a head atlas) are known. This allows for a fast reconstruction within a few seconds or even an online reconstruction.

3.4.5 Weighted minimum norm estimate (wMNE)

Reconstructing activations only in those parts of the brain having a high impact on the measurements (as in tSVD) is reasonable, since doing so ensures that weak signal components (which might simply be noise) are not over-interpreted. However, one often wants to ensure that activations from different parts of the brain are equally likely to be detected. To this end, weighted minimum-norm estimates (wMNE) are employed. The idea here is to adjust the ℓ_2-norm penalty in Eq. 3.4 to compensate for the different gains activation foci have at the detector level depending on their depth. Formally, this is achieved by introducing a $\tilde{N} \times \tilde{N}$ weight matrix W in the penalty term:

$$\tilde{\Delta\mu_a} = \arg\min_{\Delta\mu_a} \|\tilde{J}\Delta\mu_a - \Delta y_\aleph\|_2^2 + \lambda\|W\Delta\mu_a\|_2^2 \tag{3.12}$$

The solution of Eq. 3.12 is given by

$$\tilde{\Delta\mu_a} = \tilde{J}^T(\tilde{J}\tilde{J}^T + \lambda W W^T)^{-1}\Delta y_\aleph \tag{3.13}$$

Here, we use a diagonal matrix $W = diag(w_1, \ldots, w_{\tilde{M}})$ the entries $w_i = S_{ii}$ of which are the diagonal of $S = \tilde{J}^T(\tilde{J}\tilde{J}^T)^{-1}\tilde{J}$ ((Haufe et al., 2008)).

3.4.6 Sparse basis field expansions (S-FLEX)

The selection of active voxels by sparse inverses tends to be unstable and highly noise-dependent. Moreover, the ℓ_1 -norm penalty prevents multiple

voxels with correlated activity to be jointly selected, which may lead to scattered solutions. To cope with these shortcomings, it has been suggested to replace sparsity in voxel domain by sparsity in a space of appropriately defined spatial basis functions (Haufe et al., 2011). The basis function dictionary of the proposed S-FLEX (sparse basis field expansion) approach consists of Gaussian blobs of different widths, centered at each voxel. Sparsifying the expansion coefficients corresponding to these blobs thus amounts to integrating the assumption that 'plausible' activation maps are composed of a small number of blob-like activities, i.e., have a simple structure. Denoting the $\tilde{N} \times K\tilde{N}$ matrix of Gaussian basis functions by G and the vector of corresponding expansion coefficients by c, where K is the number of blob widths, S-FLEX decomposes the estimated brain source activity into

$$\tilde{\Delta\mu}_a = W^{-1}G\tilde{c} \tag{3.14}$$

where W is the weight matrix defined in the section above. S-FLEX minimizes the squared deviation from the data under an additional ℓ_1 -norm constraint ensuring the sparsity of c:

$$\tilde{c} = \arg\min_c \|\tilde{J}W^{-1}Gc - \Delta y_{\aleph}\|_2^2 + \lambda\|c\|_1 \tag{3.15}$$

The minimum of Eq. 3.15 is inserted into Eq. 3.14 to yield the estimated brain activation $\tilde{\Delta\mu}_a$. Note that for $G = I$, the S-FLEX solution coincides with the weighted minimum ℓ_1-norm solution Eq.3.6.

For time series, S-FLEX estimates the brain activations at all available time points jointly under the assumption that a common set of spatial basis functions is active throughout the recording. To this end, coefficients corresponding to the same basis function but different time instants are grouped together and jointly sparsified using a so-called $\ell_{1,2}$-norm penalty (Haufe et al., 2011). Note, that without this technique, the sparsity pattern would jump from each reconstructed sample to the next, obfuscating entirely the temporal structure of the activations at the voxel level. We use the technique also for the minimum ℓ_1-norm approach. The minimum ℓ_0-norm approach, for which this problem also occurs, can however not be extended to time-series data as easily.

3.4.7 Linearly Constrained Minimum Variance (LCMV) beamformer

In contrast to the previously discussed techniques, beamforming is not concerned with estimating activity across the entire brain at once, but rather does the estimation separately for each node. To this end, activity from each voxel q is extracted by means of a designated linear spatial filter v_q, which is optimized for the given the data $\Delta y_{\aleph}$. The estimated brain activity is then obtained as $\Delta\tilde{\mu}_a = [v_1, \ldots, v_{\tilde{N}}]^T \Delta y_{\aleph}$.

The idea of the linearly constrained minimum variance (LCMV) beamformer is to construct filters, which let signals from a specific location pass with unit-gain, while suppressing all noise components (Van Veen et al., 1997). The optimal filter for location q is obtained as the solution to the optimization problem

$$\tilde{v}_q = \arg\min_{v_q} {v_q}^T C v_q \quad \text{s.t.} \quad v_q^T \tilde{J}_q = 1 \tag{3.16}$$

where C is the covariance matrix of the data $\Delta y_{\aleph}$ taken across time, and $\tilde{J}_q$ is the gain vector for the q-th voxel (the q-th column of $\tilde{J}$. The solution is obtained as

$$\tilde{v}_q = \left[\tilde{J}_q{}^T C^{-1} \tilde{J}_q\right]^{-1} \tilde{J}_q{}^T C^{-1} \tag{3.17}$$

The linear constraint $v_q^T \tilde{J}_q = 1$ here ensures that brain activity from voxel q (i.e., the signal of interest) is not damped, while the minimization of ${v_q}^T C v_q$ amounts to minimizing the overall (signal + noise) power of the projected data $v_q \Delta y_{\aleph}$. In total, Eq. 3.17 thus maximizes the signal-to-noise ratio. This, however, only holds if source activity at different voxels is uncorrelated. If there is correlated activity, the estimation of (in particular of the power of) the sources may be biased.

3.5 General Linear Model

Each of the image reconstruction procedures results in a matrix with the dimension $\tilde{N} \times samples$. The most intuitive way to detect activation is to find time courses that show the expected 'behavior' after stimulus onset, which is shown in Figure 2.2. By identifying time courses with a significantly

decreased concentration of HbR and an increased concentration of HbO_2 5-8s after stimulus onset, the activated areas can be detected. Another approach is to calculate a general linear model (GLM)

$$X = \beta P + \epsilon \tag{3.18}$$

with a model P of the expected hemodynamic response, a matrix of reconstructed time courses X , and the unexplained variance ϵ. The aim is to fit P to the reconstructed data X in order to minimize ϵ and to maximize the value of β. This fitting is usually done with a least-square approach. Application of the GLM for optical brain imaging data has been increasingly used within the last years. However, it requires an adequate knowledge about the input model function and is sensitive to over fitting and a sufficient preprocessing of the data is necessary to eliminate artifacts.

3.6 Determining reconstruction quality in simulation studies

In simulation studies aiming at benchmarking different reconstruction approaches or other aspects of the reconstruction procedure, the localization error between simulated activation and result can be estimated. This includes the focality of the result or in other words, how much the result has been spread and the positioning error of the peak value.

The most intuitive way to determine positioning error is calculating the Euclidean Distance between simulated and recovered activation. Since coordinates of both are available, their distance is calculated by applying the Pythagorean formula. Difficulties may appear when more than one target is recovered or the result is rather blurry.

A more sophisticated measure of quality takes localization errors and blur of the result into account.

The Earth Mover's Distance (EMD) (Rubner et al., 1998) is a measure of distance for two signatures, which is based on the transportation problem between a set of suppliers R (in our case the normalized histogram of the reconstruction result) and a set of costumers S (the normalized histogram of the simulation). It aims at minimizing the work F that is necessary to transform the distribution R into S given a ground distance $D = [d_{\mathrm{r,s}}]$:

$$\sum_{r\in R}\sum_{s\in S} d_{rs} f_{rs} \tag{3.19}$$

with the constraints

$$f_{\mathrm{rs}} \geq 0 \tag{3.20}$$

$$\sum_{r\in R} f_{\mathrm{rs}} = y_s \tag{3.21}$$

$$\sum_{s\in S} f_{\mathrm{rs}} \leq x_r \tag{3.22}$$

where x_r is the total supply of supplier r and y_s is the total capacity of consumer s.

The last constraint

$$\sum_{s\in S} y_s \leq \sum_{r\in R} x_r \tag{3.23}$$

is a feasibility condition, which makes sure that the total demand does not exceeds the total supply. In our case, both histograms are normalized and their total weight is 1. Having found the optimal flow F, the EMD is defined as

$$\mathrm{EMD}(R,S) = \frac{\sum_{r\in R}\sum_{s\in S} d_{rs} f_{rs}}{\sum_{s\in S} y_s}. \tag{3.24}$$

3.7 Summary

Within this work, I present new approaches that aim at determining the potential of DOT as a functional brain imaging tool. So far, I discussed typical challenges in DOT experiments such as the forward model generation and integration of the measurement space to the reconstruction space. A variety of standard algorithms for image reconstruction and additionally newly proposed methods were discussed. Those will be evaluated within the curse of the next chapter.

4 Simulation study on Algorithms for Image reconstruction

As discussed in the previous chapter, a variety of reconstruction procedures is available. However, most applied DOT studies utilize one of the linear reconstruction methods (Dehghani et al., 2009; Kavuri et al., 2012; Niu et al., 2010a; White and Culver, 2010a). Though yielding sufficiently good results, these standard algorithms tend to yield blurry rather than sharp-edged images. Furthermore, they rely on regularization to handle the rectangular and ill-conditioned nature of J. This regularization parameter is often chosen *ad hoc* and lacks objective criteria. For researchers it may be challenging to find an appropriate regularization parameter, since the measured data vary highly between experiments, depending on the setup, the imaging device, tissue properties and noise level.

This chapter presents results from an extensive simulation study which has two aims.

The first part is concerned with the problem of regularization. We demonstrate how the reconstruction quality depends on the chosen parameter when distributed source localization methods are used, thereby demonstrating the need of an independent parameter selection. This selection should be solely based on the features of the measurement data and avoid interference by the user. We illustrate that cross-validation for parameter selection allows to determine the degree of regularization automatically and data-driven and that it yields high quality results.

The second part includes an extensive evaluation of the seven image reconstruction methods, presented in section 3.4, which are a set of (I) linear reconstruction methods depending on (cross-validated) regularization, (II) noise-and depths-weighted modifications of these procedures and (III) two adapted EEG source localization algorithms. Especially sparser methods

could provide an alternative to the smooth results that are often obtained with linear methods. To our knowledge, such extensive evaluation not been performed for cerebral DOT, in which data have to be reconstructed in 3D space by relying on back-reflected light, only.

In order to provide a framework for this comparative study, we simulated a DOT measurement in a highly realistic setting. We used an atlas-based five-layered head model in combination with a real-world noise model that was added to the generated data. This noise model considers fiber distance-dependent noise levels and the spatio-temporal distribution of typical hemodynamic fluctuations.

Major parts are taken from the publication *Optimizing the Regularization for Image Reconstruction of Cerebral Diffuse Optical Tomography*, by Habermehl et al., Journal of Biomedical Optics, 2014.

4.1 Methods

4.1.1 Head Atlas and Meshing

To achieve a simulation, which is close to a real measurement we used the Montreal ICBM 2009a head atlas, an unbiased nonlinear average of 152 anatomical MR images with $1 \times 1 \times 1$mm voxel size (Fonov et al., 2011, 2009) and the corresponding tissue probability maps for cerospinal fluid, gray matter, and white matter (Collins et al., 1999). In order to receive information about scalp and skull sturctures, we additionally segmented the ICBM2009a images using mathematical morphological operations (Dogdas et al., 2005) (Figure 4.1). Based on this segmented five-layered head atlas, we used a masking and meshing software (Nirview) (Jermyn et al., 2013) to create a 3D tetrahedral finite element mesh. This mesh was then used to calculate the photon transport and thus provides the framework to simulate cortical activation and test the outcome of different reconstruction methods.

4.1.2 Forward simulation and spatial constraints

Optical fiber positions on the boundary of the FE mesh were chosen according to the setting of a previous real world cerebral DOT experiment conducted under resting conditions (Figure 4.1 (b)).

Due to the use of registration landmarks from the EEG 10-20 system and known source-detector distances, the coordinates for each fiber were known. To model light propagation, we used the Nirfast software toolbox (Dehghani et al., 2008), a Matlab-based freely available light modeling and reconstruction software. Nirfast applies the diffusion equation approximation, which is appropriate when scattering events dominate over absorption and the medium can be assumed to be an isotropic fluence field.

One challenge in DOT is the sensitivity of the measurement to signals coming from non-cortical regions. The HbO_2 specific wavelength is often contaminated with hemodynamic fluctuations from superficial veins in the scalp (Kirilina et al., 2012). On the other hand, the decrease in absorption from the HbR sensitive wavelength is highly correlated to the BOLD response in fMRI (Steinbrink et al., 2006). For this simulation study we therefore use light model and data from the HbR sensitive wavelength of 760nm. Optical properties μ_a and μ_s' were assigned to each node of the FE mesh according to Strangman and co-workers (Strangman et al., 2003).

Since the reconstruction volume was not entirely covered with the optode set, and since DOT has only a limited penetration depth of 3-4cm, we constrained J in order to reduce the result space and thus reduce the 'degree of ill-posedness'. One criterion for the exclusion of nodes was their affiliation to non-cortical tissue. Nodes belonging to scalp, skull, or cerebrospinal fluid were discarded.

To exclude 'weak' channels with very low sensitivity (e.g., due to large source-detector separation), we calculated the vector norm for all rows of J. Rows having a norm lower than 1% of the maximum value were discarded. The same procedure was performed for the mesh nodes, excluding nodes from the result space that had hardly been reached by any measuring channel.

This step reduced the result space from 256 channels to 232, and from 150,000 nodes to approx. 10,000. In the following, we refer to this reduced Jacobian as $\tilde{J}$ with the dimension of $\tilde{M}$ measuring channels and $\tilde{N}$ reconstruction nodes. Figure 4.1 (d) depicts the total sensitivity of J and Figure 4.1 (e) $\tilde{J}$, which is calculated as the sum of the sensitivity over all measurement pairs for all used nodes within the head volume.

4.1.3 Signal Generation and Noise Model

As an input signal, we modeled a hemodynamic response function (hrf) for absorption changes at 760nm peaking 5s after stimulus onset (Boynton et al.,

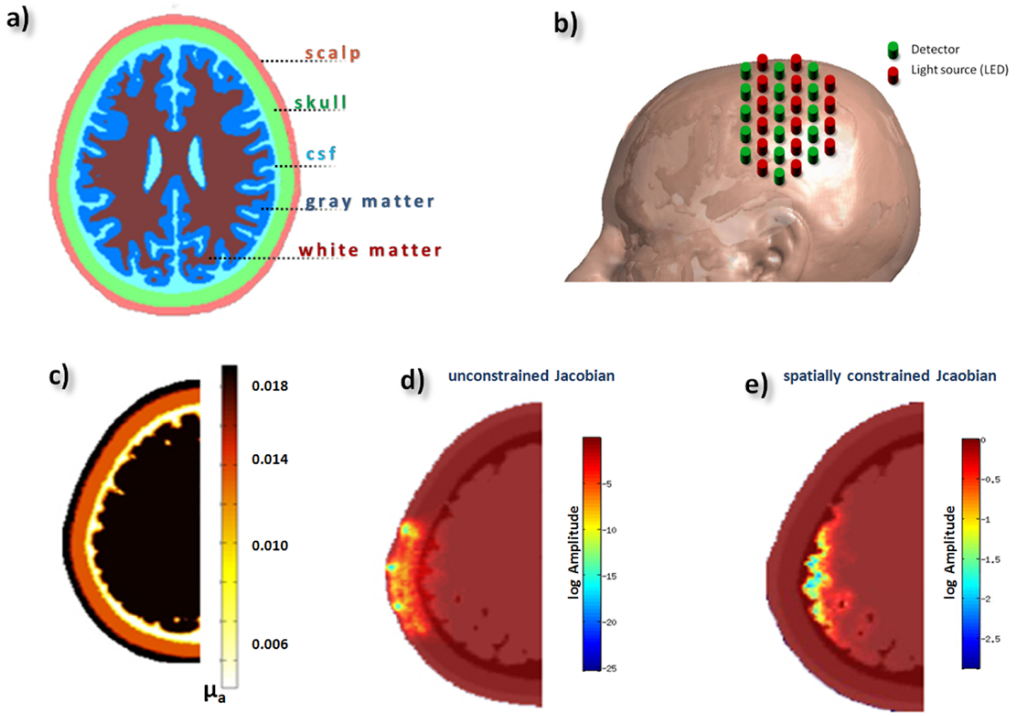

Figure 4.1: (*a*) Segmented head atlas (ICBM 2009a, a non-linear average of 152 MR images). From outer to inner layer: scalp, skull, cerebrospinal fluid, gray matter, white matter. (*b*) Sketch of the optical fiber setup as used in the forward model (1^{st} nearest neighbor distance: 13 mm. (*c*) Finite element (FE) mesh of the left hemisphere with optical properties (μ_a). (*d*) Example of the total sensitivity of an unconstrained Jacobian. (*e*) Total sensitivity of the spatially constrained Jacobian $\tilde{J}$: sensitivities for skull, scalp and CSF were set to zero.

1996), thereby mimicking a 400s experiment with a stimulus duration of 20s and an inter-stimulus interval of 20s. This was necessary for testing the linear constrained minimum variance (LCMV) beamformer reconstruction method, which requires time-series data. Moreover, it allowed us to superimpose the artificial data with realistic noise of the same dimensionality obtained from the above-mentioned resting-state recording.

Detector readings were generated as follows. A sparse matrix A_{sim} with dimension of $\tilde{N} \times \tilde{N}_{active}$ was created, where $\tilde{N}_{active}$ is the number of 'activated' nodes. Each column of A_{sim} labels one node by setting $A_{sim(l)} = 1$ at a specific location l, while all other nodes are set to '0'. The locations for these 'activated' nodes were chosen randomly, but due to restrictions of the reduced Jacobian $\tilde{J}$, all were cortical. The specific sensitivity pattern p in the activated node/nodes is defined by

$$p = \tilde{J} * A_{sim} \tag{4.1}$$

with p having the dimensions $\tilde{M} \times \tilde{N}_{active}$, and the simulated DOT measurement y is defined by the $\tilde{M} \times samples^{hrf}$ matrix

$$y = p * hrf \tag{4.2}$$

where the $\tilde{N}_{active} \times samples^{hrf}$ matrix hrf contains the activations of the simulated brain activity at the active nodes.

We applied a realistic noise model for the purpose of testing different reconstruction algorithms under natural conditions. Most studies add white noise to the data to simulate real measurements. In real life measurements, however, the noise is usually temporally and spatially correlated and not normally distributed. We typically observe a highly increased noise level for larger source and detector separations than for short distances.

Secondly, the noise often has a high fraction of hemodynamic oscillations, which often interfere with the hemodynamic response and are sometimes hard to remove. Rather than applying a random noise term, we utilized data from a 10min DOT experiment conducted under resting conditions as the noise model $\aleph$. For recording these resting state data, we used a compact tomography imager that provides up to 32 sources* 32 detectors (NIRScoutX Tomography Imager, NIRx Medizintechnik GmbH, Germany). This allowed us to achieve realistic simulation data with characteristic features of real measurements. The setup for that resting state experiment was the same as the simulation setup, so that fiber distances and orientations were preserved.

We selected the rows of the noise matrix ℵ according to the choice of channels for $\tilde{J}$ so that identical channels were used. Additionally, we took a subset of sampling/time points (columns) from ℵ , so that y and ℵ had the same dimension. Finally, ℵ and y were normalized by their respective Frobenius norms in order to calibrate artificial measurement and noise matrix. Given y, ℵ and s, where s is the signal level with a value between 0 and 1, the noisy simulated measurement $y_{\aleph}$ was constructed as

$$y_{\aleph} = ys + \aleph(1 - s) \tag{4.3}$$

According to real measurements, we low pass-filtered (first order Butterworth) the generated data with a cut-off frequency of 0.4Hz to remove cardiac signals. In Figure 4.2 (a), we see detector readings from the resting measurement for large, medium, and short source-detector separations, and the dependence of the noise level on the fiber distances.

Figure 4.2 (b) depicts examples of the generated signal for two different measurement channels, each with a signal strength of 50% ($s = 0.5$), but due to different location and source-detector-separation, the signal in the upper measurement is less dominated by noise, compared to the second example in the lower graph.

4.1.4 Automatic determination of the regularization parameter using cross-validation

Distributed inverses such as ℓ_2MNE, ℓ_1MNE, ℓ_0MNE, tSVD, wMNE, and S-FLEX estimate the source activity $\Delta\tilde{\mu}_a$ directly. This means that for an $\tilde{M} \times T$ sensor time series, $\tilde{N} \times T$ parameters have to be estimated, where $\tilde{N} >> \tilde{M}$. Under these circumstances, regularization is necessary (as outlined above). The choice of the regularization parameter crucially affects whether the fitted model is too complex (over-fitting the data), too simple (not explaining the relevant aspects of the data), or 'just right'.

Beamformers, on the other hand, are characterized by a low number of parameters. The estimation is therefore typically very stable. The LCMV beamformer (Eq. 3.17), for example, solves $\tilde{N}$ optimization problems (one for each voxel), each of which is concerned with the estimation of only a single $\tilde{M}$-dimensional filter $\tilde{v}_q$ based on the covariance matrix of a $\tilde{M} \times T$ dataset $\Delta y_{\aleph}$ where T is the number of samples, and typically $T >> \tilde{M}$.

The parameter λ of regularized models drives the estimated brain activation ($\Delta\tilde{\mu}_a$) away from the solution that explains the measurement best to

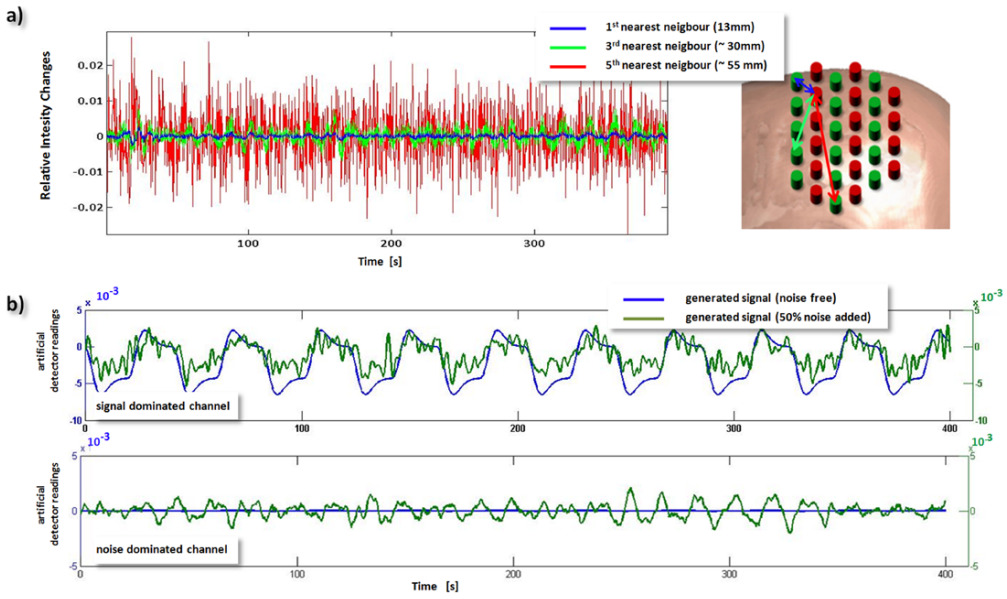

Figure 4.2: (*a*) Simulated DOT measurement with additive realistic noise recorded in resting condition using a compact tomography imager (NIRScoutX, NIRx, Medizintechnik, Germany). The noise level depends strongly on the source-detector-separation. (*b*) Two different measurement channels and generated signals with no noise (blue line) and with 50% noise (green line) added. The lower channel is noise-dominated, since the signal generated is 100 times smaller compared to the upper example. Due to different location and source-detector separation, noise has a different impact on the generated signal and may hamper the correct reconstruction.

a solution with 'simpler' structure. As such, λ critically affects the shape of the chosen solution, and the reconstruction accuracy. Choosing the 'right' amount of regularization is therefore very important. This choice should not be based on visual inspection or other subjective measures in order not to bias the later neurophysiological interpretation of the results. Rather, an automatic selection criterion is required.

One way of assessing the quality of a regularized model is to measure how well it explains unseen data, which have not been used for estimating the model parameters. This can be done using cross-validation (CV). In k-fold CV, the data is split into k chunks. The model is fitted on $k-1$ chunks, and evaluated on the remaining 'test' chunk. This procedure is repeated for each choice of the regularization parameter, and for each choice of the test chunk. The parameter explaining the test data best on average is selected, and used for training a final model based on the entire data available.

In distributed inverse source reconstruction, data folds are created by dividing the measurement channels into k sets, and the performance criterion to be estimated is the squared loss at the 'test' channels, i.e., $\|\tilde{J}^{test}\tilde{\mu_a} - \Delta y_{\aleph}^{test}\|_2^2$, where $\tilde{J}^{test}$ and $\Delta y_{\aleph}^{test}$ are the parts of $\tilde{J}$ and $\Delta y_{\aleph}$ belonging to the test channels.

For inverse methods estimating the brain activations as linear combinations of the data using some pseudo inverse $\tilde{J}_\lambda^{\#}$ (such as MNE, wMNE and tSVD), an approximation to leave-one-out cross-validation (i.e., k-fold CV with $k = M$) can be carried out in closed form. The so-called generalized CV score $g(\lambda)$ is given by

$$g(\lambda) = \frac{\|\tilde{J}\tilde{J}_\lambda^{\#} y_{\aleph} - y_{\aleph}\|_2^2}{trace(I - \tilde{J}\tilde{J}_\lambda^{\#})^2} \tag{4.4}$$

where $\tilde{J}_\lambda^{\#}$ is the pseudo-inverse constructed using the regularization parameter λ (Golub et al., 1979; Murase et al., 2004; Jagannath and Yalavarthy, 2012). The value of $g(\lambda)$ is calculated for every λ to be tested, and the parameter with minimal score is used for reconstruction.

One goal of this work is to demonstrate the dependance, of the reconstruction quality on the choice of regularization values used for the reconstruction. Methods that estimate $\Delta\mu_a$ directly are highly depending on the choice of this parameter. To visualize this relationship, we first generated one target, then added 50% noise to the artificial measurement matrix and finally we reconstructed this specific activation using a wide range of values for λ. For

every of these reconstruction result, the EMD was calculated. This procedure was repeated 50 times for ℓ_2MNE and wMNE. To test the same for tSVD, we proceed in the same manner, except that we increased the number of singular values used for reconstruction, starting with the 10 highest and ending with using all ($m = 231$).

4.1.5 Estimating the reconstruction quality

Each image reconstruction process resulted in a matrix with the dimension $\tilde{N} \times samples^{hrf}$. To estimate the quality of the result, we calculated a general linear model in a sense of a linear regression for all reconstructed time courses $x_{1,\ldots,\tilde{N}}$ with hrf as the regressor. Thus, for each voxel of the reconstruction volume a t-value was derived. All negative t-values and those with a t-value smaller than 20% of the maximum t-value were eliminated.

As a measure of quality, we employed the Earth Mover's Distance (EMD, (Rubner et al., 1998)) to the reconstruction results (t-values) of all methods as well as the Euclidean Distance between simulation and the location of the maximum t-value of the reconstruction.

4.1.6 Estimating the impact of the chosen regularization parameter

In this chapter, we want to show, how the reconstruction quality is influenced by the use of different regularization values. Methods that estimate $\Delta\mu_a$ directly are highly depending on the choice of this parameter. To visualize this relationship, we (1.) generated one activation, (2.) added 50% noise to the artificial measurement matrix and (3.)reconstructed this specific activation using a wide range of values for λ.

For every of these reconstruction results, the EMD was calculated. This procedure was repeated 50 times for MNE and wMNE. To test the same for tSVD, we proceed in the same manner, except that we increased the number of singular values for reconstruction, starting with the 10 highest and ending with using all ($m = 231$).

4.2 Results

In the following section, we quantify how the choice of the regularization parameter λ (or in case of tSVD, the number of singular values m) impacts on the effectiveness of the proposed methods . Secondly, we present simulation results that were achieved using the seven methods described above. We benchmark their performance in a realistic DOT simulation for one and two activated spots.

4.2.1 Reconstruction Quality Highly Depends on the Choice of the Regularization Parameter

To visualize the impact of the chosen value for regularization, Figure 4.3 depicts an example of reconstruction for tSVD, where the activation was recovered using different numbers of singular values for the inversion of $\tilde{J}$.

Figure 4.3 (b) shows the best possible reconstruction result for this simulation with the lowest EMD (number of singular values $m = 30$). The result that was achieved when the number of singular values was determined automatically by cross-validation ($m = 60$) is shown in Figure 4.3 (c). Both parameters resolve the activation reasonably well with a correct location and little blur. The result with an arbitrarily chosen high number of singular values (m=160, see Figure 4.3 (d)) leads to over-fitting, which is evident from a high number of phantom activations.

Figure 4.4 depicts multiple graphs, each representing one of the distributed reconstruction methods used. The red solid line shows the mean EMD for 50 different simulations and a wide range of values for λ (increasing number of singular values m for tSVD, respectively). The red transparent area represents the standard error of the mean and the blue area the standard deviation. In all quality plots, we see clearly how EMD alters with the different regularization parameter. We find a high EMD when very small or very high regularization values are chosen, rendering data that are either over- or under-fitted. Between them, we find a global minimum, which is indicated by the red dot representing the best possible EMD.

Assuming that the location of this minimum would be known prior to reconstruction, this λ (m, respectively) would be the first choice for parameter selection. However, in real world experiments the true location and extent of the activation is unknown and such a plot is not available. For overcom-

ing this challenge, this optimum is approximated by CV as described in the section above. The blue dots in each subplot indicate the mean value for λ (m, respectively) estimated using CV and the respective mean EMD. In all three methods, the cross-validated value leads to results that are comparable in quality to the best possible result.

Please note that since ℓ_1MNE, ℓ_0MNE and S-FLEX cannot be solved in closed form and rely on numerical optimization, calculation time for such a large number of variations was unreasonably high. Results for these methods are therefore not shown here. In practice, we choose the regularization strengths for these methods indirectly by selecting λ such that the data is explained to the same extent as it is explained by wMNE using a cross-validated λ. The LCMV beamformer is also omitted here, since it does not depend on the choice of a regularization parameter in the same way as do the other methods, as mentioned above.

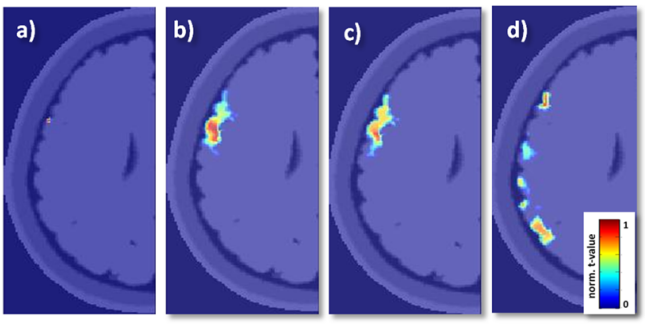

Figure 4.3: Example for image reconstruction using tSVD and with different numbers of singular values used for inversion of $\tilde{J}$ (a) Simulated target activation. (b) Result using 30 used singular values for reconstruction ($EMD = 12.6$, best possible result). (c) Result using (cross-validated) 60 singular values ($EMD = 15.1$). (d) Result from reconstruction with 160 singular values ($EMD = 57.3$).

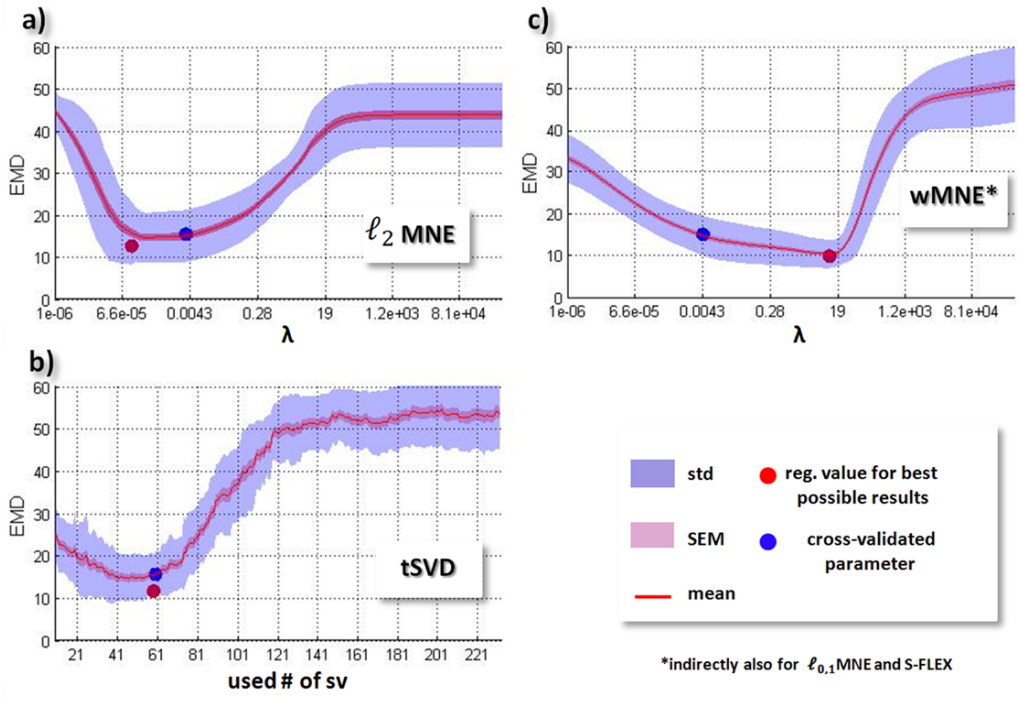

Figure 4.4: Depiction of the relation between regularization and reconstruction quality of three distributed reconstruction methods (noisy data, one activated spot). (*a*) Result for ℓ_2MNE. In each simulation run, the activation was reconstructed using 100 different regularization parameters. The red line depicts the average EMD for 50 simulation runs. The geometric mean of the best possible regularization value (red dot) and the same for the automatically detected (cross-validated) (blue dot) and their respective mean EMD. (*b*) Reconstruction quality for tSVD using an increasing number of singular values for reconstruction. (*c*) Result for wMNE.

4.2.2 LCMV Beamforming resolves single activation spots best.

The second focus of this chapter is on benchmarking source reconstruction methods, among which are frequently used methods, recently proposed sparse algorithms, and EEG-source localization methods. All methods are described in detail in section 3.4.

Figure 4.5 gives an impression of the simulation and the reconstruction result with the seven reviewed methods for a single spot activation in a single case. For visualization, we show transverse cross sections covering the area of the simulated activation.

The arrow in Fig 4.5 (a) indicates the node that was set 'active'. Rows 1-7 in Figure 4.5 (b) show the reconstructed images for all tested methods in a noise-free simulation. Within each row, the EMD between simulation and result is pointed out in the last column. Figure 4.5 (c) shows the same simulation but with 50% noise in the data.

For ℓ_2MNE, tSVD, and wMNE we find a relatively good localization of the peak activation with slight blurring in the noise-free simulation. This blurring increases when noise is added to the data. Compared to ℓ_2MNE, wMNE shows an increased sparsity and a lower EMD. S-FLEX and ℓ_1MNE show small positioning errors in the noisy case and a focal result. In both noise levels, we find ideal results for LCMV, with no displacement, and a high focality. All the latter three methods appear to be rather insensitive to the applied noise level. ℓ_0MNE performs well in the noise-free case but fails when noise is added to the data.

For an overall comparison of all methods, the average EMD of 100 simulations with one activated spot and four different noise levels (0%, 25%, 50%, and 75%) can be found in Figure 4.6 (a) and the respective mean Euclidean distance between simulation and maximum value of the reconstruction result can be found in Figure 4.6 (b).

Similar to the single case we find the best reconstruction at every noise level when LCMV is used. In almost all simulations, the beamformer achieves a correct positioning with minimal blurring even at the highest noise level. S-FLEX and ℓ_1MNE perform well and recover sparse results; however, their results are dislocated by a few millimeters. Interestingly, S-FLEX and ℓ_1MNE do not achieve their best EMD scores at the lowest noise levels with high signal level s (see Eq. 4.3). This may be due to the fact that for efficiency reasons the optimization for both methods is stopped after the data have

been fitted with a goodness-of-fit of $gof = 0.95$, where $gof = 1 - \|\tilde{J}\Delta\tilde{\mu}_a - \Delta y_{\aleph}\|_2 / \|\Delta y_{\aleph}\|_2$ The data may thus be insufficiently fitted for very low noise levels.

ℓ_2MNE, tSVD, and wMNE show a clear dependence on the noise level: With higher noise, their respective EMD increases. This can be observed especially in tSVD. However, although reaching a high EMD, tSVD still shows only a small positioning error (Euclidean distance) between the peak value of the reconstruction and the simulation (Figure 4.6 (b)); within the highest noise level, the average Euclidean distance between result and simulation is 8.3mm (ℓ_2MNE: 15mm, wMNE: 11mm, LCMV: 0.2mm, S-FLEX: 10.1mm, ℓ_1MNE: 8.8mm).

This implies that the main reason for high EMD is a higher blur level rather than malpositioning; this blur could possibly be reduced by thresholding the result. The highest sensitivity to noise is found in ℓ_0MNE: From low noise levels, the EMD and the positioning error increase dramatically.

4.2.3 Minimum ℓ_1 -norm achieves best result when two spots are active

When investigating a relatively small area of the brain there is often only one spot of activation within the probe. Nevertheless, there are approaches where larger areas or even the whole head are scanned.

When the medium is larger, the possibility of including two or more areas with simultaneously fluctuating rhythms caused by a synchronic hemodynamic answer rises. We therefore simulated two additional areas with perfectly correlated activity in the brain.

Recovering two (or more) activation foci in an algorithm is a challenge. TSVD, ℓ_2MNE, and wMNE show no significant differences in their EMD which is attributable to the generally increased level of blur. That makes it harder to distinguish the quality using the EMD method.

Nevertheless, when looking at single cases with visualized reconstruction results (Figure 4.7), we can see that all methods except the beamformer are capable of recovering both activations. Since ℓ_1MNE can reconstruct sparser activation patches than the other methods, its performance is better, though, again some slight positioning errors do occur. At lower noise levels, S-FLEX yields results comparable to those of ℓ_1MNE but their quality decreases at the highest noise levels. ℓ_0MNE can recover both targets almost perfectly in a noise-free dataset, but fails again when noise is added. Due to reduced blur, wMNE shows a slight but not significant advantage over ℓ_2MNE, and with increased noise levels also over tSVD. Finally, it is obvious that the LCMV beamformer cannot resolve correlated activity at different brain sites, and therefore highly decreases in performance .

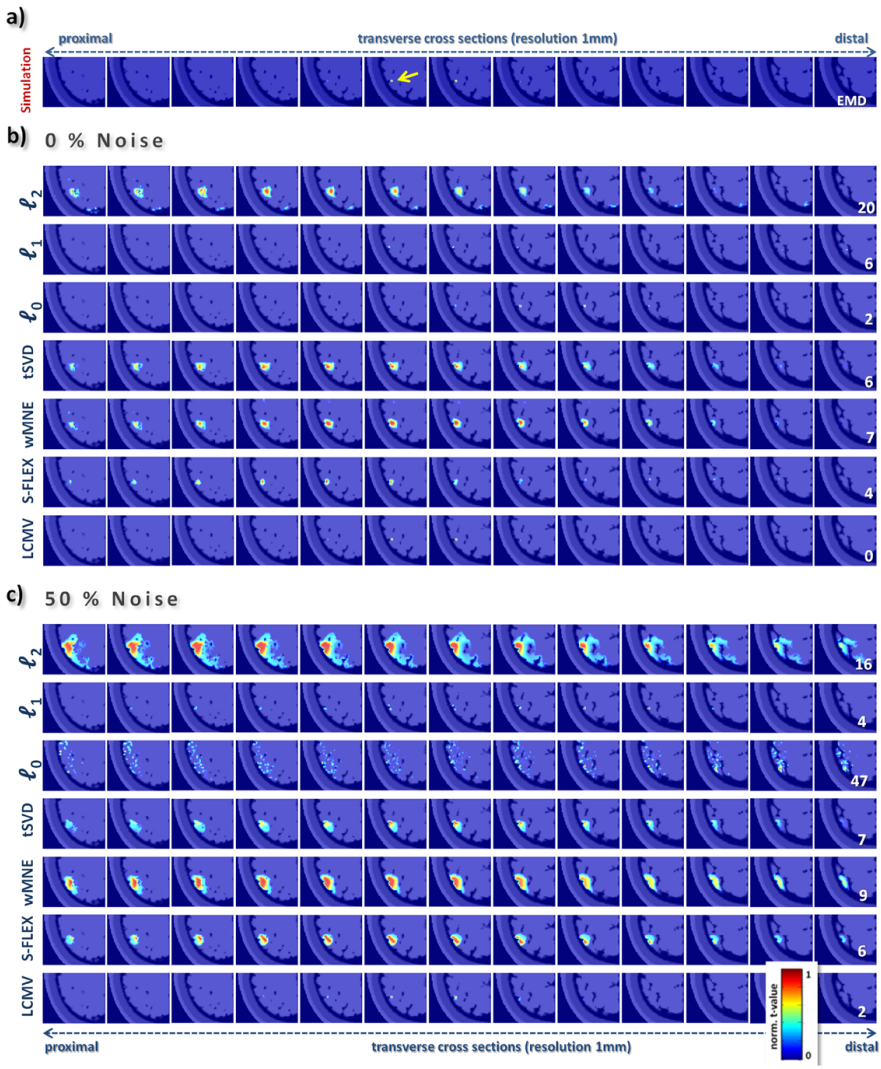

Figure 4.5: Exemplary reconstruction images for a single spot activation. (*a*) Transversal slices of the reconstruction volume with the simulated activation in column 6. The other columns depict transverse cross sections adjacent to the central layer (z-direction, slice depth: 1mm). (*b*) Reconstruction result for a 0% noise level. Each row represents the result from one particular reconstruction method. The number in the right column indicates the Earth Movers Distance (EMD) for this specific example. (*c*) 50% noise added to the data.

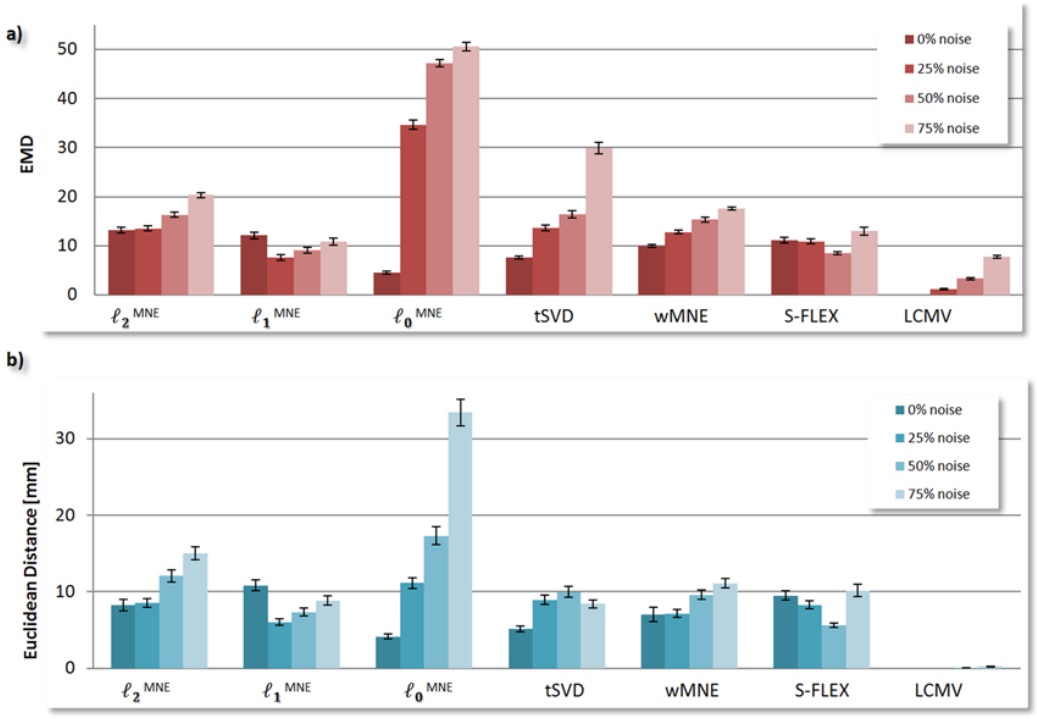

Figure 4.6: (*a*) Overall EMD statistics for single spot activation, four applied noise levels and all seven reconstruction methods. (*b*) Averaged Euclidean Distance between simulated target and maximum value of the result in mm for all methods and noise levels. Black bar indicates standard error of mean.

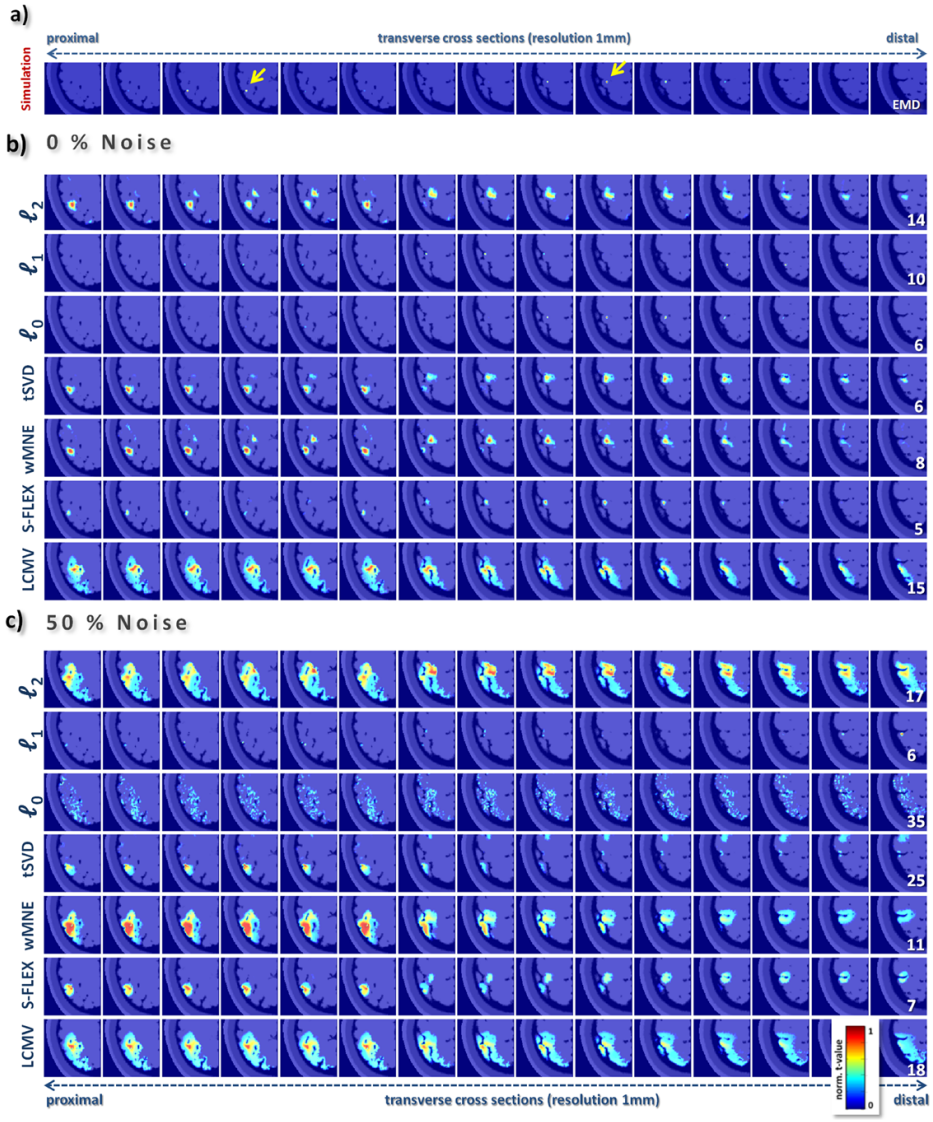

Figure 4.7: 7 Exemplary reconstruction images for two activations. (*a*) Simulated activation: two nodes in different locations were defined as 'active' (indicated by the arrow). (*b*) Reconstruction results for noise-free data and from seven different reconstruction algorithms (*c*) Results for noisy data (50%). Columns represent transverse cross sections of the reconstruction volume (z-direction, slice depth: 1mm).

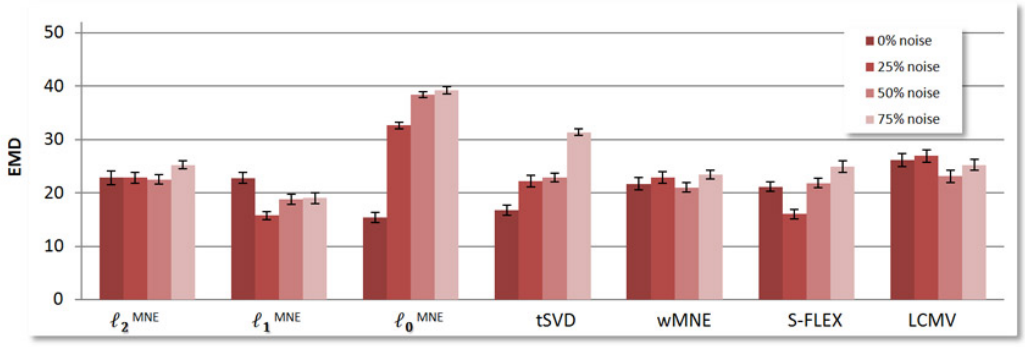

Figure 4.8: Overall EMD statistics (n=100) for all seven methods and four different noise levels and two activated spots. Black bar indicates standard error of mean.

4.3 Discussion

We conducted this simulation study to illustrate how image reconstruction methods depend on the regularization parameters chosen, and to benchmark a wide range of reconstruction procedures for cerebral DOT in a semi-infinite medium. To our knowledge, such an extensive study had not yet been performed.

The implementation aimed at mimicking a most realistic environment for DOT measurements. However, assumptions of the nature of the used medium had to be made. For instance, the choice of optical properties to model light propergation in the head were intermediate values, since their true values alter and a variety of values have been reported (Bevilacqua et al., 1999; Okada et al., 1997; Torricelli et al., 2001). Furthermore, Choi et al. (2004) reported an decreasing scattering coefficient when looking at larger optode distances (reflecting deeper tissue) which is in contrast to the values used from Strangman et al. (2003) assuming an increasing value for μ_s'.

For a most realistic data generation, we added noise originating from a real world experiment, including all the specific features such as hemodynamic fluctuations and fiber distance-dependent noise levels that can influence reconstruction quality. This allowed the generation of data sets, to be recorded in psycho-physiological experiments, while at the same time allowing for a direct assessment of the reconstruction quality. In contrast to other studies (Prakash et al., 2013; Shaw and Yalavarthy, 2012a), all methods were tested on a semi-infinite medium. This geometry can rely on back-reflected light only and there might be differences to the usually used circles or cylinders where light is applied from all sides.

Since experimental setups and imaging devices alter between experiments and labs, parameters such as regularization values should be determined for every reconstruction in a data-dependent (and user-independent) way. In this work, we demonstrated that cross-validation is able to ascertain the degree of regularization required for a good balance between data and noise. It can be easily implemented within the reconstruction routine and leads to high-quality results by relying solely on the measurement and the Jacobian. Cross-validation is one of the most popular methods for model selection due to its high robustness and stability. Note, however, that CV assumes stationarity and i.i.d. (independent and identically distributed) properties of the underlying data. In the setup of the present study, both assumptions

are fulfilled: (1) Even though different channels are left out, the reconstruction of the signal on the remaining channels follows the overall distribution without causing non-stationarity (Sugiyama et al., 2007) and (2) Due to the low spatial range of NIRS it can be safely assumed that the data is spatially independent.

Linear methods such as tSVD and ℓ_2MNE are widely used in cerebral DOT and NIRS experiments or phantom studies, because they allow for fast or even real-time volumetric image reconstruction of time series. However, they often provide heavily blurred images, in which the true activation may be indistinguishable. To overcome this drawback, sparse methods such as ℓ_1MNE or S-FLEX may be used. These methods prefer spatially focal results and they have proved able to distinguish multiple activation foci. They have provided good results regardless of the number of activated spots within a medium noise level. Besides the promising results for sparse methods, some aspects may also hamper their application. The most important is that they are nonlinear in the data. Thus, unlike the linear methods, they cannot be implemented as a multiplication of the data matrix with a precalculated pseudoinverse matrix, but rather require iterative optimization for each new data point or chunk. This makes these algorithms unsuitable for online use, and even hard to apply to large data recordings (such as psychophysiological experiments) at all. An increased number of measuring channels and/or a higher reconstruction resolution will increase the reconstruction time dramatically.

As a further sparse method, we tested ℓ_0MNE, which failed to reconstruct noisy data properly. In contrast to S-FLEX or ℓ_1MNE, the proposed implementation of ℓ_0MNE lacks the potential to treat time series in its entirety. Since the inverse solution is recalculated for every time point, the sparsity patterns vary likewise. The performance could probably be improved if the activation is localized for one entire time series (rather than one sample at a time) with the constraint that identical voxels must be chosen for the whole time course, as was the case in implementing for S-FLEX or ℓ_1MNE.

In addition to the distributed imaging approaches discussed above, we also introduced the linearly constrained minimum variance (LCMV) beamformer, another reconstruction method used in the EEG field (although originally developed for radar arrays), which provides linear filters for transforming sensor measurements into source activations, and can thus be applied efficiently just like tSVD, ℓ_2MNE and wMNE. Although LCMV provides a filter matrix of the size of a pseudoinverse of $\tilde{J}$, it technically does not provide a solution to

the general forward equation. This means that certain parts of the measured data may not be explained at all, while the variance in other components may be accounted for many times in different voxels. The reason for this behaviour lies in the beamformer's property of modeling the activation at each voxel separately. Consequently, it shows excellent results when only one brain area is active, or when multiple brain sites show uncorrelated activation, but it is unable to deal with correlated source signals. Furthermore, in contrast to all other methods, LCMV filters must be computed from a large amount of data. This prohibits the localization of single measurement samples and hampers straightforward online application. Its broad utilization in functional brain imaging experiments with potentially multiple correlated sources of activation has to be considered carefully regarding paradigm, imaging setup and the presumed area(s) of activation.

Besides the implemented methods, a huge variety of other source localization algorithms exist. A few of them are mentioned here, such as the sub-space preconditioned least square root (SP-LSQR) (Jacobsen et al., 2003), the generalized Tikhonov regularization (GTR), GTR in combination with the L-curve criterion (GTR-MLCC) (Salehi Ravesh et al., 2013), ℓ_1/ℓ_2-norm estimate (group lasso), $\ell_1+\ell_1/\ell_2$ (sparse group lasso) (Montoya-Martinez et al., 2012), a total variation (TV) regularization (Fan, 2012), and a time-frequency mixed-norm estimate (TF-MxNE) (Gramfort et al., 2013) that uses time-frequency analysis for regularization.

With this work, we performed a highly realistic simulation of a functional brain imaging study with cerebral DOT in humans which is performed on a whole multi-layered finite element model of the human head. A choice of volumetric image reconstruction approaches were benchmarked including two recent methods for EEG source localization. We showed that linear reconstruction methods provide fast and adequate results. However, its accuracy can be increased by implementing sparse algorithms, albeit at the expense of computational time and effort. Using this presented framework, a robust system for cerebral DOT can be established and the necessary model parameters can be selected with the CV approach.

5 *In Vivo* Functional Brain Imaging: Exploring the Lateral Resolution

The next chapters will focus on *in vivo* capabilities of functional DOT. The study, which is described now aims at investigating the capability and limits of DOT to increase the spatial resolution in optical brain imaging. Wide parts of this section have been published in Habermehl et al.: *'Somatosensory activation of two fingers can be discriminated with ultrahigh-density diffuse optical tomography'*, Neuroimage, 2012 (Habermehl et al., 2012).

As already mentioned, the spatial resolution of fNIRS with its topographic approach is limited to several centimeters. Figure 5.1 depicts a result (significant decreased HbR concentration) for a motor task of the left hand. This rather rough activation map is obtained with the 2D back-projection scheme when few optical fibers are used.

A better resolution may not be required for many applications, but within the clinical setting it might be required. For example, monitoring the patient's progress in recovery and rehabilitation by investigating changes of cortical function requires a higher spatial resolution than conventional fNIRS can provide.

In this chapter, we show that for demanding functional mapping tasks, such as demonstrated on the somatosensory system, DOT in conjunction with high spatial sampling significantly improves the spatial resolution. Furthermore we show, that it is essential to visualize and distinguish very small activation patterns. In contrast to many studies focusing on the primary motor-system (Boas et al., 2004; Franceschini et al., 2003; Joseph et al., 2006) or primary/secondary visual system (Liao et al., 2010; White and Culver, 2010b; Zeff et al., 2007), we are only aware of two reports on somatosensory

studies with NIRS (Custo et al., 2010; Franceschini et al., 2003), both using a median nerve stimulation procedure.

The primary somatosensory cortex (SI) was chosen here as a model system for several reasons: The superficial location at the posterior wall of the central sulcus makes it easily accessible to DOT measurements. Activations within SI are of small extent with short distances between representational areas of the fingers of one hand, suitable to demonstrate the need for and the benefit of high spatially resolved optical imaging. Furthermore, the highly individual and variable representational distribution provides a challenge and an interesting quality assessment for the comparison between NIRS and fMRI activations. And finally, beyond pure and basic research, there may be relevant future clinical applications in neurorehabilitation and rehabilitation monitoring, e.g. in stroke patients by assessing cortical neuronal plasticity.

In previous fMRI studies, finger representations have been confirmed to be localized within the contra lateral postcentral gyrus and to show a somatotopic arrangement; generally, the first finger (thumb, d1) is represented in the most lateral, anterior and inferior position, with the other finger representations following in a superior medial direction along the central sulcus (Kurth et al., 2000; Maldjian et al., 1999; Weibull et al., 2008). Repeated measurements show comparable results for individual subjects. However, there is high inter-individual variability in somatotopic arrangement as well as in hemodynamic response strength (Kurth et al., 2000; Schweizer et al.,

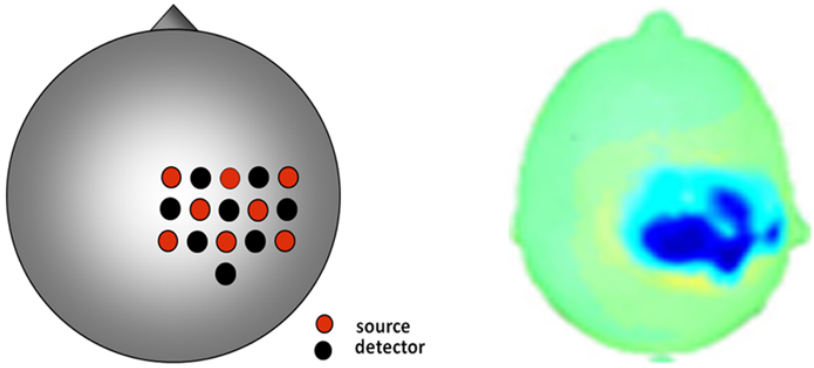

Figure 5.1: Example for optical fiber placement in fNIRS (left) and the obtained activation map for a motor task of the left hand.

2008).

In this study, we extended our previously published results on vibrotactile finger stimulation (Koch et al., 2010) towards the comparison of classical topographic image generation and a three-dimensional image reconstruction. Additionally, the same subjects underwent fMRI using the same experimental design to compare the functional activations of both imaging modalities. Finally, the individual position of optical fibers in the forward model were taken into account in the current study allowing to co-register volumes of functional activation with the individual anatomy.

fNIRS still is exceedingly used in brain research compared to optical tomography. In this study, we show that there are applications where the three-dimensional tomographic approach is essential to image brain activity: with a topographic setup or even with a conventionally dense tomographic setup the specific activation foci cannot be distinguished properly. Furthermore, we demonstrate that our imaging and reconstruction procedure is able to separate cortical answers to different stimuli not only laterally but also transversely, with the activation pattern being found in different tissue depths. Additionally, we show that DOT and 3T fMRI as tools of functional brain imaging in humans yield comparable results.

In contrast to other groups, e.g.(Zeff et al., 2007) that use fiber grids with a minimum SD separation of 13mm and fibers that are separated sources and detectors (not co-located) we applied a tighter fiber arrangement (see section 5.1), exceeding the sampling density of other multi-distance approaches. In the following, we refer to this strategy as *ultrahigh-density* DOT.

5.1 Methods

5.1.1 Subjects and Stimulus Procedure

We investigated eight healthy right-handed volunteers (mean age 26.8 ± 4.6 years, 2 female) who had no history of any neurological disease. Written consent was obtained from each volunteer prior to the experiment. Subjects were monetarily rewarded for their participation. The study was approved of by the local ethic committee.

Volunteers underwent vibrotactile stimulation of the 1^{st} (thumb, d1) and 5^{th} finger (little finger, d5) of their right hand using a piezoelectric transducer (model PL-127.251, PI Ceramic) with a flat semicircle-shaped rubber pad

(diameter: 13mm); the frequency of the vibration was 40Hz. The transducer was gently fixed at the participant's fingertips with adhesive tape to assure the correct position throughout the experiment. D1 and d5 were stimulated 40 times each. Stimulation periods of 20s were separated by resting periods of equal length. The sequence of d1 and d5 stimulation was pseudo-randomized but identical for all subjects and for both the DOT and the fMRI sessions. For DOT measurement, the subjects sat in a chair in a dimly-lit, silent room. The fMRI measurement was performed in supine position. Except from the position, the stimulation procedure was identical for both, the DOT and the fMRI experiments. In addition to the fMRI measurements in a 3T scanner, which was performed on a subsequent day after the DOT measurements we acquired an anatomical MRI in a 1.5T scanner just prior to the DOT session in each participant. For a schematic of the experimental setup see Figure 5.2.

For each subject four data sets were acquired: (i) a 1.5T anatomical scan prior to (ii) the DOT measurement, (iii) a 3T functional and (iv) anatomical MRI measurement.

5.1.2 Optical Data Acquisition

We used a DYNOT 232 instrument (NIRx Medizintechnik GmbH, Berlin, Germany) to acquire the DOT data. The system performs continuous-wave measurements using two frequency-encoded laser sources at 760nm and 830nm with a sampling rate of 1.8Hz in a time-multiplexed scanning fashion. The instrument employs an optical switch to provide a large number of illumination sites in a sequential illumination fashion. In conjunction with dynamic gain switching of the optical detectors, this provides the very high dynamic measurement range needed for diffuse-tomographic multi-distance measurements. Details of the measuring system can be found elsewhere (Schmitz et al., 2002). In this specific study DOT measurements used 30fiber-optic probes (optodes). Each optode can act as a source and as a detector, thereby providing 900 combinations, each entering the analysis as one optical data channel. The optodes were arranged in a rectangular grid of 6×5 probe positions, with a center-to-center distance of 7.5mm for neighboring optodes (Figure 5.2 (b)). Because of the co-located source-detector design and the tight fiber arrangement, our setup allows for uniquely dense spatial sampling, from 0mm (i.e, co-located) to about 30mm source-detector distance.

Because the spatial sampling density is much higher than in other to-

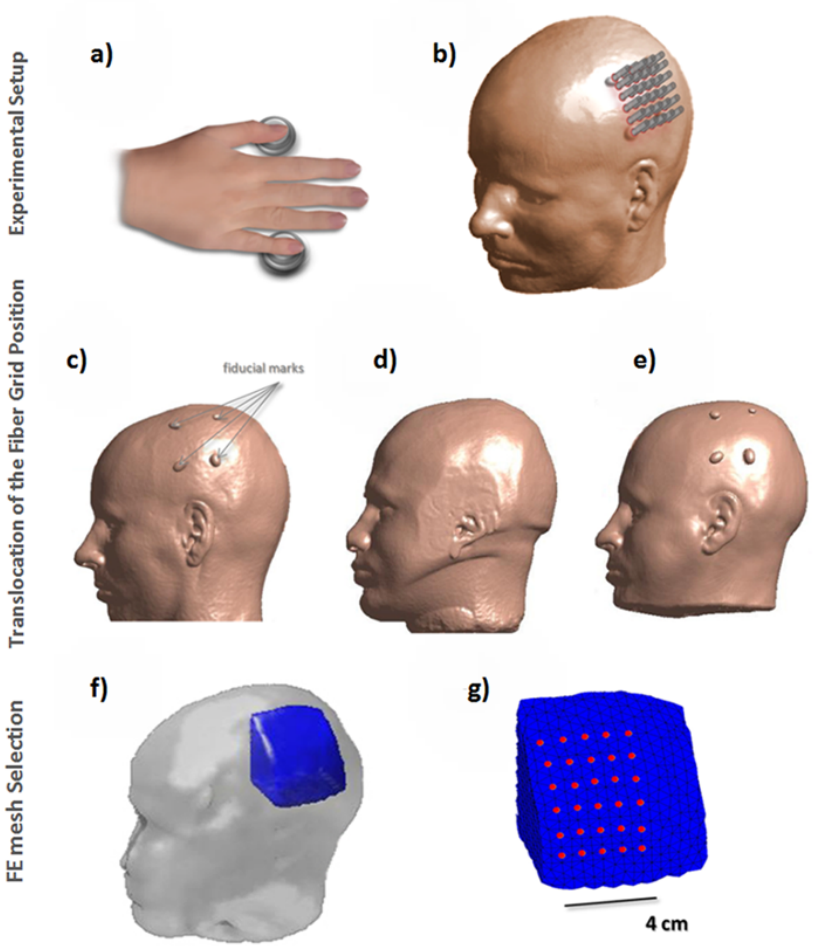

Figure 5.2: (*a*) Experimental setup: The fingers d1 and d5 of the right hand were stimulated by piezoelectric vibration devices. (*b*) 30 optical fibers (inter-optode distance 7.5mm) were placed around C3. The positions of the fiber grid corners were marked with vitamin E capsules (*c*) Fiduciary mark approach for co-registration: subject's MR scan in the real world space with the fiduciary marks on the head surface. (*d*) Anatomic MR scan of the generic head atlas on which the FE mesh is based. (*e*) Subject's MR scan, warped into space and shape of the atlas. (*f*) Atlas with a sub-mesh (blue) of the FE model, covering the area of interest. (*g*) Within the sub-mesh, the locations of the optical fibers (red dots) on the boundary were defined individually for each subject.

mographic or multi-distance approaches (e.g. minimum SD distance 19mm: (Boas et al., 2004), 13mm: (Zeff et al., 2007; Gregg et al., 2010)), we refer to this strategy as *ultrahigh-density* DOT.

The instrument's rigid scaffolding head gear employs individual spring-loaded mounts of the fiber tips and allows parting of the subject's hair. It provides a stable optical contact to the skin to minimize artifacts from mechanical instabilities or subject motion. Since the activation for finger stimulation is expected to be located over the left, post-central gyrus, contralateral to the stimulated hand, we located the probe grid around the C3 position relating to the 10-20 System (Klem et al., 1999).

5.1.3 Forward Model

Co-registration of the individual optode-positions and the cortical anatomy required three steps, using the fiduciary marks approach (Figure 5.2, which is described in detail in section 3.2.2.

To create the Jacobian matrix J we used the BrainModeler tool of the NIRx NAVI imaging suite, which is implemented in MATLAB (The MathWorks, Natick, MA, USA). The mesh was based on a brain atlas, obtained by an anatomical MR scan with 1mm resolution. For each of these meshes there are approx. 400 boundary nodes on the head surface with a spatial resolution of 4mm. These surface nodes are considered as potential source/detector positions and the FEM discretized photon diffusion equation using Type III boundary condition (Paulsen and Jiang, 1995) was solved for each sub-mesh, providing the reference detector values and the weight function, respectively. The forward solution was computed based on the simplified assumption of homogenous interior optical properties ($\mu_a = 0.06\text{cm}^{-1}$ and $\mu_s = 10\text{cm}^{-1}$).

We selected the sub-mesh that best approximated the area of our measurements, according to the translocated positions of the fiber grid. This sub-mesh was used for all subjects and contains 3884 nodes and 16772 tetrahedrons with a dimension of $60 \times 71 \times 78$mm (depth $\times$ width $\times$ height). Because the fiber positions within the mesh varied between subjects, we individually assigned the positions of the optical fibers to the mesh for each participant. A further limitation of the reconstruction space by means of spatial constraints was omitted due to the nature of the generic head model.

5.1.4 Image Reconstruction

Raw data were band-pass filtered between 0.016 and 0.4Hz to attenuate physiological noise (very slow fluctuations and pulse). Data channels exceeding a noise level of 15% (coefficient of variation) were excluded from further analysis. For seven of the eight participants all 900 data channels were retained for image reconstruction. For the remaining participant (subject 5) 84 channels exceeded the noise level and were discarded, so that 816 channels were used for the image reconstruction. Due to the better fiber-skin contact in all other subjects, we observed inferior data quality in this subject, as judged by the variance of the raw data. We are aware that the threshold of 15% is a rather weak criterion allowing most of the channels to be used for reconstruction, but the main procedure defining 'activated DOT voxels' is the t-test after image reconstruction (see below). It separates DOT voxels showing real activation over a longer period after stimulus onset from those that fluctuates randomly.

When looking at different source-detector separations (e.g., 7.5mm vs. 30mm) we did observe deterioration of data quality with increasing distances but this was limited to few channels still not reaching the 15% level. Consistently we observed a slightly better signal-to-noise level in data measured with 760nm (to which HbR contributes more).

We obtained images of hemodynamic changes using the normalized difference method (Pei et al., 2001) in which differences between predicted and measured surface data are related to changes of interior optical properties (e.g. absorption) of the investigated medium compared to a reference medium (perturbation approach). To make the weight matrix J more uniform and less ill-conditioned, and to suppress numerical errors and accelerate convergence, J was scaled by normalizing the column vectors to their respective mean values. No constraints or weightings concerning the reconstruction space (e.g. limiting it to cortical nodes) were made. The inversion was then calculated by performing a truncated singular value decomposition which has been shown to reconstruct large time series of from very high number of optical data channels computational efficient and sufficiently precise (see section 3.4.4).

5.1.5 Statistics

To identify DOT voxels with a stimulus-related hemodynamic response, t-tests between a baseline interval from -10 to -1s and the stimulus interval from 13 to 20s both with regard to stimulus onset were calculated. Within this functional study, we focus on changes in HbR, which we regard the more reliable indicator of a hemodynamic response in the brain's cortex. HbO_2 is often confounded by superficial tissue signaling such as blood pressure (Franceschini et al., 2003) and other global (i.e., non-task specific) hemodynamics (Kirilina et al., 2012).

Since the activation-induced increase in regional cerebral blood flow overcompensates the regional increase in oxygen uptake (Fox and Raichle, 1986) a decrease in HbR is expected (see Figure 2.2 on page 8). Negative t-values in the HbR maps therefore indicate activation in the respective DOT voxel. Due to the expected small activations and a high inter-subject variability, activation data were evaluated on single subject level. We did not use the same cutoff-value for all subjects and conditions, but determined individual thresholds, since the different signal amplitudes and signal-to-noise levels were determined. The t-values ranged between 70% and 90% of the maximum t-value. Only DOT voxels with values below this threshold are displayed as 'active'.

The NAVI software provides the reconstructed images in a 2D array, which contains a time series of the whole experiment for each node of the FE mesh. All statistical calculations were performed on this 2D-array and then transformed into Cartesian 3D space using an interpolation routine from MATLAB (The Mathworks, Natick, MA, USA).

5.1.6 Topographic and sparse tomographic analysis

We sought to test the hypothesis that tomographic imaging renders a better and more adequate representation of the activation pattern in the somatosensory cortex than topographic NIRS. To allow a direct comparison of a topographic, a sparse tomographic, and a dense tomographic approach in the same data sets, we defined a subset of second nearest neighbor (2NN) source detector combinations mimicking a topographic set-up.

This topographic approach was based on five sources and four detectors which were not co-located. Similar to the tomographic setting, data were band pass filtered at 0.016-0.4 Hz. To compute concentration changes in

HbO_2 and HbR we used a modified Beer-Lambert law as is usually done in topographic approaches (Cope et al., 1988). Statistical inference was the same as for the tomographic imaging: t-tests between pre-stimulus baseline to late-stimulation intervals (-13 to -1s and 13 to 20s with respect to stimulus onset).

To further assess the influence of probe density on the separability between activation foci we additionally mimicked a sparser sampling DOT, using 15 instead of 30 probes and 225 optical data channels instead of 900. The image reconstruction for this sparse tomographic approach was the same as described in section 5.1.4.

5.1.7 Functional MRI Data Acquisition and Analysis

To provide a 'gold standard' of spatial resolution with regard to the hemodynamic response we acquired functional MRIs in the volunteers. The stimulation procedure was identical to the DOT experiment. FMRI data were acquired on a 3T MR scanner (TRIO, Siemens, Erlangen Germany) employing a T2*-weighted BOLD-sensitive echoplanar imaging (EPI) sequence (TR=2000ms, TE=18ms, 3mm isotropic fMRI voxel size) covering almost the entire brain. Immediately before functional imaging, an anatomical image volume was acquired (TR 1300ms TE 3.93ms, flip angle10∘, 1mm isotropic fMRI voxel size) for superposition of statistical t-maps. For each subject, we acquired 1200 fMR scans, resulting in a total duration of 54min.

SPM8 was used to perform analysis on imaging data. The initial ten images of each data set were discarded to account for T1 saturation effects. Preprocessing of functional images comprised realignment to the mean functional image and spatial smoothing (Gaussian kernel; FWHM= $6\times6\times6$mm). Voxel wise time courses were temporally high-pass-filtered (cutoff period 128s). Statistical t-maps were calculated by regression analysis based on the general linear model (Friston et al., 1995), defining regressor functions as the respective stimulus onset functions convolved with the canonical hemodynamic response function. According to the procedure applied to the DOT data, we set individual thresholds for all subjects and conditions in the fMRI experiment. The resulting t-maps for both conditions were superimposed on the 1.5T individual anatomical brain scans of each single subject, which were co-registered to the 3T anatomical brain scans. Data were masked within a hypothesis-driven region of interest (ROI) by selecting only clusters contra lateral to the stimulated hand. Thresholded t-maps of the two conditions

were then superimposed on the individual brain, which was extracted with the SPM8 segmentation tool.

5.2 Results

5.2.1 Ultrahigh-density DOT reveals distinct activations for 1st and 5th finger

In five (out of eight) subjects, we found two distinct separate activation foci for the two fingers using the ultrahigh-density DOT approach as shown in Figure 5.3. The volumes were reconstructed from the 900 optical data channels and are mapped onto the individuals' anatomies. In these five participants, the activations were found in the post-central gyrus, which is in line with the expected activation in response to the vibrotactile stimulation. However, the exact locations of the activations for the two fingers vary notably between individuals. Two subject (s4 and s6) showed the expected spatial orientation in the z-dimension with d1 activation inferior to d5 (s4) or with d1 activation anterior to d5 (s6).Three subjects (s2, s3 and s5) showed a pattern in which d1 stimulation elicited an activation superior to that during d5 stimulation. Although the individual functional-anatomical tomography varied, the distance between activations of the d1 and d5 was quite homogeneous (mean distance $d_{d1,\,d5}$ 13.7mm, standard deviation 5.6mm).

The remaining three participants (s1, s7 and s8) showed activation patterns for one of the two fingers only in the DOT measurements. It is worth noting that the same subjects did not reveal two activation foci during the fMRI experiment, either (data not shown).

Figure 5.3 shows all volumes in which remarkable changes were detected for both, d1 (magenta) and d5 (blue) stimulation. To reach distinct non-overlapping areas of activation for each finger the thresholds were adjusted individually. A fixed threshold across subjects blurred the contrast between fingers. This is unsurprising given the fact that absolute changes depend on many factors such as background optical properties which are known to vary largely between individuals and individual signal-to-noise ratio. The thresholding at a fixed percentage of the peak activation, however, yielded largely similar results as the arbitrary (hypothesis driven) threshold. We conclude that for identifying small activations, such as in our paradigm, it may be required to use hypothesis-driven thresholds.

5.2.2 Ultrahigh-density DOT is essential to identify small activations.

To illustrate the relevance of ultrahigh-density DOT, we mimicked the use of sparser probe arrays in our experiment by omitting channels from the data set and compared the reconstructed results.

The results in two subjects (s2 and s6) are illustrated in Figure 5.4. A sparse NIRS setup using a next neighbor approach with 12 channels (five sources and four detectors) is shown in the top row of Figure 5.4. The middle row illustrates the results which would be obtained using a moderately dense sensor placement for tomography (15 fibers with all potential combinations), yielding 225 optical channels. For s2 (middle column), the differences between a topographic nearest neighbor measurement (upper row) and ultrahigh-density DOT (lower row) are substantially different. The intermediate approach (middle row) reveals less focalized activations but shows the same general pattern as ultrahigh-density DOT. For s6 (right column), we can see a comparable orientation of the activation clusters with d1 anterior to d5 in all three setups, however the activation foci in response to the different fingers are separated only when the ultrahigh-density approach is used.

While individual results differed in the other subjects the general superiority of the ultrahigh-density approach with regard to a separation of the activation foci was present in all data sets.

5.2.3 Ultrahigh-density DOT shows good relative depth resolution but the activation volumes are projected to extra-cerebral layers.

One of the challenges in DOT is the correct depth localization because the underlying reconstruction methods favor solutions close to the tissue surface and therefore have a tendency to underestimate activation depth. This effect is particularly prominent in partial-view DOT imaging such as the back reflection geometry that is necessary in optical neuro imaging when no spatial constraints are applied. To illustrate the effect, Figure 5.5 shows the result from a simulation as described in chapter 4. In Figure 5.5 (a) we see the simulated target and (b) shows the reconstructed result without spatial constraints concerning the reconstruction space comparable to the discussed experiment.

Figure 5.6 (a) shows two activation clusters in a frontal view. The activation areas are clearly separated, with the d1 representation located somewhat deeper than that of the d5. This clearly demonstrates the ability of ultrahigh-density DOT to resolve cortical activation with good spatial resolution not only laterally, but also with remarkable relative depth discrimination.

While both activations are resolved in depth, the overlay with the anatomical structure demonstrates that the absolute depth placement is incorrect; both activation regions are projected to structural areas outside of the cortex. The reconstruction algorithm manages to locate the activations some distance below the outermost tissue layers but fails to achieve a more accurate placement within the brain matter. This is a well-known phenomenon which is caused mainly by the fact that the Jacobian derived from the forward model has the highest sensitivity values close to the surface and a significant decrease in deeper layers. As a result, any solution to the inverse problem that includes superficial optical changes is heavily favored over deeper-laying variations in optical dynamics.

There are several strategies to counter this effect (Niu et al., 2010b; Xu et al., 2007), each of which with particular advantages and disadvantages. The problem is to find objective criteria for manipulating W prior to the image reconstruction (Niu et al., 2010a) or to adjust the reconstructed images to the correct depth. The method by Xu et al. Xu et al. (2007) has not been tested on physiological data so far. In our study we used a physiology/anatomy driven approach to correct the depth localization of the reconstructed volumes. Instead of applying model-based correction schemes, which bear significant risk of image distortion in themselves, we affine-transformed the DOT result and this way forced it into the cortical layers (Figure 5.6 (b), (c).

Based on the knowledge that somatosensory finger representation is mainly found in superficial cortical areas, we determined the minimum distance that was needed to project the result volumes 'back' into the outermost cortical layer. Relating to the outer boundaries of the activation foci, it was consistently found that a translocation of about 15mm parallel to the head surface was needed to place the activation in cortical tissue. This was the least assumptive and invasive correction strategy and it led to a conservation of the size and relative orientation of the activation clusters to each other. No lateral distortions of the activation clusters were observed due to this affine transformation.

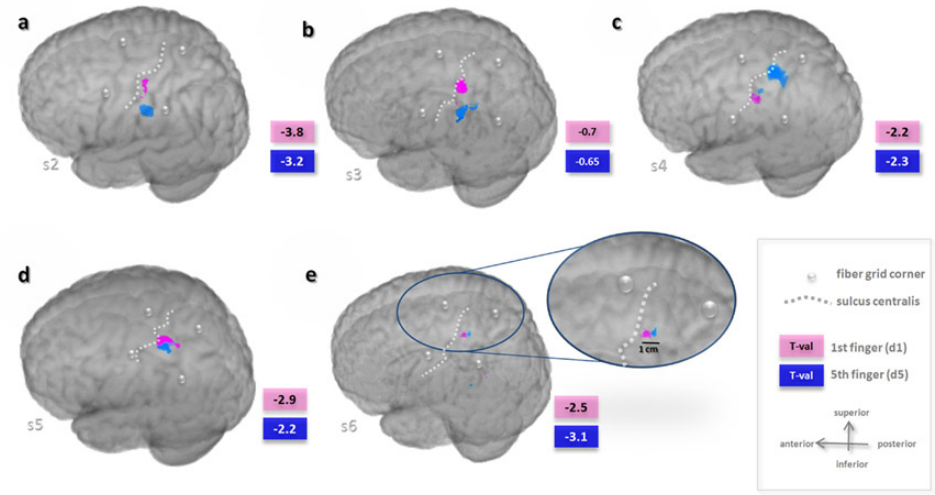

Figure 5.3: Results for vibrotactile stimulation of d1 (pink) and d5 (blue) of the right hand, mapped onto the individual brain anatomy of five subjects (s2-s6). Gray spheres indicate the corners of the grid.

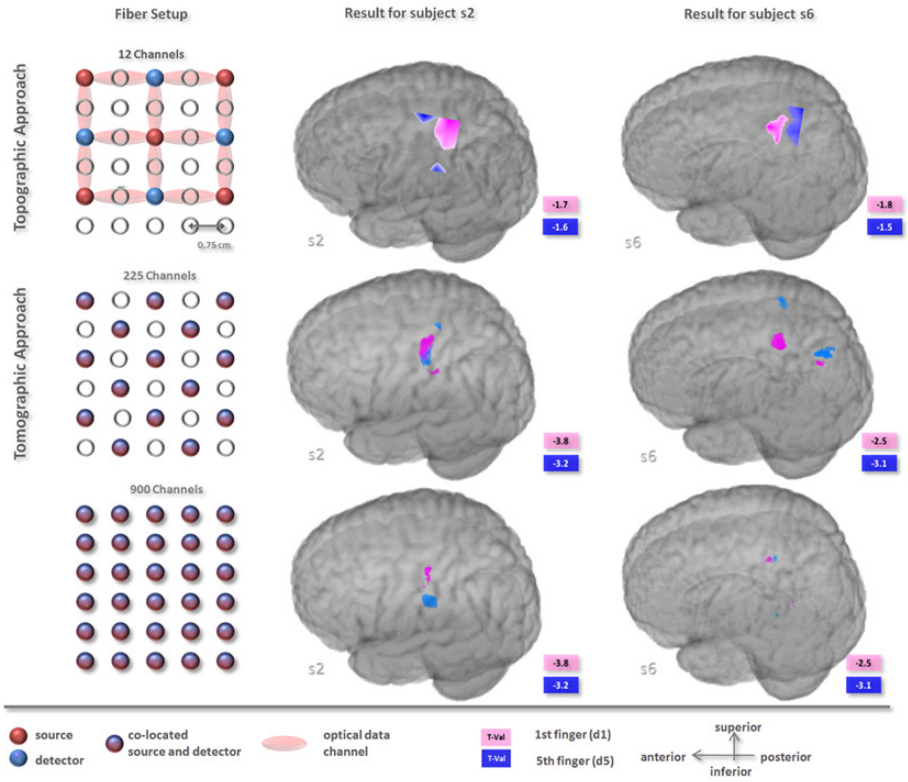

Figure 5.4: Comparison of activation patterns for vibrotactile stimulation of the d1 (pink) and d5 (blue) of the right hand for two subjects (s2, s6) when simulating three different densities of probes. Top row: Topography approach using 12 NIRS- channels (light red ellipses between light source (red dots) and detectors (blue dots). Middle row: DOT approach with a medium-dense grid of co-located sources and detectors (*bi*-colored dots, minimum SD distance 15mm) yields 225 optical data channels. Lower row: DOT approach with an ultrahigh-density grid and 900 channels. The increasing number of channels leads to a better lateral resolution and allows distinguishing between the two activations in both subjects (middle and right column).

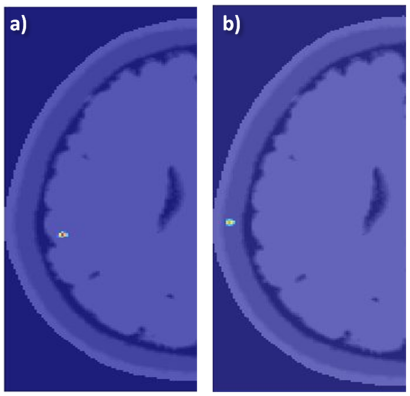

Figure 5.5: Challenge of correct depth localization. (*a*) DOT simulation of cerebral activation (*b*) reconstructed activation using tSVD and no spatial constraints in the forward model. The result was 'allowed' in all voxels.

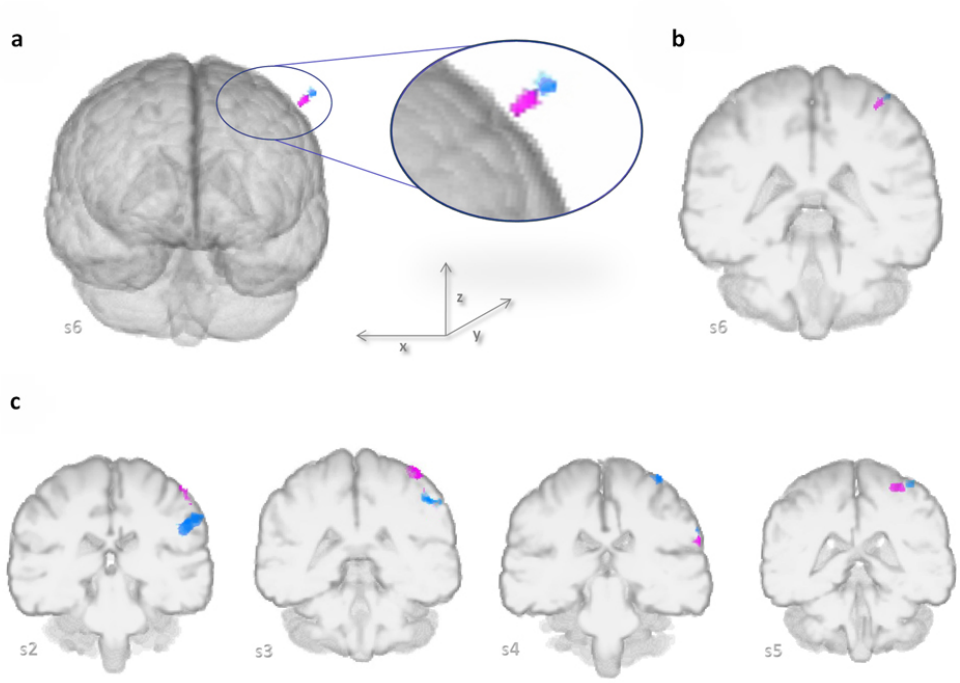

Figure 5.6: Reconstruction-based dislocation of the activation foci for d1 (pink) and d5 (blue) stimulation of the right hand in five subjects (s2-s6). (*a*) Frontal view reveals that activation clusters for both fingers was determined in different tissue depths but still there is insufficient depth localization. (*b*) Depth correction of the result volume localization: the volumes were translocated into the brain by 15mm parallel to the head surface in x and z direction. (*c*) Frontal view of a 10mm slice of the activated area for four subjects (s2-s5) after depth correction.

5.2.4 DOT and fMRI find comparable lateral positions in seven out of ten finger representations

Figure 5.7 illustrates the comparison between the results of DOT when compared to the corresponding fMRI measurements. Two clearly separate foci of activation for the d1 and d5 stimulation were seen-with both methods-in five of the eight subjects (s2-s6). The left column shows the reconstructed DOT results, and the right column contains the fMRI findings, all mapped onto the individual anatomies of the subjects.

We determined the coordinates of centers of activation for both fingers and imaging modalities by normalizing all anatomical scans and the DOT and fMRI volumes to a standard brain (Evans et al., 1993) using SPM 8. The Euclidean distances between DOT and fMRI activation were calculated for each condition and subject to obtain the lateral distance $d(DOT_{x,y}, fMRI_{x,y})$ and the distance in 3D space $d(DOT_{x,y,z}, fMRI_{x,y,z})$ (see Table 5.1). Regarding the absolute position of the activation foci we find six out of ten finger representations where the position error between DOT and fMRI result is less than 10mm in 3D space (lateral and depth difference) and in seven out of ten finger representations when taking only the lateral distance into account. When discussing these distances, one should keep in mind, that there is still some positioning error occurring from the previously described depth localization problem in DOT which not only affects the z-direction but also the x-direction.

From our view more interesting than the absolute position of the activation is the relative orientation of the foci: three out of the five subjects (s2-s4, top three rows) show substantially similar activation patterns in DOT and fMRI. Interestingly, while s4 displays the typically assumed functional organization that places d1 activation inferior to d5, s2 and s3 show the opposite behavior, and consistently do so in both DOT and fMRI. Reconstructing this 'switched' and rather unusual activation pattern with both methods give further indication that ultrahigh-density DOT and fMRI have a comparable access to cortical activation. In two other subjects (s5 and s6) the pattern was not identical, with a more posterior rather than inferior orientation of d5 (s5) and with a higher distance of both activations in s6 in fMRI and DOT. In these two cases, only the activation for d1 was similarly localized.

Subject	Finger	DOT			fMRI			3D distance $d(DOT_{x,y,z}, fMRI_{x,y,z})$ [mm]	lateral distance $d(DOT_{x,y}, fMRI_{x,y})$ [mm]
		x	y	z	x	y	z		
s2	*d1*	−50	−20	46	−56	−24	49	7.8	7.2
	d5	−56	−24	28	−55	−28	48	20.4	4.1
s3	*d1*	−40	−30	55	−56	−29	51	16.5	16.0
	d5	−51	−30	38	−59	−26	40	9.1	8.9
s4	*d1*	−64	−17	17	−66	−18	17	2.2	2.6
	d5	−62	−26	24	−59	−23	21	5.1	4.2
s5	*d1*	−31	−35	53	−49	−26	51	20.2	20.1
	d5	−40	−35	51	−42	−42	49	7.5	7.2
s6	*d1*	−38	−32	51	−50	−22	50	15.6	15.6
	d5	−41	−38	56	−48	−36	62	9.4	7.2

Table 5.1: Coordinates of the centers of activation for DOT and fMRI. Euclidean distances d between the activation foci of both methods were calculated for $d(\mathrm{DOT_{x,y}}, \mathrm{fMRI_{x,y}})$ and $d(\mathrm{DOT_{x,y,z}}, \mathrm{fMRI_{x,y,z}})$

.

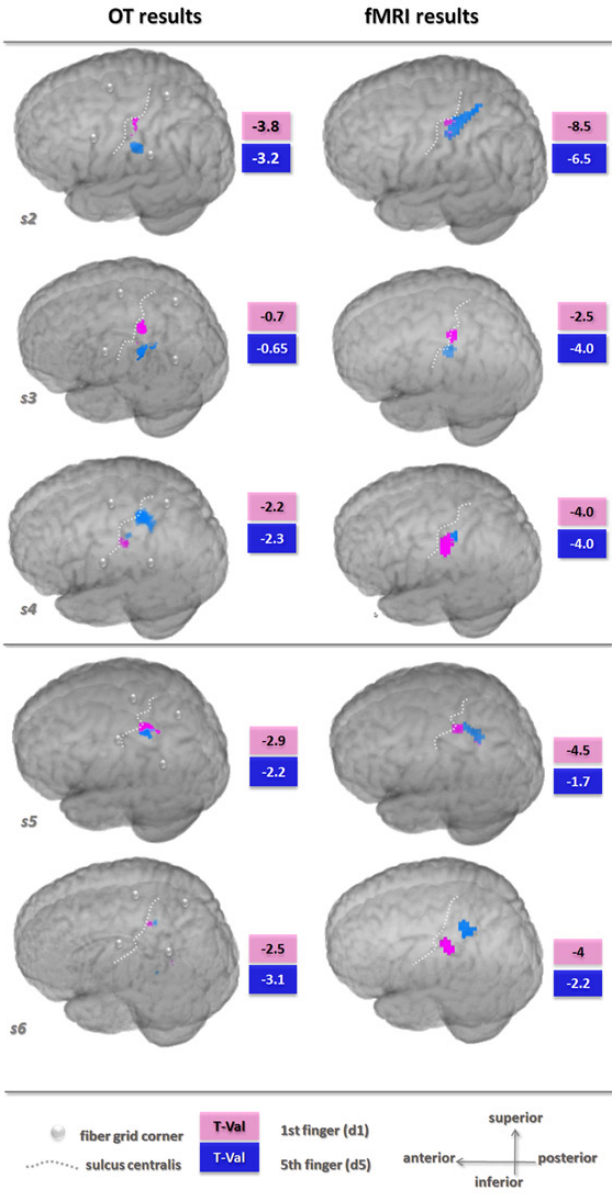

Figure 5.7: Comparison of NIRS and fMRI activation. All results were mapped onto the individual anatomy. Left column: reconstructed activation maps from DOT experiment for vibrotactile stimulation of d1 (pink) and d5 (blue) of the right hand for five subjects (s2-s6). Colored boxes indicate the cut-off t-values. Right column: results for the fMRI experiment.

5.3 Discussion

The aim of this multi-modal functional imaging study was two-fold. Firstly, we wanted to investigate whether ultrahigh-density DOT allows identifying distinct activation patterns for stimuli that are known to activate cortical areas of a small extend. Secondly, we examined the comparability of high density optical measurements with the gold-standard in functional brain imaging, fMRI.

For the optical measurement, we used an ultrahigh-density grid of optical fibers with an inter-optode distance of less than 10mm. We showed that a classic 12-channel topographic approach fails to resolve small activations and that a medium-dense grid can only partly reconstruct the expected results.

By attaching 30 optical fibers over an area of about 12 cm^2, we achieve a much denser spatial sampling compared to previous tomography approaches that use wider inter-optode distances (Custo et al., 2010; Dehghani et al., 2009; White and Culver, 2010a). We found that satisfactory results in terms of the location and separation of small functional activations such as present in the somatosensory system can only be achieved with DOT if the spatial sampling density approaches the scale on which feature resolution is desired, in our case, about 10mm.

The benefit of ultrahigh-density DOT is further substantiated by the similarities between the findings in HR-DOT and fMRI results. Seven of ten finger representations were detected in the same location. In three out of five subjects, showing two activation foci, we found a similar relative orientation of the activation maps, including two unusual switched patterns. For three remaining subjects, a stimulus answer could be detected neither with DOT nor in fMRI, which we take as further indication that both imaging modalities provide comparable access to small activations.

Even though the activation patterns showed strong qualitative similarities in both methods, we also observed consistent differences worth mentioning. For almost every subject, we received more than one result cluster below the chosen threshold for DOT, whereas in fMRI mostly one cluster for each stimulus was present. One possible explanation for this observation may be that methodological differences in the specifics of each of the modalities' analysis introduce this bias. Even though it is also possible that these additional clusters of activation in the DOT result could be false positive results, we deem this unlikely, given the fact that these areas appear in isolated places

and in the form of continuous patterns, rather than showing a distributed, grainy appearance throughout the entire volume, as one would expect from noise.

Even though we demonstrate the high functional sensitivity and good lateral resolution of ultrahigh-density DOT, there is significant potential in improving the depth profiling accuracy. Although we observe the remarkable capability of resolving different activation depths, the anatomical localization of those is still poor. The algorithm underestimates the activation depth and places the activation in superficial layers that correspond mostly to extracortical areas, such as the scalp and skull.

We have good reason to assume that the activation actually stems from the cortex. Recently we demonstrated that our imaging system using the same fiber configuration is able to access hemodynamics the cortex as shown in chapter 6. Furthermore, the observed signals show distinct focal areas instead of noisy patterns that correspond well with the known idiosyncrasy of hemodynamics connected with functional activation of the brain (Obrig and Villringer, 2003).

There are a number of methods to improve depth localization in DOT. Because this was not the scope of this specific study, we did not employ but would rather mention them. One way would be manipulating the Jacobian to restrain the result space to DOT-voxels that are located within cortical tissue. This is possible and has been shown to achieve good results in simulation studies where the head geometry -in contrast to this study- is known. Other less constraining algorithms look to correct the position error introduced in the reconstruction process. One proposed method (Niu et al., 2010b) adjusts the weight matrix by multiplying a matrix with an inversely arranged order of increasing values from outer to deeper layers, thus counterbalancing the loss of sensitivity in deeper layers. The problem with such correction methods is the identification of objective criteria to what extent and in which way to adjust the weight matrix.

One source of inaccuracy in the applied DOT method is the generic forward model geometry. The generation of individual forward models is time and energy consuming and not feasible when many subjects are investigated. It has been shown by (Custo et al., 2010) that using a generic head model can lead to an image reconstruction within the correct gyrus. The relative difference method, which we applied for image reconstruction (Pei et al., 2001) has been proven to be robust to inaccuracies of the initial guess and therefore allowed us to use a forward model with homogenous interior properties.

Nevertheless, differences in the skull geometry of subject and forward model and high variability of cortical structures can lead to distortions of results.

Despite the improvement in methods for DOT there seem to be difficulties that make the method yet unattractive to be widely used for functional studies in adults. Most studies deal with visual or motor tasks. Studies concerning the limitations of DOT application in human brains are not published so far. A relatively high noise level of the data compared to other imaging modalities may constrain extensive use of DOT.

One possibility to increase the signal-to-noise ratio and to extend the field of application could be the use extrinsic contrast agents instead of intrinsic agents like hemoglobin. A study applying an optical contrast agent in conjunction with DOT to increase the signal level and to obtain a clear separation of different tissue depths is discussed in the next chapter.

6 *In Vivo* Functional Brain Imaging: Detecting Extrinsic Agents in the Brain

Most *in vivo* studies of NIRS or DOT can be assigned to one of two fields: functional or (patho-)physiological. In the previous chapter, we showed the potential of functional DOT to resolve small and proximate activations. We also showed a good relative depth discrimination, even for low-contrast activations.

The next part of this thesis will examine the potential of DOT to detect physiological processes, more precisely, we evaluate if high-resolution DOT (in contrast to fNIRS) is able to separate cortical from non-cortical compartments and thereby detect changes in cortical blood supply. This could give rise for applications in a clinical setting.

For instance, bedside monitoring of brain perfusion or perfusion based therapies in neurointensive care patients is highly desirable. It may help to evaluate the patient's pathological state and to guide treatment. Existing imaging modalities such as X-ray computed tomography, MRI, or positron emission tomography (PET) are not always within a timely reach at the intensive care unit (ICU) and are not suited for constant monitoring of the brain. Furthermore, imaging facilities may be remote from the ICU and require undesirable intensive-care patient transport. Other established neurological monitoring techniques like intra-cranial pressure assessment, microdialysis and transcranial Doppler ultrasonography cannot monitor perfusion of the brain parenchyma.

Contrast enhanced DOT has the potential to close this gap and to serve as a quasi-continuous brain perfusion monitor. It is portable, noninvasive, and may be applied regularly (e.g. every 20-60min) without undue discomfort or

adverse health effects.

Previous fNIRS studies of brain perfusion using indocyanine green (ICG) focused on the measurement of cerebral blood flow (CBF) and cerebral blood volume (CBV) (Hopton et al., 1999; Keller et al., 2003) or differences of bolus kinetics in affected and unaffected hemispheres in stroke patients (Terborg et al., 2004, 2009). All these studies employed a topographic NIRS approach, which uses next-nearest neighbor measurements of optical fibers that are equally separated up to 5 cm. One major challenge of this approach is that the signal of the contrast agent in superficial layers like skin can dominate the measured absorption change. That's why methods are needed that are able to differentiate between tissue depths and that assess the contribution of the signal that originates from the brain: Studies using depth resolved NIRS, like time-domain (TD) (Liebert et al., 2006, 2004) and frequency-domain (FD) techniques (Kohl-Bareis et al., 2002) have shown the passage of an ICG bolus in the brain. Consistently, it was found that in healthy subjects the bolus was detected first in deeper (cerebral) layers and a few seconds later in the superficial (skin) layers. Figure 6.1 shows a schematic of the expected bolus behavior.

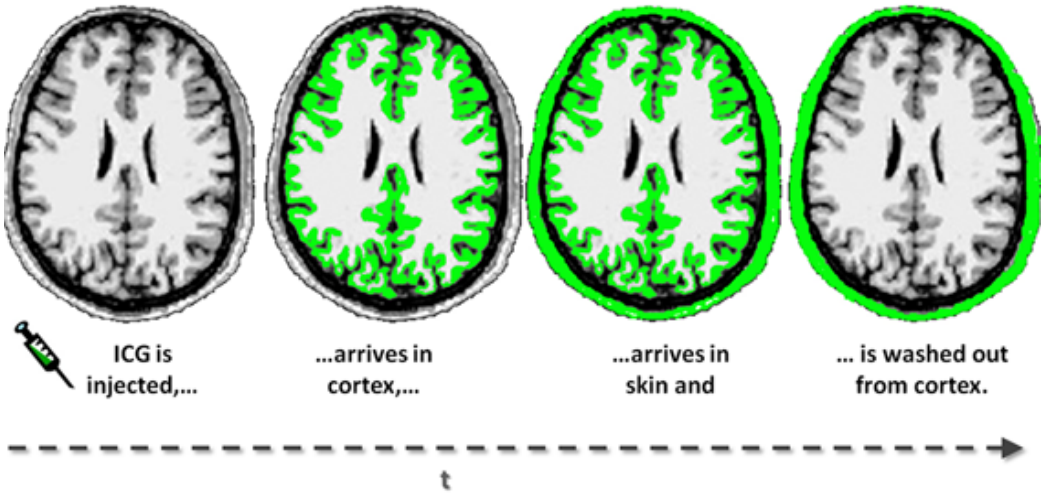

Figure 6.1: Schematic of the expected behavior of an injected optical contrast agent. Few seconds after injection, the bolus arrives in the cortex, followed by an arrival in the scalp and a fast washout from the brain. The tracer can be found in the skin many seconds later.

It can be expected that signals from intra-cerebral tissue decline faster than signals from superficial layers. This is in good agreement with the known high perfusion of brain tissue, and this phenomenon allows evaluating the separation of intra- and extra-cerebral fractions of the signal. While these FD and TD results are promising, we believe that the introduction into clinical use would benefit greatly from the application of continuous wave (cw) DOT, which is technically much less demanding and more economic compared to other approaches. In this study, we used the ultra-high density DOT system which is discussed in the previous section to detect absorption changes caused by an injected ICG bolus.

With this study, we are the first to demonstrate the bolus kinetics of an ICG injection using a cw HR-DOT system. We visualize the different bolus kinetics in the several compartments of the head, demonstrating the separation of intra-and extra-cerebral tissue, thus confirming the results that were obtained with more complex imaging devices. This is a contribution to the attempt of many research groups to develop a bedside-monitoring tool for brain perfusion. In contrast to other groups we do not aim for measuring absolute values of CBF or CBV which may not be necessary when the patient is repeatedly monitored. Major parts in this chapter are taken from the publication Habermehl et al. (2011): *'Contrast enhanced high-resolution diffuse optical tomography of the human brain using ICG'.*

6.1 Methods

We investigated three healthy, voluntary subjects (2 male, mean age 38 years). All subjects were collaborators of this study. We diluted 50mg indocyanine green (ICG-PULSION, PULSION Medical Systems, Germany) in 30ml *aqua ad injectabilia*. Different amounts of ICG were injected into the cubital vein of the right arm of each subject. Subject 1 received two boli (9mg ICG as the first bolus, 16mg as the second bolus) with a 10min delay. Subject 2 and 3 were administered one bolus of 12.5mg ICG each. ICG is a non-toxic fluorescent dye (Desmettre et al., 2000; Ebert et al., 2011) that binds tightly to serum proteins and has been frequently used in clinical routine. ICG absorbs light in the near infrared spectrum with an absorption and emission maximum at 805nm in plasma solution (Landsman et al., 1976). In experimental stroke models, it was shown that a disturbance of the blood-brain-barrier (BBB) together with an ICG injection and the exposure

to near-infrared light does not lead to photo-toxicity (Keller et al., 2002). This is important since stroke patients often suffer from a disruption of the BBB.

We measured absorption changes with the DYNOT tomography imager (NIRx Medizintechnik GmbH, Berlin, Germany), which applies light of two wavelengths (λ_1=760nm and λ_2=830nm) to the subject's head. Thirty co-located optical fibers (serving as source and detector) were placed over C4 in a 5×6 optical fiber grid covering $\sim$12cm^2 of the right hemisphere (inter-optode separation: 7.5mm) (Fig 6.2) thereby achieving 900 overlapping optical data channels. To fixate the optical fibers on the head surface and to ensure stable optical contact, we used an open scaffolding structure and individually spring-loaded fibers. This design allows easy access of the fiber tips for parting of the hair before placing an optode. We obtained images of hemodynamic changes using the normalized difference method (Pei et al., 2001) with an image reconstruction using tSVD (see section 3.4.4 on page 23) using all singular values that explain 98% of the data.

The Jacobian was determined using BrainModeler (NIRx Medical Technology, LLC, NY) which provides a library of subvolumes from a MRI-scan based finite element (FE) mesh with precalculated inverse parameters for all possible source and detector combinations on the subvolume's boundary. Each of these subvolumes contains precalculated forward solutions of the photon diffusion equation and reference detector values. These forward solutions are computed based on the simplified assumption of homogenous interior optical properties ($\mu_a = 0.06\text{cm}^{-1}$,$\mu_s = 10\text{cm}^{-1}$). We used the same FE mesh for image reconstruction for all three subjects. This mesh contains 3332 nodes with a resolution of $\sim$4mm and has the dimension of $72 \times 68 \times 52$mm ($height \times width \times depth$).

All data were low-pass filtered to reduce high-frequency noise before further processing ($f_{cut\,off}$=0.3Hz). We reconstructed the time courses of relative absorption changes for every node of the finite element mesh using tSVD, which resulted in an array of 3332 time courses. For visualizing the bolus kinetics in different compartments of the volume, we determined the time (in s after bolus injection) of the ICG arrival for each node (defined as the time point when 50% of the maximum value was reached). In combination with the spatial coordinates of each node we finally converted the result in a 3D volume. Results were comparable in all three subjects. Interestingly, no quantitative differences were observed due to different amounts of injected ICG. Therefore we will report detailed results for one subject only.

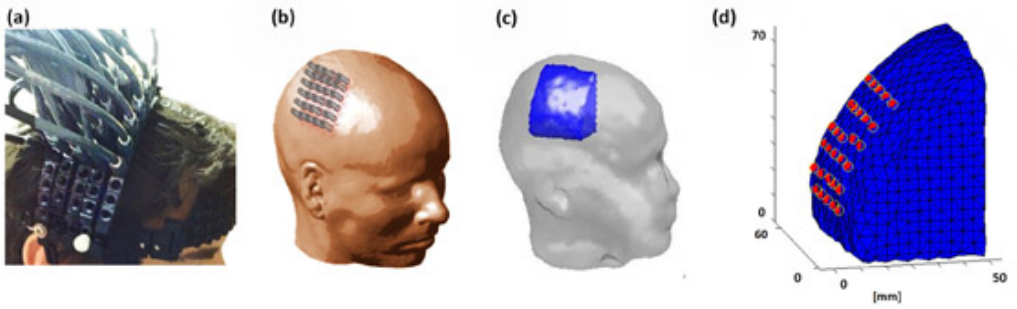

Figure 6.2: Imaging setup. (*a*) Absorption changes were measured with a DOT imaging system (DYNOT, NIRx Medizintechnik GmbH, Berlin, Germany) (*b*) A 5×6 fiber grid with 30 co-located sources and detectors was placed pericentrally over the right hemisphere. (*c*) Subvolume, which was selected for forward modeling.(*d*) Finite element mesh that was used for image reconstruction of relative absorption changes.

6.2 Results

6.2.1 An earlier increase in absorption can be observed for larger optode distances

Three-dimensional DOT uses multi-distance measurements of different SD combinations. Light that is detected far away from the source is assumed to have passed deeper tissue layers than light that is detected close to the source. Signals measured with 3rd nearest neighbor (NN) combinations ($\sim$22.5mm SD distance) can be assumed to have significant components originating from brain tissue, while signals from 1st NN ($\sim$7.5mm SD distance) channels contain mainly information of skin and skull tissue.

A few seconds after injection, the passing of the bolus is clearly indicated in the raw signals by a transient decrease (indicating a higher absorption of the light). When examining the raw detector readings (not shown), we find an averaged decrease in the measured intensity of 8% for 1st NN and 12% for 3rd NN combinations (standard deviation of a 45s pre-bolus baseline: 0.5% for 1st NN and 0.8% for 3rd NN).

To compare the different bolus kinetics directly, Figure 6.3 shows normalized detector readings from 1st NN and 3rd NN measurements (data from subject 1, 1st bolus and $\lambda = 760nm$). The averaged 1st NN response (red) shows a clear delay in the bolus-related signal decrease, compared to the mean 3rd NN signal (blue). This is explained because the larger optode separations have a significant signal contribution from deep tissue (i.e., cortex), which due to better perfusion is reached first by the bolus compared to skin. Short SD separations, in contrast, are much less sensitive to deep tissue and are mainly influenced by superficial activity, such as skin perfusion, which is known to be delayed with respect to the brain. This clearly demonstrates the sensitivity of the different SD distances to different tissue depths, even in the raw (non-reconstructed) signals.

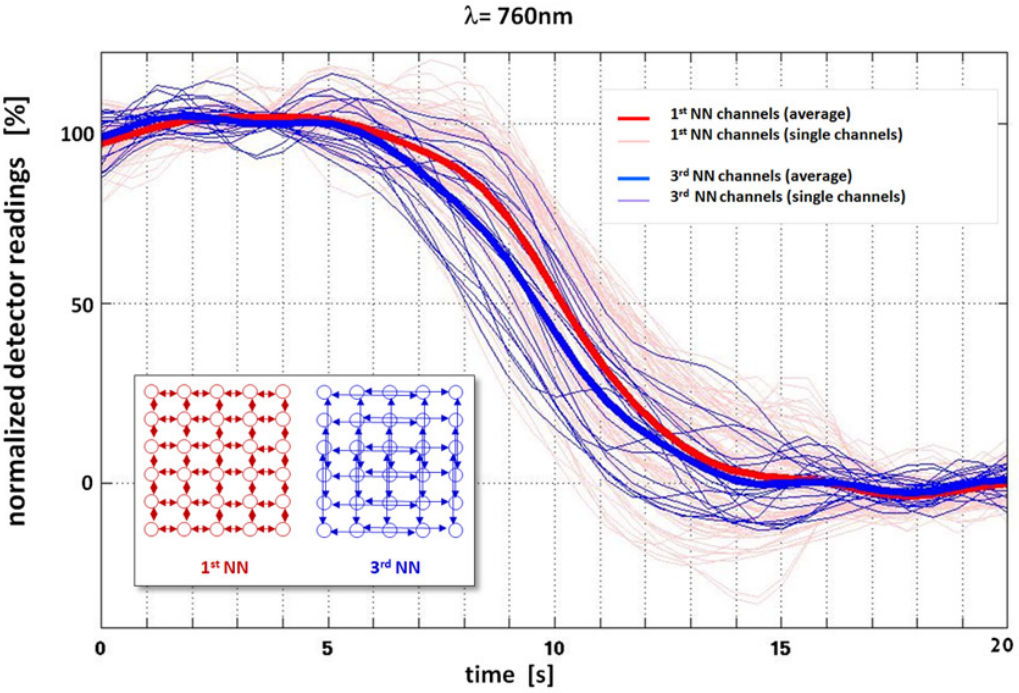

Figure 6.3: Normalized detector readings following an ICG bolus (subject 1, $\lambda = 760$nm). Thin red lines indicate the time course of all 1^{st} NN combinations (SD distance 7.5mm). Thin blue lines represent the time course for all 3^{rd} NN combinations (SD distance 22.5mm). The average 1^{st} NN and 3^{rd} NN time courses are depicted by the bold lines. The insert box in the left corner depicts the fiber grid set-up and the channels taken for the different time courses.

6.2.2 Reconstruction in DOT allows the separation of extra- and intracerebral tissue

To be able to locate the bolus dynamics in a volumetric view, we reconstructed a three-dimensional time series of absorption changes within the sampled tissue, using the forward geometry and definition of the optical fiber arrangement shown in Figure 6.2 (c).

Figure 6.4 (a) depicts a frontal view on the reconstructed result volume, visualizing the early arrival of ICG in deeper voxels at t=5s and the arrival of the dye in superficial layers approximately at $t = 7$s. Figure 6.4 (b) shows the arrival time of the bolus in each voxel by color-coding the time at which 50% of the maximum absorption value is reached. In both figures we find a clear border at a depth of 10-12mm, beneath which the early response is seen. This indicates the location of the cortical surface that runs about 10-14mm blow the head surface (see, Figure 6.4 (c).

Figure 6.5 shows the averaged reconstructed time courses from two regions of interest (ROI) of different tissue depth for subject 1. One ROI is located in the superficial (skin) layer (red), and the other one in the brain region (blue). Since the image reconstruction procedure calculates relative changes of absorption, the baseline prior to the bolus fluctuates around zero. The measured relative increase of absorption due to the bolus injection ranged from 1.0×10^{-5} to 2.6×10^{-5}mol/l for deep voxels and from 1.3×10^{-5} to 2.4×10^{-5}mol/l for superficial voxels. To allow for a direct comparison of the different bolus kinetics, we normalized each time course.

In both boli of subject 1 and for each wavelength we find a systematic earlier increase of absorption in deeper voxels and delayed (1.5-4s) increase of absorption within the superficial layer. We also observe a fast decline in the time courses of the deeper voxels. This observation is in line with contrast enhanced perfusion-weighted MRI and has also been observed using frequency and time domain systems (Kohl-Bareis et al., 2002; Liebert et al., 2006).

Figure 6.6 presents the results for subject 2 and subject 3, demonstrating the robustness of the method. Similar to the results of subject 1 we can clearly separate deeper voxels with an early arrival of the absorber and superficial voxels with a later increase of absorption. Due to the somewhat slower injection of the bolus we find a more broadened answer in the deeper voxels than in subject 1. We determined the characteristic shape in the time courses of the in- and out-flow of the contrast agent in extra-and intracerebral

tissue in all three subjects, demonstrating that three-dimensional perfusion imaging of the brain is possible using cw HR-DOT.

To show the improved resolution of the method, Figure 6.7 presents a secondary result. When viewing the HR-DOT images for subject 1 in an angle perpendicular to the head surface, we consistently observe a distinct pattern of the arriving absorber in the most superficial layer. The bolus dynamics in the outermost layer (10mm thickness) displays the arrival of the ICG at t=7s, spreading from anterior/inferior to posterior/superior. These results were confirmed for every bolus injection and wavelength (data only shown for 1^{st} bolus and $\lambda = 760$nm). This is further indication of the excellent lateral and depth resolution of the used imaging system and reconstruction procedure.

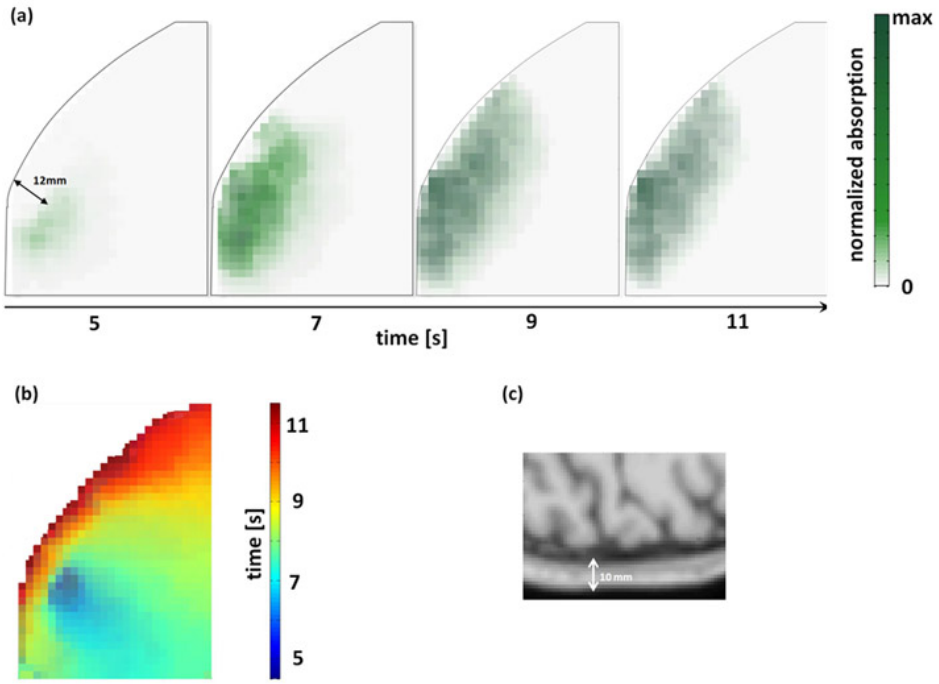

Figure 6.4: (*a*) Single frames from a video can be accessed via Optics Express, depicting a cross-section of the reconstructed result volume (subject 1, 1st ICG bolus and $\lambda = 760$nm). Green voxels indicate increased absorption. Voxels are colored semi-transparent, bolus injection was at $t = 0 - 1$s. (*b*) Same view on the reconstructed result volume as in (a), displaying for each voxel the time (in s after bolus injection) when 50% of the maximum absorption value was reached. (*c*) Transversal slice from an anatomical scan of the used forward model geometry.

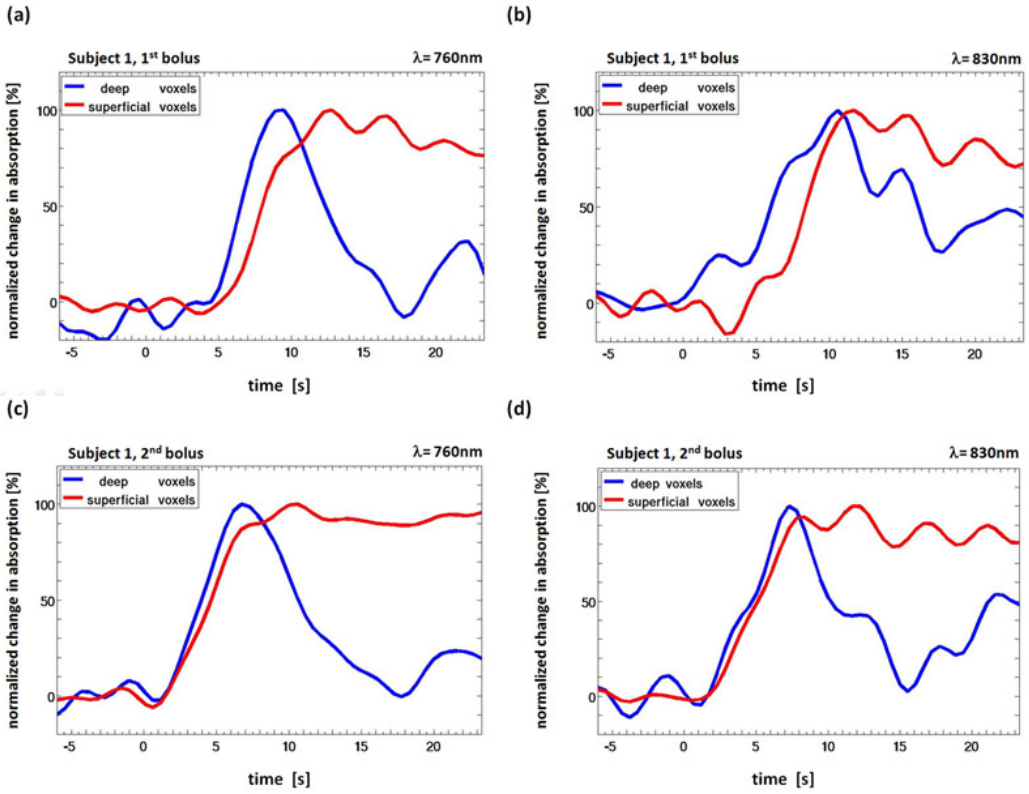

Figure 6.5: Time courses of normalized relative absorption changes for subject 1 and both boli and wavelengths. Red lines represent the averaged intensity values from superficial voxels; blue lines represent intensity values from voxels from deeper (cortical) layers. Injection of the ICG bolus was at t=0-1s. Note, that due to manual injection, this time point is only an approximation. (*a*) 1st ICG bolus, $\lambda = 760$nm. (*b*) 1st bolus, $\lambda = 830$nm. (*c*) 2nd bolus, $\lambda = 760$nm. (*d*) 2nd bolus, $\lambda = 830$nm.

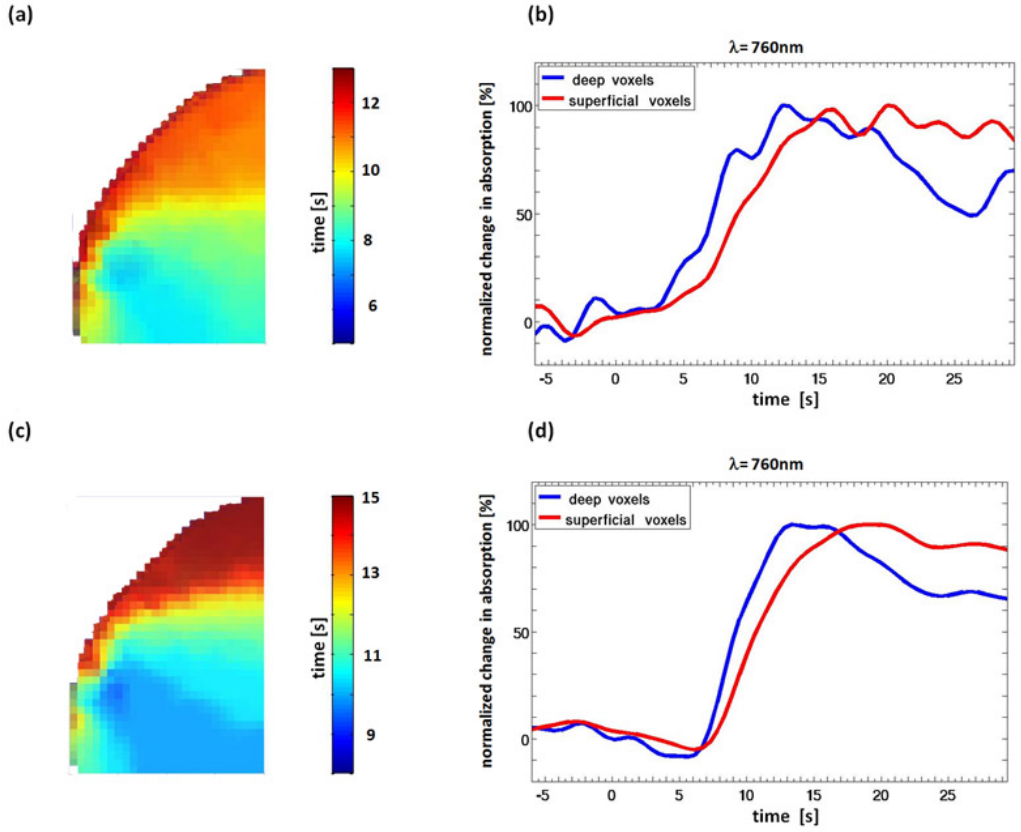

Figure 6.6: Subject 2. (*a*) Frontal view on the reconstruction volume, color-coded voxels depict the time (in s after bolus injection (t=0-3s)) when 50% of the maximum absorption value was reached. (*b*) Subject 2, reconstructed time courses for deep and superficial voxels for $\lambda = 760$nm. (*c*), (*d*) Same as (a) and (b) but for subject 3.

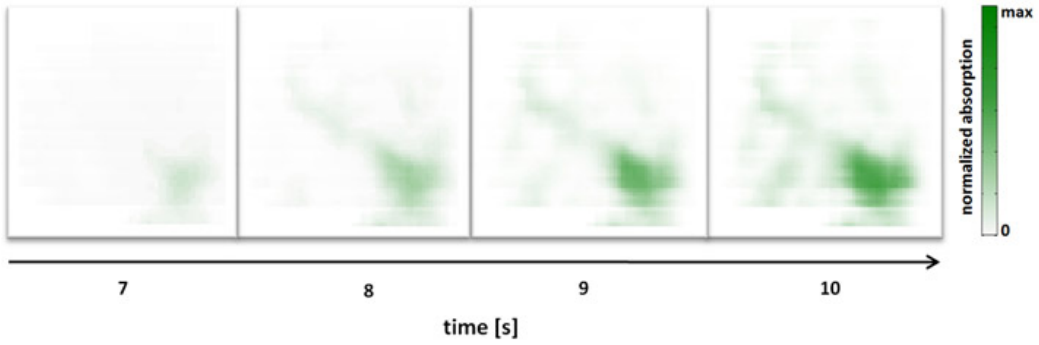

Figure 6.7: Single frames from a video accessible via Optics Express of a lateral view on a 10mm thick slice (60×60mm wide) of superficial layers for subject 1, the 1st ICG bolus and $\lambda = 760$nm. Green voxels indicate increased absorption.

6.2.3 Ultra-high density or high density DOT are mandatory to separate cortical from non-cortical layers

The first column of Figure 6.8 shows the reconstructed results obtained on a single subject, considering all 900 data channels. The first row illustrates the FE mesh with the defined position of the 30 co-located sources and detectors on the boundary. The second and third row depict the time of arrival of the bolus in each voxel, seen from different angles. We clearly observe an early increase in absorption in deeper layers (∼12mm depth) and a later increase in superficial layers. This is confirmed when defining two separate regions of interest for skin and brain and averaging all time courses within each of these (last row). As expected, the absorption dynamic in the brain region shows an early increase, followed by rapid decay. In contrast, we find a delayed increase and a slower decline in superficial voxels.

The center column of Figure 6.8 shows reconstructed results from the same experiment; however, here we only considered data from those 225 optical channels that one would obtain using a dense grid of 30 optodes, of which 15 are sources and 15 are detectors (i.e., no collocated positions). Even though the spatial resolution decreases to some extent, this setup would be sufficient to separate both layers and reconstruct the different bolus kinetics in the two ROI.

The right column presents the reconstructed result volume with data from 9 optical data channels. This corresponds to a topographical NIRS setup which contains only neighboring optodes and does not afford any overlapping measurement channels. The so reduced setup is not capable of distinguishing between different layers, and the spatial resolution is greatly diminished. The location of regions with specific arrival times is greatly distorted in comparison to the cases shown in the left and center columns. The time varying absorption from ROI in the skin and brain layer shows no clear separation in flooding or washout dynamics.

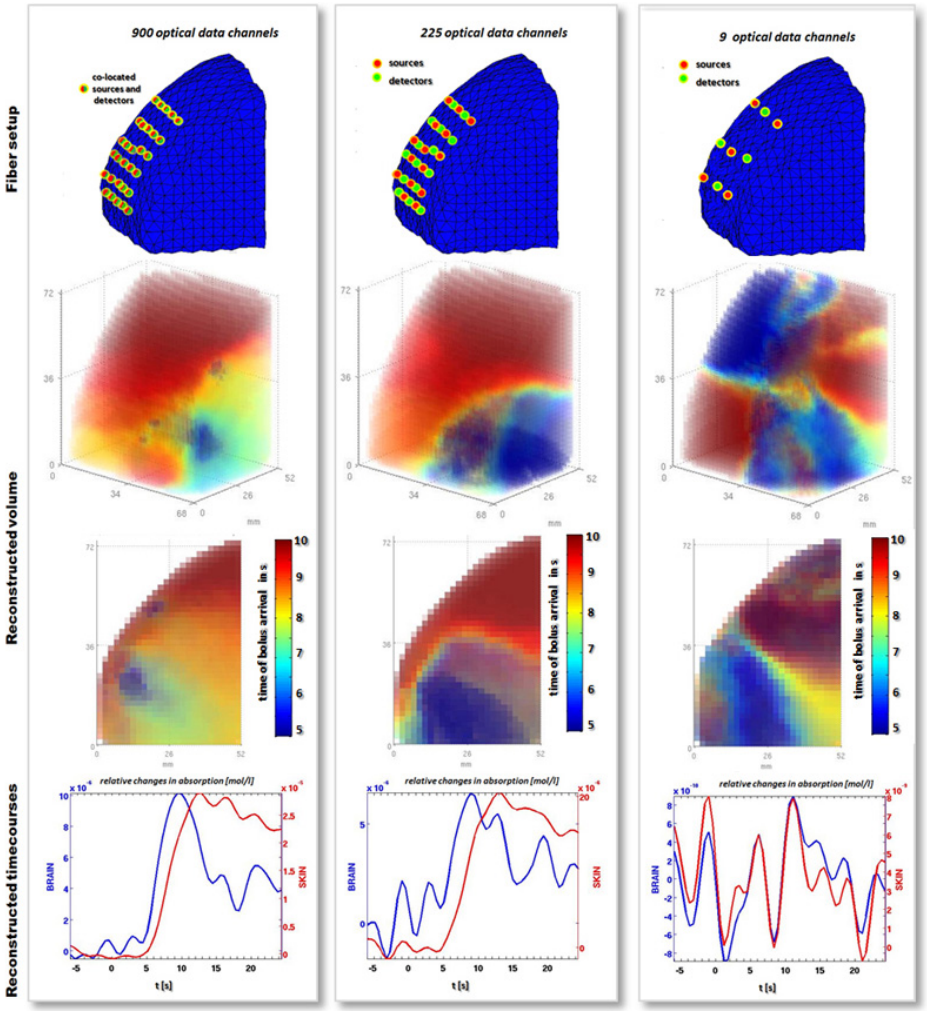

Figure 6.8: Results for one subject. The first row shows the fiber location on the FE-mesh, the second and third rows present the reconstructed volume with the voxels color-coded with the time of arrival of ICG (defined as the time in s after injection when 50% of the maximum value was reached).The bottom row shows the reconstructed time courses of brain and skin region. Left column: Results using data from all 900 optical data channels (including zero-distance measurements). Center column: Results considering a subset of data corresponding to a fiber-setup using separate sources and detectors. Right column: Results considering only fibers at topographic distances.

6.3 Discussion

Monitoring of cerebral perfusion in neurointensive care is highly desirable and as of yet is only partially realized owing to the scarcity of neuro-ICU equipped with dedicated imaging equipment on one hand, and the limited monitoring capability of existing equipment on the other. A tool that enables the regular monitoring at short intervals at the bedside using a safe dye would be helpful, also because many patients cannot easily be transported. Unlike topographic NIRS, we demonstrate that the continuous wave high resolution DOT has sufficient depth and lateral resolution to be used for cerebral perfusion monitoring. It furthermore overcomes the technical challenges of more demanding frequency or time domain NIRS approaches.

In this study, we investigated the feasibility of separating intra- and extracerebral tissue by using a cw HR-DOT imaging system which is normally used to determine concentration changes of HbO_2 and HbR (Habermehl et al., 2012; Koch et al., 2010; Schmitz et al., 2000) due to brain activation. We were able to reproduce previous results (Kohl-Bareis et al., 2002; Liebert et al., 2006) with a less demanding system in all three subjects. Three-dimensional result volumes of absorption changes were reconstructed within a few seconds due to the use of pre-calculated forward solutions. The images show a high lateral and good depth resolution and allow the separation of intra- and extra-cerebral tissue.

The used wavelengths are close to the maximal absorption spectrum of ICG in plasma. We are aware of the fact that there are three chromophores that mainly contribute to the measured signal, but the impact of changes in HbO_2 and HbR concentration (which can be seen in fluctuations of the baseline) is relatively small and stable over time compared to the high amplitude changes in light attenuation caused by the ICG. For example, referring the measurement with $\lambda = 760$nm (subject 1, bolus 1, intracerebral ROI) we found an almost 10-fold increased amplitude of the ICG response ($1.1 * 10^{-5}$mol/l) compared to the standard deviation of a 45s pre-bolus baseline ($1.2 * 10^{-6}$mol/l). For $\lambda = 830nm$ (same measurement) we found a more than 20-fold increase.

Nevertheless, hemodynamics can be observed in the signal; especially within the 830nm time courses, to which HbO_2 is the predominantly contributing hemoglobin species, we see oscillations that are part of systemic signals (Kirilina et al., 2012; Obrig et al., 2000). For further studies, we

consider the implementation of a third wavelength, allowing for a better separation of the signals. However, the typical bolus kinetics with different bolus arrival times within the different compartments and the fast decline of the signal within cerebral tissue and can clearly be seen using a single wavelength. The distinct border of the early arrived bolus at 12mm tissue depth indicates the cerebral boundary.

In this study we succeeded in the attempt of showing the separation of intra- and extra cerebral tissue by using a cw HR-DOT imaging system in combination with the injection of a safe dye. In our results, we see the early arrival of the ICG for larger SD-separations in the raw data and the expected bolus kinetics in different layers of the reconstructed volume. This work can help to promote the use of DOT for monitoring patients undergoing brain trauma or stroke. It could be highly useful to detect changes in brain perfusion in time without expensive measurements and difficult transport of the patient. We highly recommend further studies using a more complex system that takes changes of all important chromophores into account.

Additional to the detection of extrinsic contrast agents, we will investigate the possibility of using intrinsic markers that are related to cerebral perfusion. The reconstruction of the spatial distribution of low frequency oscillations in brain and skin will be discussed in the next chapter.

7 *In Vivo* Functional Brain Imaging: Intrinsic Cortical Signals

A strong signal that occurs in many NIRS measurements are spontaneous hemodynamic oscillations in the 0.1Hz band, so-called low frequency oscillations (LFO). They could serve as an additional marker for local brain perfusion. Together with heart beat (HB) signals (around 0.9-1.2Hz) they are found in almost all NIRS and DOT measurements. Figure 7.2 shows an example of one measurement channel of a DOT resting state measurement using 830nm. LFO that occur every ten seconds (Figure 7.2 (a) and the cardiac signal (b)) can be clearly observed.

Even though the driving mechanism for LFO remain unclear, they are connected to blood pressure, cerebral blood flow and autoregulation (Sassaroli et al., 2012; Schytz et al., 2012; Tong and Frederick, 2010). Various fNIRS studies have been performed to evaluate LFO in the context of different diseases (Phillip et al., 2013; Schytz et al., 2013) or resting state connectivity (Nakao et al., 2013; Medvedev, 2013; Mesquita et al., 2010). Since all studies used topographical NIRS, one main question remains unresolved: do the measured signals origin from the brain or the skin? To visualize the problem of superficial blood vessels interfering with cortical signals, Figure 7.1 shows an anatomical specimen of superficial arteries in the human head.

In section 6, we described the discrimination of different layers of the head by tracking a bolus of an *extrinsic* contrast agent. Based on these promising results, we aimed at achieving the same by relying on *intrinsic* slow oscillations. Therefore, we demonstrate that DOT with its 3D image reconstruction allows a depth profiling of hemodynamic rhythms in the adult head.

Figure 7.1: Preparation of superficial arteries of the head with red wax from Friedrich Schlemm, 1830 (Anatomische Sammlung am Centrum für Anatomie der Charité Berlin).

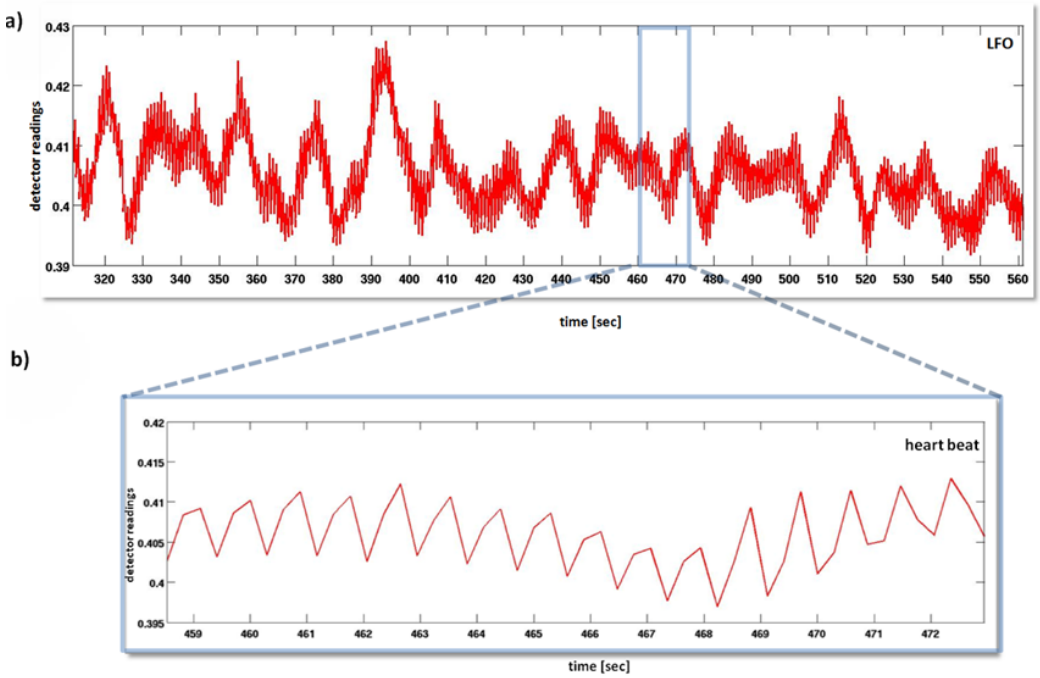

Figure 7.2: Example of detector readings from a DOT measurement (resting state) from a wavelength of 830nm which is dominated by changes in the concentration of HbO_2. Low frequency oscillations (0.1Hz) and heart beat signals can be clearly seen and dominate the resting measurement.

7.1 Methods

For the measurement, we used the same imaging system and set-up described in section 4.1.3 on page 31 (NIRScoutX (NIRx Medizintechnik, Germany) with 32 sources* 32 detectors, 760nm & 850nm). We placed two grids of optical fibers bilateral, peri-centrally over C3 and C4 (each side: 16 sources *16 detectors) achieving 2*256 data channels with a minimum source-detector separation of 13mm and a 3.91 Hz sampling frequency. Eight subjects (2 female, 6 male, mean age 33.8 $\pm$ 6.7 years) performed a 10min resting task in a sitting position.

Image reconstruction was performed for both hemispheres independently. For forward modeling and image reconstruction we used the methods described in sections 6.1. A schematic of the fiber setup and forward model can be found in Figure 7.3.

To investigate localization of the power of LFO and HB, the reconstructed time series were linearly detrended and normalized by their respective mean value to discard the DC part in the spectrum. We calculated the power spectral density (PSD) for each reconstructed HbO_2 time course in every node of the finite element mesh. These power spectra were normalized by their respective integral to give all nodes (especially the deeper ones) the same impact. For visualization purpose, the normalized power at 0.1Hz (and subject-specific heart beat rate, respectively) was interpolated into one volume. To generate one final result, volumes of all subject were averaged and a central slice of the reconstruction volume was superimposed onto the brain atlas.

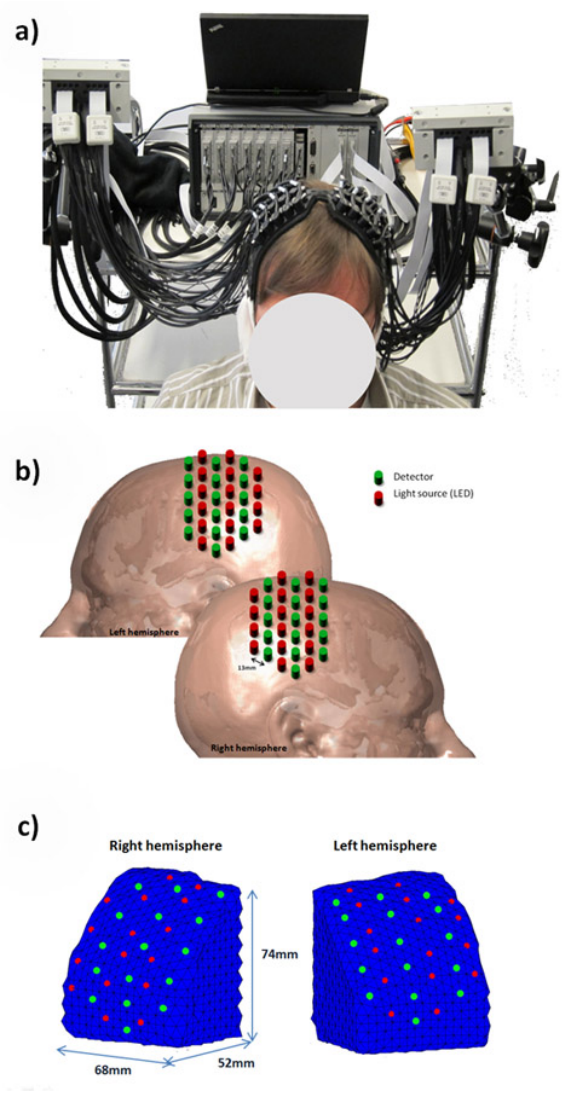

Figure 7.3: (*a*) Imaging device (NIRScoutX), (*b*) Schematic of the fiber setup, (*c*) Discretization for the forward model. This setup achieved 256 optical data channels over each hemisphere with a minimum inter-optode distance of 13mm.

7.2 Results

In the following, we analyze the distribution of specific oscillations; first we investigate the distribution of typical hemodynamic signals in the raw data concerning wavelength of the used light and differences within different source-detector separations. Finally, we investigate their spatial distribution within reconstructed volumes.

7.2.1 Raw Data of both wavelengths are contaminated with hemodynamic oscillations.

Figure 7.4 shows the power spectrum for normalized, unfiltered raw data from a resting measurement. For all measurement channels with a short (13mm) and with a large (35mm) inter-optode distance, the power spectral density was calculated and averaged. This was done for both wavelengths (red: 830nm, blue: 760nm). This corresponds to a topographic NIRS setup. We find in all wavelengths and both fiber distances low frequency oscillations of $\leq$0.1Hz and heart beat signals; relying on a topographical data analysis does not allow to ascertain their origin within the volume. Consequently, the analysis of the spatial distribution was based on the reconstructed volumes.

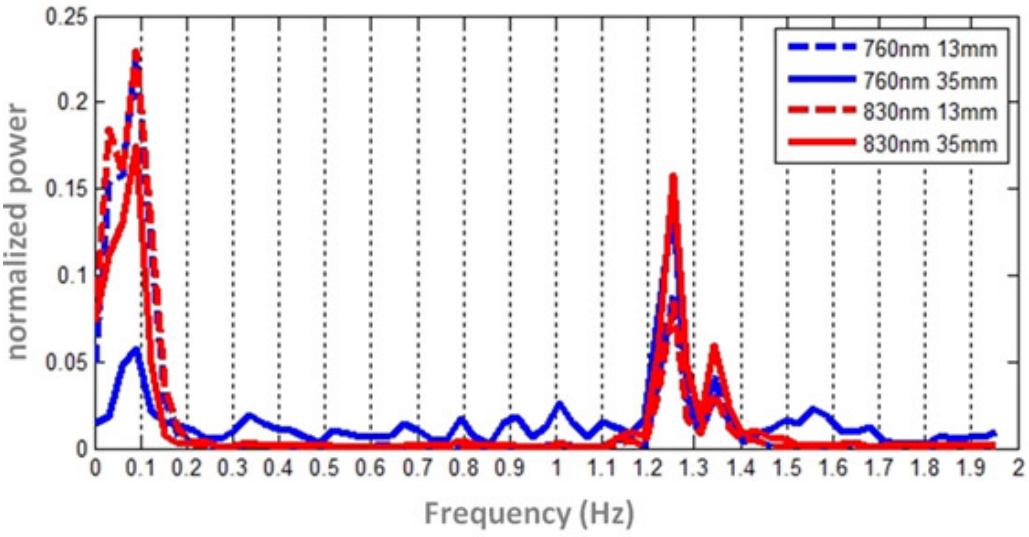

Figure 7.4: Power spectral density for all averaged 1st and 3rd nearest neighbors (13mm and 35mm, respectively) and both measured wavelenghts.

7.2.2 Oscillations are stronger in HbO_2 time courses.

In the following, we concentrate on the reconstructed time courses for absorption changes of HbO_2 and HbR in each volume element. In functional brain imaging as described in chapter 5 the HbR signal is more reliable since it is less contaminated with global or superficial signals. However, in this study we are particularly interested in these global signals. As a first analysis, we compared the absolute power values for all reconstructed nodes in all subjects. Not suprisingly, we found that the hemodynamic signals are more prominent in HbO_2 time courses. Figure 7.5 shows the average of the normalized power spectral density of all reconstructed time courses for HbO_2 and HbR for one subject. When looking in all subjects, the power in HbO_2 was 1.8times higher ($\pm$0.65) for the 0.1Hz oscillations and 2.1 times higher ($\pm$0.73)for the heart beat signal. Hence, we concentrate in the following on results based on this chromophore.

7.2.3 LFO are mainly found in deep and superficial layers, whereas heart beat is seen in the skin.

Based on the frequency analysis of reconstructed time courses of HbO_2 absorption changes, we find a specific pattern which can be observed in almost all subjects.

We find that a high fraction of the signal variation that can be explained by LFO origins from deeper layers but they can also be seen in the skin voxels. When when looking at regions of interest (brain and skin), we find an equal distribution of the power for LFO. The ratio $\text{power}_{\text{skin}}/\text{power}_{\text{brain}}$ is 0.94 ± 0.4 for the left hemisphere and 1.00 ± 0.3 for the right hemisphere (grand average for all subjects).

On the other side, time courses that have a high power for heart beat signals are mainly found in superficial voxels. In seven out of eight subjects we find a higher power in the skin region (ratio $\text{power}_{\text{skin}}/\text{power}_{\text{brain}}$: 1.94$\pm$1.2 for the left side and 1.41 ± 0.4 for the right side).

Figure 7.6 shows the average power for LFO and heart beat for all eight subject, both hemispheres and the two regions of interest. Please note, that these averaged values can only give a first impression about the spatial distribution, since there is a high localization of regions with high power.

For a more intuitive visualization, Figure 7.7 shows this distribution of the power values as a grand average of all subjects in a volumetric view.

One middle cross section of the reconstruction volumes for each hemisphere is mapped onto the brain atlas (see (a) for LFO and (b) for heart beat signal). Since there are subject-specific differences due to variations in anatomy, position of the fiber pad and signal-to-noise level of the measurement, cross-sections of all individual subjects are shown in figure 7.8.

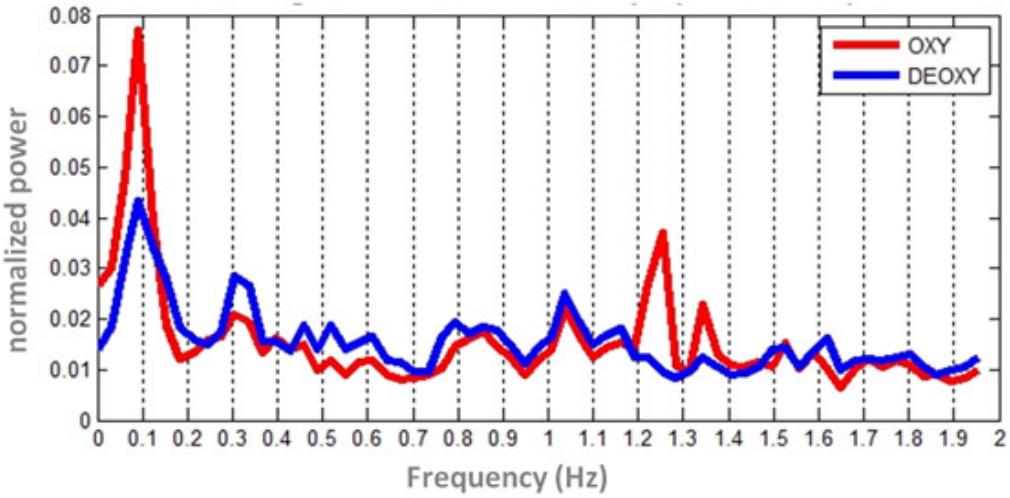

Figure 7.5: Averaged Power Spectrum for all reconstructed HbO_2 and HbR timecourses for one subject.

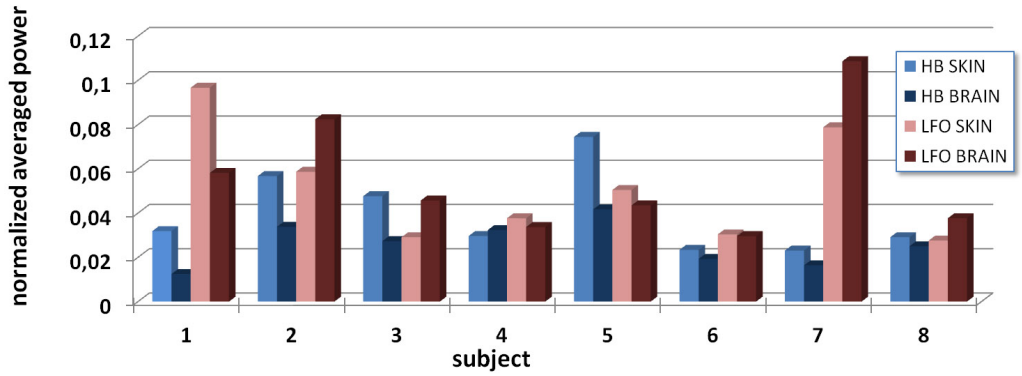

Figure 7.6: Averaged power for the frequency band of 0.1Hz (LFO) and heart beat rate for eight subjects and two regions of interest (brain and skin).

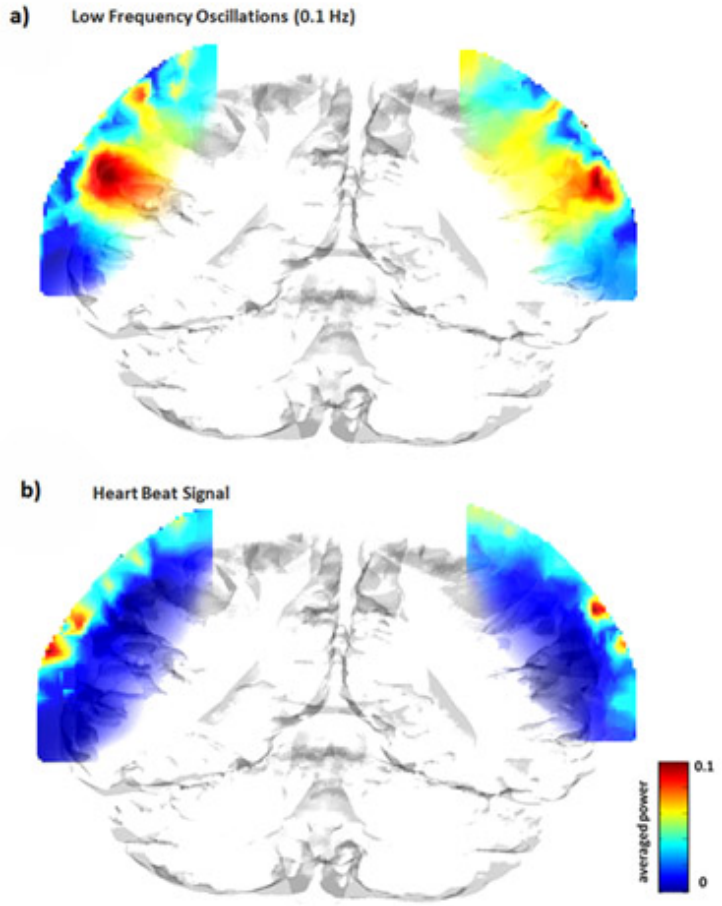

Figure 7.7: Frontal view on the reconstruction volumes of both hemispheres. Voxels are color-coded with their average power at (*a*) 0.1 Hz and (*b*) heart beat rate for eight subjects (grand average).

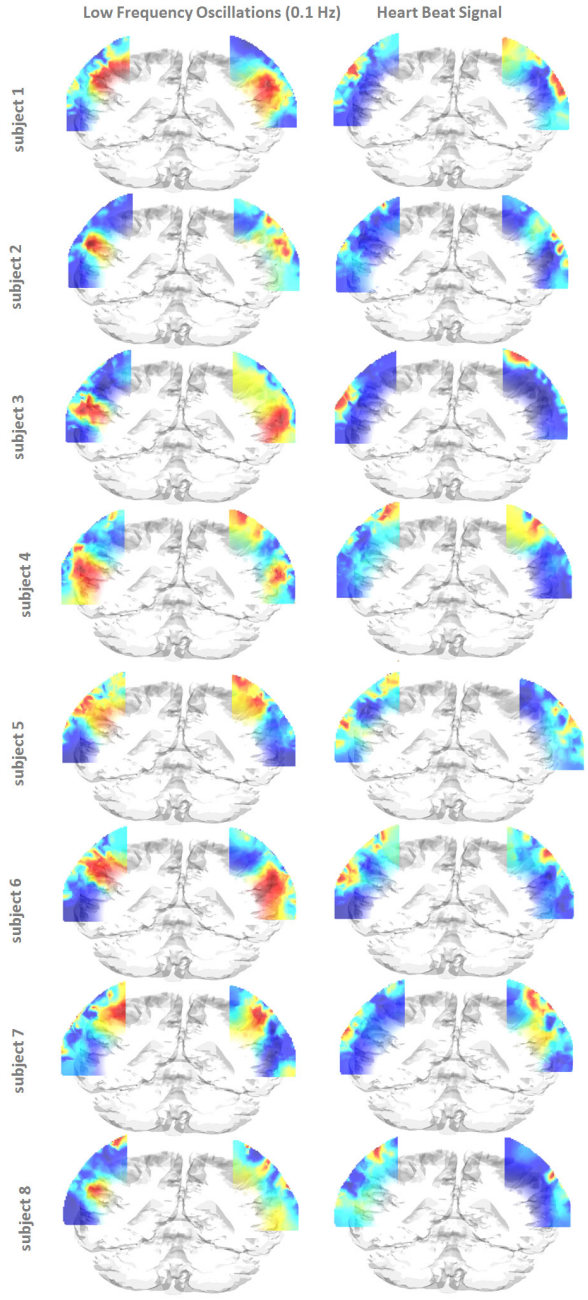

Figure 7.8: Frontal view on the reconstruction volumes of both hemispheres. Voxels are color-coded with their normalized power at 0.1 Hz (left) and heart beat rate (right column) for eight individuals.

7.3 Discussion

In this study, we demonstrated that DOT in conjunction with 3D image reconstruction allows a depth profiling of hemodynamic rhythms in the adult head. Contamination of NIRS measurements with low frequency oscillations in the 0.1Hz band and heart beat signals have been frequently reported. However, the spatial origin of these blood-flow related signals remained unclear, since fNIRS provides no depth resolution. Nevertheless, within the last years LFO have become a target to investigate resting state connectivity with NIRS (Tong and Frederick, 2010; Schytz et al., 2012; Phillip et al., 2013; Nakao et al., 2013). This study aimed at investigating the (spatial) origin of LFO and heart beat signals in NIRS measurements. Skin or brain, that was the question. We showed that DOT as a 3D modality of NIRS allows to determine the origin of LFO in optical measurements. We found a high relative fraction of LFO in cortical voxels. However, slow fluctuations were also seen in short fiber-distances in the raw data as well as in superficial voxels of the reconstruction volume, we must assume that a part of the measured oscillations actually stem from the skin. The same analysis for heart beat signals revealed a concentration within superficial layers. These findings were consistent throughout all subjects.

There are some important implications of these results. First, the higher contamination with LFO in HbO_2 compared to HbR time courses is in line with observations from our and other groups, stressing the necessity of a careful pre-processing of NIRS data from the HbO_2 sensitive wavelength. Again, we underline the importance of HbR time courses when analyzing functional brain imaging data. Second, fNIRS might be an inappropriate tool to investigate resting state networks based on LFO, since the fraction of cortical and non-cortical LFO can not be estimated without depth resolution.

However, when looking forward to potential clinical applications e.g. in neurointensive care patients, we have to investigate, if monitoring these hemodynamic features with a tomographic setup could be an additional module to detect changes in cerebral blood flow at the bedside. A correlation between a changed pattern of the distribution of LFO and a changed or reduced perfusion has not been investigated so far but is subject to further studies. Since there is usually no continuous monitoring of brain perfusion, neurointensive care patients with a risk of suffering from an under-supply of oxygen could benefit from such a bedside monitor.

8 Conclusion and Outlook

Aim of this work was to promote DOT as a functional brain imaging tool. I demonstrated, that DOT vastly improves fNIRS, bringing it closer to the capabilities of fMRI, the gold standard of functional brain imaging. Due to its multi-distance approach and its increased spatial resolution, DOT is able to detect very small activations in the sub-centimeter range. Even more important, I showed that DOT is able to separate cortical from non-cortical signals.

I performed extensive simulation studies, thereby introducing a novel approach to generate highly realistic artificial data and adapted a wide range of reconstruction methods for DOT. I demonstrated the superiority of sparse reconstruction methods but also showed, that linear methods can provide sufficient good results with low computational costs. Furthermore, I demonstrated a fast way to chose the regularization parameter independent from user influence.

In the second part, results from *in vivo* measurements using high-resolution DOT in humans were presented. I evaluated and improved the applicability of DOT and tested its limitations and potentials concerning spatial resolution and depth separation.

Future studies will investigate multi-modal image reconstruction, simultaneously using EEG and DOT in order to obtain a more robust reconstruction for complex sources.

Small and mobile devices that cover large areas of the head will be needed for future applications. First steps are done by our group (Piper et al., 2014) but still have the potential for improvement, especially concerning head coverage, fiber design and fiber application. Pointed fibers could minimize the effort which is still necessary to apply the fibers on the head and in the same time, the spatial resolution could be improved by ultra-dense fiber grids and more data channels. Consequently this would reduce the ill-posedness

of the inverse problem and decrease the sensitivity to noise.

An easy-to-apply mobile tomography system could serve in many areas of research, starting with investigations in the field of developmental psychology with experimental set-ups in real-life environments like schools. It would encourage more psychiatric studies and in general a wider spread of the method. As already mentioned, we deem the technique now ready for a broad usage in clinical studies, diagnosis, and general neuroscience research: studies on epilepsy and brain perfusion will follow.

Bibliography

Arridge, S. R. and Hebden, J. C. (1997). Optical imaging in medicine: Ii. modelling and reconstruction. *Phys Med Biol*, 42(5):841–853.

Arridge, S. R., Schweiger, M., Hiraoka, M., and Delpy, D. T. (1993). A finite element approach for modeling photon transport in tissue. *Med Phys*, 20(2 Pt 1):299–309.

Ashburner, J. (2012). Spm: a history. *Neuroimage*, 62(2):791–800.

Ashburner, J., Barnes, G., Chen, C., Daunizeau, J., Flandin, G., Friston, K., Gitelman, D., Kiebel, S., Kilner, J., Litvak, V., Moran, R., Penny, W., Stephan, K., Gitelman, D., Henson, R., Hutton, C., Glauche, V., Mattout, J., and Phillips, C. (2011). *SPM8 Manual*.

Aslin, R. N. (2012). Questioning the questions that have been asked about the infant brain using near-infrared spectroscopy. *Cogn Neuropsychol*, 29(1-2):7–33.

Barbour, R. L., Graber, H. L., Pei, Y., Zhong, S., and Schmitz, C. H. (2001). Optical tomographic imaging of dynamic features of dense-scattering media. *J Opt Soc Am A Opt Image Sci Vis*, 18(12):3018–36.

Bevilacqua, F., Piguet, D., Marquet, P., Gross, J. D., Tromberg, B. J., and Depeursinge, C. (1999). In vivo local determination of tissue optical properties: applications to human brain. *Appl Opt*, 38(22):4939–4950.

Birbaumer, N. (2006). Breaking the silence: brain-computer interfaces (bci) for communication and motor control. *Psychophysiology*, 43(6):517–32.

Birbaumer, N., Weber, C., Neuper, C., Buch, E., Haapen, K., and Cohen, L. (2006). Physiological regulation of thinking: brain-computer interface (bci) research. *Prog Brain Res*, 159:369–91.

Bluestone, A., Abdoulaev, G., Schmitz, C., Barbour, R., and Hielscher, A. (2001). Three-dimensional optical tomography of hemodynamics in the human head. *Opt Express*, 9(6):272–86.

Boas, D. A., Chen, K., Grebert, D., and Franceschini, M. A. (2004). Improving the diffuse optical imaging spatial resolution of the cerebral hemodynamic response to brain activation in humans. *Opt Lett*, 29(13):1506–8.

Boynton, G. M., Engel, S. A., Glover, G. H., and Heeger, D. J. (1996). Linear systems analysis of functional magnetic resonance imaging in human v1. *J Neurosci*, 16(13):4207–21.

Buchheim, K., Obrig, H., v Pannwitz, W., Muller, A., Heekeren, H., Villringer, A., and Meierkord, H. (2004). Decrease in haemoglobin oxygenation during absence seizures in adult humans. *Neurosci Lett*, 354(2):119–22.

Budohoski, K. P., Czosnyka, M., Smielewski, P., Kasprowicz, M., Helmy, A., Bulters, D., Pickard, J. D., and Kirkpatrick, P. J. (2012). Impairment of cerebral autoregulation predicts delayed cerebral ischemia after subarachnoid hemorrhage: a prospective observational study. *Stroke*, 43(12):3230–7.

Choi, J., Wolf, M., Toronov, V., Wolf, U., Polzonetti, C., Hueber, D., Safonova, L. P., Gupta, R., Michalos, A., Mantulin, W., and Gratton, E. (2004). Noninvasive determination of the optical properties of adult brain: near-infrared spectroscopy approach. *J Biomed Opt*, 9(1):221–229.

Collins, D., Zijdenbos, A., Baar´e, W. C., and Evans, A. (1999). *ANIMAL+INSECT: Improved Cortical Structure Segmentation*, volume 1613 of *Lecture Notes in Computer Science*, pages 210–223. Springer Berlin Heidelberg.

Cooper, R. J., Caffini, M., Dubb, J., Fang, Q., Custo, A., Tsuzuki, D., Fischl, B., Wells, W., r., Dan, I., and Boas, D. A. (2012). Validating atlas-guided dot: a comparison of diffuse optical tomography informed by atlas and subject-specific anatomies. *Neuroimage*, 62(3):1999–2006.

Cope, M., Delpy, D. T., Reynolds, E. O., Wray, S., Wyatt, J., and van der Zee, P. (1988). Methods of quantitating cerebral near infrared spectroscopy data. *Adv Exp Med Biol*, 222:183–9.

Custo, A., Boas, D. A., Tsuzuki, D., Dan, I., Mesquita, R., Fischl, B., Grimson, W. E., and Wells, W., r. (2010). Anatomical atlas-guided diffuse optical tomography of brain activation. *Neuroimage*, 49(1):561–7.

Dehghani, H., Eames, M. E., Yalavarthy, P. K., Davis, S. C., Srinivasan, S., Carpenter, C. M., Pogue, B. W., and Paulsen, K. D. (2008). Near infrared optical tomography using nirfast: Algorithm for numerical model and image reconstruction. *Commun Numer Methods Eng*, 25(6):711–732.

Dehghani, H., White, B. R., Zeff, B. W., Tizzard, A., and Culver, J. P. (2009). Depth sensitivity and image reconstruction analysis of dense imaging arrays for mapping brain function with diffuse optical tomography. *Appl Opt*, 48(10):D137–43.

Delpy, D. T., Cope, M., van der Zee, P., Arridge, S., Wray, S., and Wyatt, J. (1988). Estimation of optical pathlength through tissue from direct time of flight measurement. *Phys Med Biol*, 33(12):1433–42.

Desmettre, T., Devoisselle, J. M., and Mordon, S. (2000). Fluorescence properties and metabolic features of indocyanine green (icg) as related to angiography. *Surv Ophthalmol*, 45(1):15–27.

Dogdas, B., Shattuck, D. W., and Leahy, R. M. (2005). Segmentation of skull and scalp in 3-d human mri using mathematical morphology. *Hum Brain Mapp*, 26(4):273–85.

Ebert, B., Riefke, B., Sukowski, U., and Licha, K. (2011). Cyanine dyes as contrast agents for near-infrared imaging in vivo: acute tolerance, pharmacokinetics, and fluorescence imaging. *J Biomed Opt*, 16(6):066003.

Evans, A. C., Collins, D., Mills, S., Brown, E., Kelly, R., and Peters, T. (1993). 3d statistical neuroanatomical models from 305 mri volumes. In *Proc. IEEE-Nuclear Science Symposium and Medical Imaging Conference*, pages 1813–1817. Proc. IEEE-Nuclear Science Symposium and Medical Imaging Conference.

Fan, W. (2012). Electrical impedance tomography for human lung reconstruction based on tv regularization algorithm. In *Intelligent Control and Information Processing (ICICIP), 2012 Third International Conference on*, pages 660–663.

Fang, Q. (2010). Mesh-based monte carlo method using fast ray-tracing in plucker coordinates. *Biomed Opt Express*, 1(1):165–175.

Fang, Q. and Boas, D. A. (2009). Monte carlo simulation of photon migration in 3d turbid media accelerated by graphics processing units. *Opt Express*, 17(22):20178–90.

Fazli, S., Mehnert, J., Steinbrink, J., and Blankertz, B. (2012a). Using nirs as a predictor for eeg-based bci performance. *Conf Proc IEEE Eng Med Biol Soc*, 2012:4911–4.

Fazli, S., Mehnert, J., Steinbrink, J., Curio, G., Villringer, A., Muller, K. R., and Blankertz, B. (2012b). Enhanced performance by a hybrid nirs-eeg brain computer interface. *Neuroimage*, 59(1):519–29.

Fonov, V., Evans, A. C., Botteron, K., Almli, C. R., McKinstry, R. C., and Collins, D. L. (2011). Unbiased average age-appropriate atlases for pediatric studies. *Neuroimage*, 54(1):313–27.

Fonov, V. S., Evans, A. C., McKinstry, R. C., Almli, C. R., and Collins, D. L. (2009). Unbiased nonlinear average age-appropriate brain templates from birth to adulthood. *NeuroImage*, 47, Supplement 1(0):S102.

Fox, P. T. and Raichle, M. E. (1986). Focal physiological uncoupling of cerebral blood flow and oxidative metabolism during somatosensory stimulation in human subjects. *Proc Natl Acad Sci U S A*, 83(4):1140–4.

Franceschini, M. A., Fantini, S., Thompson, J. H., Culver, J. P., and Boas, D. A. (2003). Hemodynamic evoked response of the sensorimotor cortex measured noninvasively with near-infrared optical imaging. *Psychophysiology*, 40(4):548–60.

Franceschini, M. A., Joseph, D. K., Huppert, T. J., Diamond, S. G., and Boas, D. A. (2006). Diffuse optical imaging of the whole head. *J Biomed Opt*, 11(5):054007.

Franceschini, M. A., Thaker, S., Themelis, G., Krishnamoorthy, K. K., Bortfeld, H., Diamond, S. G., Boas, D. A., Arvin, K., and Grant, P. E. (2007). Assessment of infant brain development with frequency-domain near-infrared spectroscopy. *Pediatr Res*, 61(5 Pt 1):546–51.

Friston, K. J., Holmes, A. P., Poline, J. B., Grasby, P. J., Williams, S. C., Frackowiak, R. S., and Turner, R. (1995). Analysis of fmri time-series revisited. *Neuroimage*, 2(1):45–53.

Gagnon, C., Desjardins-Crepeau, L., Tournier, I., Desjardins, M., Lesage, F., Greenwood, C. E., and Bherer, L. (2012). Near-infrared imaging of the effects of glucose ingestion and regulation on prefrontal activation during dual-task execution in healthy fasting older adults. *Behav Brain Res*, 232(1):137–47.

Gibson, A. P., Austin, T., Everdell, N. L., Schweiger, M., Arridge, S. R., Meek, J. H., Wyatt, J. S., Delpy, D. T., and Hebden, J. C. (2006). Three-dimensional whole-head optical tomography of passive motor evoked responses in the neonate. *Neuroimage*, 30(2):521–8.

Goebel, R. (2012). Brainvoyager–past, present, future. *Neuroimage*, 62(2):748–56.

Goff, D. A., Buckley, E. M., Durduran, T., Wang, J., and Licht, D. J. (2010). Noninvasive cerebral perfusion imaging in high-risk neonates. *Semin Perinatol*, 34(1):46–56.

Golub, G. H., Heath, M., and Wahba, G. (1979). Generalized cross-validation as a method for choosing a good ridge parameter. *Technometrics*, 21(2):215–223.

Gramfort, A., Strohmeier, D., Haueisen, J., Hämäläinen, M. S., and Kowalski, M. (2013). Time-frequency mixed-norm estimates: sparse m/eeg imaging with non-stationary source activations. *Neuroimage*, 70:410–422.

Gregg, N. M., White, B. R., Zeff, B. W., Berger, A. J., and Culver, J. P. (2010). Brain specificity of diffuse optical imaging: improvements from superficial signal regression and tomography. *Front Neuroenergetics*, 2.

Habermehl, C., Holtze, S., Steinbrink, J., Koch, S. P., Obrig, H., Mehnert, J., and Schmitz, C. H. (2012). Somatosensory activation of two fingers can be discriminated with ultrahigh-density diffuse optical tomography. *Neuroimage*, 59(4):3201–11.

Habermehl, C., Schmitz, C. H., and Steinbrink, J. (2011). Contrast enhanced high-resolution diffuse optical tomography of the human brain using icg. *Opt Express*, 19(19):18636–44.

Hamalainen, M. S. and Ilmoniemi, R. J. (1994). Interpreting magnetic fields of the brain: minimum norm estimates. *Med Biol Eng Comput*, 32(1):35–42.

Haufe, S., Nikulin, V. V., Ziehe, A., Muller, K. R., and Nolte, G. (2008). Combining sparsity and rotational invariance in eeg/meg source reconstruction. *Neuroimage*, 42(2):726–38.

Haufe, S., Tomioka, R., Dickhaus, T., Sannelli, C., Blankertz, B., Nolte, G., and Muller, K. R. (2011). Large-scale eeg/meg source localization with spatial flexibility. *Neuroimage*, 54(2):851–9.

Holper, L., Biallas, M., and Wolf, M. (2009). Task complexity relates to activation of cortical motor areas during uni- and bimanual performance: a functional nirs study. *Neuroimage*, 46(4):1105–13.

Holper, L., Muehlemann, T., Scholkmann, F., Eng, K., Kiper, D., and Wolf, M. (2010). Testing the potential of a virtual reality neurorehabilitation system during performance of observation, imagery and imitation of motor actions recorded by wireless functional near-infrared spectroscopy (fnirs). *J Neuroeng Rehabil*, 7:57.

Hopton, P., Walsh, T. S., and Lee, A. (1999). Measurement of cerebral blood volume using near-infrared spectroscopy and indocyanine green elimination. *J Appl Physiol*, 87(5):1981–7.

Horn, B. (1987). Closed-form solution of absolute orientation using unit quaternions. *J. Opt. Soc. Am. A*, 4(4):629–642.

Hyde, D. C., Boas, D. A., Blair, C., and Carey, S. (2010). Near-infrared spectroscopy shows right parietal specialization for number in pre-verbal infants. *Neuroimage*, 53(2):647–52.

Hyodo, K., Dan, I., Suwabe, K., Kyutoku, Y., Yamada, Y., Akahori, M., Byun, K., Kato, M., and Soya, H. (2012). Acute moderate exercise enhances compensatory brain activation in older adults. *Neurobiol Aging*, 33(11):2621–32.

Jackson, P. A., Reay, J. L., Scholey, A. B., and Kennedy, D. O. (2012). Dharich oil modulates the cerebral haemodynamic response to cognitive tasks in healthy young adults: a near ir spectroscopy pilot study. *Br J Nutr*, 107(8):1093–8.

Jacobsen, M., Hansen, P., and Saunders, M. (2003). Subspace preconditioned lsqr for discrete ill-posed problems. *BIT Numerical Mathematics*, 43(5):975–989.

Jagannath, R. P. K. and Yalavarthy, P. K. (2012). Minimal residual method provides optimal regularization parameter for diffuse optical tomography. *J Biomed Opt*, 17(10):106015.

Jermyn, M., Ghadyani, H., Mastanduno, M. A., Turner, W., Davis, S. C., Dehghani, H., and Pogue, B. W. (2013). Fast segmentation and high-quality three-dimensional volume mesh creation from medical images for diffuse optical tomography. *J Biomed Opt*, 18(8):86007.

Jermyn, M., Pogue, B., Ghadyani, H. R., Davis, S., Mastanduno, M. A., and Dehghani, H. a. (2012). A user-enabling visual workflow for near-infrared light transport modeling in tissue. In *Biomedical Optics*, OSA Technical Digest, page BW1A.7. Optical Society of America.

Joseph, D. K., Huppert, T. J., Franceschini, M. A., and Boas, D. A. (2006). Diffuse optical tomography system to image brain activation with improved spatial resolution and validation with functional magnetic resonance imaging. *Appl Opt*, 45(31):8142–51.

Jurcak, V., Okamoto, M., Singh, A., and Dan, I. (2005). Virtual 10-20 measurement on mr images for inter-modal linking of transcranial and tomographic neuroimaging methods. *Neuroimage*, 26(4):1184–92.

Kameyama, M., Fukuda, M., Yamagishi, Y., Sato, T., Uehara, T., Ito, M., Suto, T., and Mikuni, M. (2006). Frontal lobe function in bipolar disorder: a multichannel near-infrared spectroscopy study. *Neuroimage*, 29(1):172–84.

Kavuri, V. C., Lin, Z. J., Tian, F., and Liu, H. (2012). Sparsity enhanced spatial resolution and depth localization in diffuse optical tomography. *Biomed Opt Express*, 3(5):943–57.

Keller, E., Ishihara, H., Nadler, A., Niederer, P., Seifert, B., Yonekawa, Y., and Frei, K. (2002). Evaluation of brain toxicity following near infrared light exposure after indocyanine green dye injection. *J Neurosci Methods*, 117(1):23–31.

Keller, E., Nadler, A., Alkadhi, H., Kollias, S. S., Yonekawa, Y., and Niederer, P. (2003). Noninvasive measurement of regional cerebral blood flow and regional cerebral blood volume by near-infrared spectroscopy and indocyanine green dye dilution. *Neuroimage*, 20(2):828–39.

Kirilina, E., Jelzow, A., Heine, A., Niessing, M., Wabnitz, H., Bruhl, R., Ittermann, B., Jacobs, A. M., and Tachtsidis, I. (2012). The physiological origin of task-evoked systemic artefacts in functional near infrared spectroscopy. *Neuroimage*, 61(1):70–81.

Klem, G. H., Luders, H. O., Jasper, H. H., and Elger, C. (1999). The ten-twenty electrode system of the international federation. the international federation of clinical neurophysiology. *Electroencephalogr Clin Neurophysiol Suppl*, 52:3–6.

Koch, S. P., Habermehl, C., Mehnert, J., Schmitz, C. H., Holtze, S., Villringer, A., Steinbrink, J., and Obrig, H. (2010). High-resolution optical functional mapping of the human somatosensory cortex. *Front Neuroenergetics*, 2:12.

Kohl-Bareis, M., Obrig, H., Steinbrink, J., Malak, J., Uludag, K., and Villringer, A. (2002). Noninvasive monitoring of cerebral blood flow by a dye bolus method: separation of brain from skin and skull signals. *J Biomed Opt*, 7(3):464–70.

Kurth, R., Villringer, K., Curio, G., Wolf, K. J., Krause, T., Repenthin, J., Schwiemann, J., Deuchert, M., and Villringer, A. (2000). fmri shows multiple somatotopic digit representations in human primary somatosensory cortex. *Neuroreport*, 11(7):1487–91.

Kwak, J. G., Kim, W. H., Oh, A. Y., Yoon, T. G., Kim, H. S., Chae, J. H., and Park, S. Y. (2007). Is unilateral brain regional perfusion neurologically safe during congenital aortic arch surgery? *Eur J Cardiothorac Surg*, 32(5):751–5.

Landsman, M. L., Kwant, G., Mook, G. A., and Zijlstra, W. G. (1976). Light-absorbing properties, stability, and spectral stabilization of indocyanine green. *J Appl Physiol*, 40(4):575–83.

Liao, S. M., Gregg, N. M., White, B. R., Zeff, B. W., Bjerkaas, K. A., Inder, T. E., and Culver, J. P. (2010). Neonatal hemodynamic response to visual cortex activity: high-density near-infrared spectroscopy study. *J Biomed Opt*, 15(2):026010.

Liebert, A., Wabnitz, H., Obrig, H., Erdmann, R., Moller, M., Macdonald, R., Rinneberg, H., Villringer, A., and Steinbrink, J. (2006). Non-invasive detection of fluorescence from exogenous chromophores in the adult human brain. *Neuroimage*, 31(2):600–8.

Liebert, A., Wabnitz, H., Steinbrink, J., Obrig, H., Moller, M., Macdonald, R., Villringer, A., and Rinneberg, H. (2004). Time-resolved multidistance near-infrared spectroscopy of the adult head: intracerebral and extracerebral absorption changes from moments of distribution of times of flight of photons. *Appl Opt*, 43(15):3037–47.

Maldjian, J. A., Gottschalk, A., Patel, R. S., Detre, J. A., and Alsop, D. C. (1999). The sensory somatotopic map of the human hand demonstrated at 4 tesla. *Neuroimage*, 10(1):55–62.

Matsuura, K. and Okabe, Y. (1995). Selective minimum-norm solution of the biomagnetic inverse problem. *IEEE Trans Biomed Eng*, 42(6):608–15.

Medvedev, A. V. (2013). Does the resting state connectivity have hemispheric asymmetry? a near-infrared spectroscopy study. *Neuroimage*.

Mesquita, R. C., Franceschini, M. A., and Boas, D. A. (2010). Resting state functional connectivity of the whole head with near-infrared spectroscopy. *Biomed Opt Express*, 1(1):324–336.

Mittnacht, A. J. (2010). Near infrared spectroscopy in children at high risk of low perfusion. *Curr Opin Anaesthesiol*, 23(3):342–7.

Miyai, I., Tanabe, H. C., Sase, I., Eda, H., Oda, I., Konishi, I., Tsunazawa, Y., Suzuki, T., Yanagida, T., and Kubota, K. (2001). Cortical mapping of gait in humans: a near-infrared spectroscopic topography study. *Neuroimage*, 14(5):1186–92.

Mohimani, H., Babaie-Zadeh, M., and Jutten, C. (2009). A fast approach for overcomplete sparse decomposition based on smoothed l0 norm. *Signal Processing, IEEE Transactions on*, 57(1):289–301.

Montoya-Martinez, J., Artes-Rodriguez, A., Hansen, L., and Pontil, M. (2012). Structured sparsity regularization approach to the eeg inverse problem. In *Cognitive Information Processing (CIP), 2012 3rd International Workshop on*, pages 1–6.

Murase, K., Yamazaki, Y., and Miyazaki, S. (2004). Deconvolution analysis of dynamic contrast-enhanced data based on singular value decomposition optimized by generalized cross validation. *Magn Reson Med Sci*, 3(4):165–75.

Murkin, J. M. and Arango, M. (2009). Near-infrared spectroscopy as an index of brain and tissue oxygenation. *Br J Anaesth*, 103 Suppl 1:i3–13.

Nakahachi, T., Ishii, R., Iwase, M., Canuet, L., Takahashi, H., Kurimoto, R., Ikezawa, K., Azechi, M., Kajimoto, O., and Takeda, M. (2010). Frontal cortex activation associated with speeded processing of visuospatial working memory revealed by multichannel near-infrared spectroscopy during advanced trail making test performance. *Behav Brain Res*, 215(1):21–7.

Nakao, T., Matsumoto, T., Shimizu, D., Morita, M., Yoshimura, S., Northoff, G., Morinobu, S., Okamoto, Y., and Yamawaki, S. (2013). Resting state low-frequency fluctuations in prefrontal cortex reflect degrees of harm avoidance and novelty seeking: an exploratory nirs study. *Front Syst Neurosci*, 7:115.

Nguyen, D. K., Tremblay, J., Pouliot, P., Vannasing, P., Florea, O., Carmant, L., Lepore, F., Sawan, M., Lesage, F., and Lassonde, M. (2013). Noninvasive continuous functional near-infrared spectroscopy combined with electroencephalography recording of frontal lobe seizures. *Epilepsia*, 54(2):331–40.

Niu, H., Lin, Z. J., Tian, F., Dhamne, S., and Liu, H. (2010a). Comprehensive investigation of three-dimensional diffuse optical tomography with depth compensation algorithm. *J Biomed Opt*, 15(4):046005.

Niu, H., Tian, F., Lin, Z. J., and Liu, H. (2010b). Development of a compensation algorithm for accurate depth localization in diffuse optical tomography. *Opt Lett*, 35(3):429–31.

Obrig, H., Neufang, M., Wenzel, R., Kohl, M., Steinbrink, J., Einhaupl, K., and Villringer, A. (2000). Spontaneous low frequency oscillations of cerebral hemodynamics and metabolism in human adults. *Neuroimage*, 12(6):623–39.

Obrig, H. and Villringer, A. (2003). Beyond the visible–imaging the human brain with light. *J Cereb Blood Flow Metab*, 23(1):1–18.

Okada, E., Firbank, M., Schweiger, M., Arridge, S. R., Cope, M., and Delpy, D. T. (1997). Theoretical and experimental investigation of near-infrared light propagation in a model of the adult head. *Appl Opt*, 36(1):21–31.

Oldag, A., Goertler, M., Bertz, A. K., Schreiber, S., Stoppel, C., Heinze, H. J., and Kopitzki, K. (2012). Assessment of cortical hemodynamics by multichannel near-infrared spectroscopy in steno-occlusive disease of the middle cerebral artery. *Stroke*, 43(11):2980–5.

Paulsen, K. D. and Jiang, H. (1995). Spatially varying optical property reconstruction using a finite element diffusion equation approximation. *Med Phys*, 22(6):691–701.

Pei, Y., Graber, H. L., and Barbour, R. L. (2001). Influence of systematic errors in reference states on image quality and on stability of derived information for dc optical imaging. *Appl Opt*, 40(31):5755–69.

Pfurtscheller, G., Allison, B. Z., Brunner, C., Bauernfeind, G., Solis-Escalante, T., Scherer, R., Zander, T. O., Mueller-Putz, G., Neuper, C., and Birbaumer, N. (2010). The hybrid bci. *Front Neurosci*, 4:30.

Phillip, D., Iversen, H. K., Schytz, H. W., Selb, J., Boas, D. A., and Ashina, M. (2013). Altered low frequency oscillations of cortical vessels in patients with cerebrovascular occlusive disease - a nirs study. *Front Neurol*, 4:204.

Piper, S. K., Krueger, A., Koch, S. P., Mehnert, J., Habermehl, C., Steinbrink, J., Obrig, H., and Schmitz, C. H. (2014). A wearable multi-channel fnirs system for brain imaging in freely moving subjects. *Neuroimage*, 85 Pt 1:64–71.

Pizza, F., Biallas, M., Kallweit, U., Wolf, M., and Bassetti, C. L. (2012). Cerebral hemodynamic changes in stroke during sleep-disordered breathing. *Stroke*, 43(7):1951–3.

Power, S. D., Kushki, A., and Chau, T. (2012). Automatic single-trial discrimination of mental arithmetic, mental singing and the no-control state from prefrontal activity: toward a three-state nirs-bci. *BMC Res Notes*, 5:141.

Prakash, J., Shaw, C., Manjappa, R., Kanhirodan, R., and Yalavarthy, P. K. (2013). Sparse recovery methods hold promise for diffuse optical tomographic image reconstruction. *Selected Topics in Quantum Electronics, IEEE Journal of*, PP(99):1–1.

Rubner, Y., Tomasi, C., and Guibas, L. (1998). A metric for distributions with applications to image databases. In *IEEE International Conference on Computer Vision*.

Salehi Ravesh, M., Brix, G., Laun, F. B., Kuder, T. A., Puderbach, M., Ley-Zaporozhan, J., Ley, S., Fieselmann, A., Herrmann, M. F., Schranz, W., Semmler, W., and Risse, F. (2013). Quantification of pulmonary microcirculation by dynamic contrast-enhanced magnetic resonance imaging: comparison of four regularization methods. *Magn Reson Med*, 69(1):188–199.

Sasai, S., Homae, F., Watanabe, H., Sasaki, A. T., Tanabe, H. C., Sadato, N., and Taga, G. (2012). A nirs-fmri study of resting state network. *Neuroimage*, 63(1):179–93.

Sasai, S., Homae, F., Watanabe, H., and Taga, G. (2011). Frequency-specific functional connectivity in the brain during resting state revealed by nirs. *Neuroimage*, 56(1):252–7.

Sassaroli, A. and Fantini, S. (2004). Comment on the modified beer-lambert law for scattering media. *Phys Med Biol*, 49(14):N255–7.

Sassaroli, A., Pierro, M., Bergethon, P., and Fantini, S. (2012). Low-frequency spontaneous oscillations of cerebral hemodynamics investigated with near-infrared spectroscopy: A review. *Selected Topics in Quantum Electronics, IEEE Journal of*, 18(4):1478–1492.

Schmitz, C. H., Graber, H. L., Luo, H., Arif, I., Hira, J., Pei, Y., Bluestone, A., Zhong, S., Andronica, R., Soller, I., Ramirez, N., Barbour, S. L., and Barbour, R. L. (2000). Instrumentation and calibration protocol for imaging dynamic features in dense-scattering media by optical tomography. *Appl Opt*, 39(34):6466–86.

Schmitz, C. H., L?űcker, M., Lasker, J. M., Hielscher, A., and Barbour, R. L. (2002). Instrumentation for fast functional optical tomography. *Review of Scientific Intruments*, 73(2):429–439.

Schweizer, R., Voit, D., and Frahm, J. (2008). Finger representations in human primary somatosensory cortex as revealed by high-resolution functional mri of tactile stimulation. *Neuroimage*, 42(1):28–35.

Schytz, H. W., Hansen, J. M., Phillip, D., Selb, J., Boas, D. A., and Ashina, M. (2012). Nitric oxide modulation of low-frequency oscillations in cortical vessels in fhm–a nirs study. *Headache*, 52(7):1146–1154.

Schytz, H. W., Jensen, B. E., Jennum, P., Selb, J., Boas, D. A., and Ashina, M. (2013). Low-frequency oscillations and vasoreactivity of cortical vessels in obstructive sleep apnea during wakefulness: a near infrared spectroscopy study. *Sleep Med*, 14(5):416–421.

Shaw, C. B. and Yalavarthy, P. K. (2012a). Effective contrast recovery in rapid dynamic near-infrared diffuse optical tomography using l(1)-norm-based linear image reconstruction method. *J Biomed Opt*, 17(8):086009.

Shaw, C. B. and Yalavarthy, P. K. (2012b). Prior image-constrained l(1)-norm-based reconstruction method for effective usage of structural information in diffuse optical tomography. *Opt Lett*, 37(20):4353–5.

Sitaram, R., Caria, A., and Birbaumer, N. (2009). Hemodynamic brain-computer interfaces for communication and rehabilitation. *Neural Netw*, 22(9):1320–8.

Slone, E., Westwood, E., Dhaliwal, H., Federico, P., and Dunn, J. F. (2012). Near-infrared spectroscopy shows preictal haemodynamic changes in temporal lobe epilepsy. *Epileptic Disord*, 14(4):371–8.

Steinbrink, J., Villringer, A., Kempf, F., Haux, D., Boden, S., and Obrig, H. (2006). Illuminating the bold signal: combined fmri-fnirs studies. *Magn Reson Imaging*, 24(4):495–505.

Strangman, G., Franceschini, M. A., and Boas, D. A. (2003). Factors affecting the accuracy of near-infrared spectroscopy concentration calculations for focal changes in oxygenation parameters. *Neuroimage*, 18(4):865–79.

Sugiyama, M., Krauledat, M., and Müller, K. (2007). Covariate shift adaptation by importance weighted cross validation. *J. Mach. Learn. Res*, 8:985–1005.

Suhr, J. A. and Chelberg, M. B. (2013). Use of near-infrared spectroscopy as a measure of cerebrovascular health in aging adults. *Neuropsychol Dev Cogn B Aging Neuropsychol Cogn*, 20(2):243–52.

Suzen, M., Giannoula, A., and Durduran, T. (2010). Compressed sensing in diffuse optical tomography. *Opt Express*, 18(23):23676–90.

Taber, K. H., Hillman, E. M., and Hurley, R. A. (2010). Optical imaging: a new window to the adult brain. *J Neuropsychiatry Clin Neurosci*, 22(4):iv, 357–60.

Takeuchi, M., Hori, E., Takamoto, K., Tran, A. H., Satoru, K., Ishikawa, A., Ono, T., Endo, S., and Nishijo, H. (2009). Brain cortical mapping by simultaneous recording of functional near infrared spectroscopy and electroencephalograms from the whole brain during right median nerve stimulation. *Brain Topogr*, 22(3):197–214.

Telkemeyer, S., Rossi, S., Nierhaus, T., Steinbrink, J., Obrig, H., and Wartenburger, I. (2011). Acoustic processing of temporally modulated sounds in infants: evidence from a combined near-infrared spectroscopy and eeg study. *Front Psychol*, 1:62.

Terborg, C., Bramer, S., Harscher, S., Simon, M., and Witte, O. W. (2004). Bedside assessment of cerebral perfusion reductions in patients with acute ischaemic stroke by near-infrared spectroscopy and indocyanine green. *J Neurol Neurosurg Psychiatry*, 75(1):38–42.

Terborg, C., Groschel, K., Petrovitch, A., Ringer, T., Schnaudigel, S., Witte, O. W., and Kastrup, A. (2009). Noninvasive assessment of cerebral perfusion and oxygenation in acute ischemic stroke by near-infrared spectroscopy. *Eur Neurol*, 62(6):338–43.

Tong, Y. and Frederick, B. D. (2010). Time lag dependent multimodal processing of concurrent fmri and near-infrared spectroscopy (nirs) data suggests a global circulatory origin for low-frequency oscillation signals in human brain. *Neuroimage*, 53(2):553–564.

Tong, Y., Hocke, L. M., Nickerson, L. D., Licata, S. C., Lindsey, K. P., and Frederick, B. D. (2013). Evaluating the effects of systemic low frequency oscillations measured in the periphery on the independent component analysis results of resting state networks. *Neuroimage*, 76:202–15.

Torricelli, A., Pifferi, A., Taroni, P., Giambattistelli, E., and Cubeddu, R. (2001). In vivo optical characterization of human tissues from 610 to 1010 nm by time-resolved reflectance spectroscopy. *Phys Med Biol*, 46(8):2227–2237.

Tsujii, T., Komatsu, K., and Sakatani, K. (2013). Acute effects of physical exercise on prefrontal cortex activity in older adults: a functional near-infrared spectroscopy study. *Adv Exp Med Biol*, 765:293–8.

Van Veen, B. D., van Drongelen, W., Yuchtman, M., and Suzuki, A. (1997). Localization of brain electrical activity via linearly constrained minimum variance spatial filtering. *IEEE Trans Biomed Eng*, 44(9):867–80.

Wartenburger, I., Steinbrink, J., Telkemeyer, S., Friedrich, M., Friederici, A. D., and Obrig, H. (2007). The processing of prosody: Evidence of interhemispheric specialization at the age of four. *Neuroimage*, 34(1):416–25.

Weibull, A., Bjorkman, A., Hall, H., Rosen, B., Lundborg, G., and Svensson, J. (2008). Optimizing the mapping of finger areas in primary somatosensory cortex using functional mri. *Magn Reson Imaging*, 26(10):1342–51.

White, B. R. and Culver, J. P. (2010a). Phase-encoded retinotopy as an evaluation of diffuse optical neuroimaging. *Neuroimage*, 49(1):568–77.

White, B. R. and Culver, J. P. (2010b). Quantitative evaluation of high-density diffuse optical tomography: in vivo resolution and mapping performance. *J Biomed Opt*, 15(2):026006.

White, B. R., Snyder, A. Z., Cohen, A. L., Petersen, S. E., Raichle, M. E., Schlaggar, B. L., and Culver, J. P. (2009). Resting-state functional connectivity in the human brain revealed with diffuse optical tomography. *Neuroimage*, 47(1):148–56.

Wilcox, T., Stubbs, J., Hirshkowitz, A., and Boas, D. A. (2012). Functional activation of the infant cortex during object processing. *Neuroimage*, 62(3):1833–40.

Xu, Y., Graber, H. L., and Barbour, R. L. (2007). Image correction algorithm for functional three-dimensional diffuse optical tomography brain imaging. *Appl Opt*, 46(10):1693–704.

Zeff, B. W., White, B. R., Dehghani, H., Schlaggar, B. L., and Culver, J. P. (2007). Retinotopic mapping of adult human visual cortex with high-density diffuse optical tomography. *Proc Natl Acad Sci U S A*, 104(29):12169–74.

Zhu, Y., Liu, X., Wang, H., Jiang, T., Fang, Y., Hu, H., Wang, G., Wang, X., Liu, Z., and Zhang, K. (2010). Reduced prefrontal activation during tower of london in first-episode schizophrenia: a multi-channel near-infrared spectroscopy study. *Neurosci Lett*, 478(3):136–40.